Pontifícia Universidade Católica
do Rio de Janeiro

André Xavier Leitão

Stress-constrained Topology Optimization of Hyperelastic Structures

TESE DE DOUTORADO

Thesis presented to the Programa de Pós-Graduação em Engenharia Mecânica of PUC-Rio in partial fulfillment of the requirements for the degree of Doutor em Engenharia Mecânica.

Advisor: Prof. Anderson Pereira

Rio de Janeiro
October 2024

Pontifícia Universidade Católica
do Rio de Janeiro

André Xavier Leitão

Stress-constrained Topology Optimization of Hyperelastic Structures

Thesis presented to the Programa de Pós-Graduação em Engenharia Mecânica of PUC-Rio in partial fulfillment of the requirements for the degree of Doutor em Engenharia Mecânica. Approved by the Examination Committee:

Prof. Anderson Pereira
Advisor
Departamento de Engenharia Mecânica – PUC-Rio

Prof. Ivan Fabio Mota de Menezes
Departamento de Engenharia Mecânica – PUC-Rio

Prof. Americo Barbosa da Cunha Junior
Universidade do Estado do Rio de Janeiro – UERJ

Prof. André Maués Brabo Pereira
Universidade Federal Fluminense – UFF

Prof. Francisco de Assis das Neves
Universidade Federal de Ouro Preto – UFOP

Rio de Janeiro, October 25th, 2024

André Xavier Leitão

The author holds a bachelor's degree in Mechanical Engineering from Pontifícia Universidade Católica do Rio de Janeiro, PUC-Rio, in 2015. The author also has a master's degree in Mechanical Engineering from the same institution in 2019.

Bibliographic data

Leitão, André Xavier

Stress-constrained Topology Optimization of Hyperelastic Structures / André Xavier Leitão; advisor: Anderson Pereira – Rio de Janeiro: PUC-Rio, Departamento de Engenharia Mecânica, 2024.

145 f.: il. color.; 29,7 cm

Tese (Doutorado) – Pontifícia Universidade Católica do Rio de Janeiro, Departamento de Engenharia Mecânica.

Inclui referências bibliográficas.

Engenharia Mecânica – Teses. Topology Optimization; Continuum Mechanics; Hyperelasticity; Finite Elements; Energy Interpolation Scheme; Stress Constraint. I. Pereira, Anderson. II. Pontifícia Universidade Católica do Rio de Janeiro. Departamento de Engenharia Mecânica. III. Título.

CDD: 621

For all those who supported and encouraged me to get here.
And to my grandparents Francisco, Lourdinha and Zezinho (*in memoriam*).

Acknowledgments

This study was financed in part by the Coordenação de Aperfeiçoamento de Pessoal de Nível Superior – Brasil (CAPES) – Finance Code 001.

First and foremost, I thank God for the chance to join this Doctoral program, which will help me to improve both professionally and personally. I am grateful for all of the spiritual assistance that provided me with the confidence and fortitude to persevere throughout tough times.

Here on Earth, I thank my advisor, Professor Anderson Pereira, for believing in me, as well as the staff of the Engineering Mechanical Department (DEM) – Carlucio dos Santos, Carina de Abreu Beline, Fabio Soares Mesquita, Leninaldo Severino da Silva, Márcia Cerqueira de Magalhães and Simone de Souza Cordeiro. I am especially grateful to Professors Daniel Milbrath de Leon, Gustavo Assis da Silva, Johannes Achleitner, and Dr. Ing. Erich Wehrle for insightful conversations on specific topics of the current piece.

I would like to thank: Cleusa de Fátima Rosa, and my friends and colleagues Eduardo Enes Cota, Edson Sabino da Silva, Jeferson Luiz Rios, João Carlos Virgolino Soares, Juan Andrés Santisteban Hidalgo, Rodolfo Oliveira Paixão, Rodrigo Bianchi Santos, Thiago Almeida Cunha and especially Waldy Jair Torres Zuniga, among others, for their encouragement throughout this dissertation process; my friends Leonardo Simões de Abreu Carneiro, Priscila Gonzaga Rocha and Tainã Barbosa Silva for fortifying me while I was not well; Vinicius Oliveira Fontes for his friendship and collaborations in different scientific productions, in addition to valuable discussions on sensitivity computing; and José Eduardo de Souza for his inspirational speeches and patience.

My family is really important to me. Without them, life would be lot more difficult. My mother, Anna, father, José, and brother, Bruno, are always eager to stand by and strengthen me. Daisy, my grandmother, for whom I shall be eternally thankful for all she has done and continues to do for me – she is an inspiration, and I cannot find the right words to express how important she is in my life.

Abstract

Leitão, André Xavier; Pereira, Anderson (Advisor). **Stress-constrained Topology Optimization of Hyperelastic Structures.** Rio de Janeiro, 2024. 145p. Doctoral Thesis — Departamento de Engenharia Mecânica, Pontifícia Universidade Católica do Rio de Janeiro.

Topology optimization is a powerful engineering design tool that can lead to innovative layouts and significantly enhance the performance of engineered systems in various sectors. In a world where we are searching for cost reduction while being ecologically responsible, we should seek practical applications of topology optimization. Reducing weight while sustaining strength requirements is one of them. Another concern is the accurate prediction of the mechanical behavior of the wide variety of available materials, such as soft and rubber-like elastomers. To this end, incorporating nonlinearities will extend conventional topology optimization to hyperelastic structures and significantly enhance the performance at the primary design stage. We consider the density-based approach, which enforces us to properly address numerical instabilities of low-density regions through an energy interpolation scheme. An augmented Lagrangian-based formulation is used to deal with the large number of stress evaluation points, whereas polynomial vanishing constraints are employed to overturn the 'singularity' phenomenon. We conducted a preliminary investigation under linear-elastic circumstances to explore different strategies related to stress constraints which justify implementing the augmented Lagrangian method. In addition, we extract analytical expressions for sensitivity analysis with extreme rigor and detail. Problems in plane stress scenarios requires effective computation of the out-of-plane strain component. Then, in order to do this, we deduced analytical expressions and a numerical solution based on the Newton's method. Different examples validate our method, demonstrating the significance of considering stress constraints and nonlinearities in topology optimization. We additionally point out that solutions derived from linear theory often violate stress limits under nonlinear conditions, making them unsuitable for modeling structures that undergo large deformations.

Keywords

Topology Optimization; Continuum Mechanics; Hyperelasticity; Finite Elements; Energy Interpolation Scheme; Stress Constraint.

Resumo

Leitão, André Xavier; Pereira, Anderson (Orientador). **Otimização Topológica de Estruturas Hiperelásticas com Restrição de Tensão.** Rio de Janeiro, 2024. 145p. Tese de Doutorado — Departamento de Engenharia Mecânica, Pontifícia Universidade Católica do Rio de Janeiro.

Otimização topológica é uma ferramenta de projeto poderosa, podendo levar a estruturas inovadoras e melhorar significativamente o desempenho de sistemas projetados em diferentes setores da indústria. Em um mundo onde se busca a redução de custos ao mesmo tempo, em que se tenta ser ecologicamente sustentável, deve-se buscar aplicações práticas para a otimização topológica. Reduzir o peso enquanto restringe-se a resistência é uma delas. Outra preocupação é a previsão do comportamento mecânico de ampla variedade de materiais disponíveis, como elastômeros macios e borrachas. Para esse fim, a incorporação de não linearidades estenderá a otimização de topologia convencional para estruturas hiperelásticas e melhorará significativamente o desempenho no estágio inicial de projeto. Consideramos o método baseado em densidade, o que nos obriga a tratar adequadamente instabilidades numéricas em regiões de baixa rigidez por meio de um esquema de interpolação de energia. Uma formulação baseada no método do Lagrangiano aumentado é empregada para lidar com o grande número de pontos de tensão, enquanto restrições do tipo polinomial são empregadas para lidar com o fenômeno da 'singularidade'. Um estudo preliminar, em condições lineares elásticas, foi conduzido para avaliar as diferentes maneiras de se lidar com restrições de tensão, a partir do qual se optou pela utilização do Lagrangiano aumentado. Além disso, expressões analíticas para análise de sensibilidade são deduzidas com extremo rigor e detalhe. Problemas em tensão plana exigem computação eficaz do componente de deformação fora do plano. Para este fim, deduzimos expressões analíticas e uma solução numérica baseada no método de Newton. Diferentes exemplos validam a metodologia empregada, demonstrando a importância de considerar restrições de tensão e não linearidade em problemas de otimização topológica. Destacamos ainda que soluções oriundas da teoria linear tendem a violar os limites de tensão em condições não lineares, tornando-as inadequadas para modelar estruturas sujeitas a grandes deformações.

Palavras-chave

Otimização Topológica; Mecânica do Contínuo; Hiperelasticidade; Elementos Finitos; Esquema de Interpolação de Energia; Restrição de Tensão.

Contents

1 Introduction **16**
1.1 Motivation 16
1.2 Objectives 18
1.3 Main Contributions 18
1.4 Literature Review 19
1.5 Notation 21
1.6 Outline 22

2 The Basics of Continuum Mechanics **24**
2.1 Deformation 24
2.2 Strain Measures 27
2.2.1 Strain Principal Invariants 28
2.3 Stress Measures 28
2.3.1 Equivalent Stress 30
2.4 Hyperelasticity 31
2.4.1 Incompressible Formulations 32
2.4.2 Nearly Incompressible Formulations 33
2.4.3 Compressible Formulations 33
2.4.3.1 St. Venant-Kirchhoff Model 34
2.4.3.2 Modified St. Venant-Kirchhoff Model 34
2.4.3.3 Simo-Ciarlet Neo-Hookean Model 35
2.5 Two-dimensional Analysis 35

3 A Brief Review to the Finite Element Method **38**
3.1 The Finite Element Method Applied to Hyperelasticity 38
3.1.1 Incremental-Iterative Newton-Raphson Procedure 40
3.1.2 Finite Element Verification 41
3.1.2.1 Block Under Homogeneous Uniaxial Deformation 42
3.1.2.2 Block Under Uniaxial Deformation 44

4 Topology Optimization **46**
4.1 Density-driven Topology Optimization Procedures 46
4.1.1 Regularization Techniques 47
4.1.1.1 Linear Filtering Schemes 48
4.1.2 Nonlinear Projection Functions 49
4.1.2.1 Nonlinear Filtering Scheme 49
4.1.2.2 Hyperbolic Tangent Projection Function 51
4.1.3 Material Representation 51

5 Stress Formulations in Topology Optimization **52**

5.1 Difficulties of Stresses Constraints 52
5.1.1 Singular Optimum 52
5.1.1.1 *Traditional Vanishing Constraints* 53
5.1.1.2 *Polynomial Vanishing Constraints* 53
5.1.2 Large Number of Constraints 54
5.1.3 Nonlinear Response of Stresses 55
5.1.4 Accuracy of Stress Assessments 55
5.2 Solution via Local Stresses 55
5.2.1 Augmented Lagrangian Method in Equality-Constrained Problems 56
5.2.2 Augmented Lagrangian Method in Inequality-Constrained Problems 57
5.2.3 Augmented Lagrangian Method in Stress-Constrained Topology Optimization 59

6 Topology Optimization Under Nonlinearities 61
6.1 Problem Formulation 61
6.2 Nonlinear Analysis in Density-based Topology Optmization 62
6.2.1 Reduced Convergence Criterion 64
6.2.2 Energy Interpolation Scheme 64
6.2.2.1 Practical Implementation 65
6.2.3 C-Shape 68
6.2.4 Sensitivity Analysis 71
6.2.4.1 Computation of $\partial m/\partial \tilde{\rho}_e$ 72
6.2.4.2 Computation of $\partial \mathcal{A}^{(i)}/\partial \check{\rho}_e$ 72
6.2.4.3 Computation of $\partial g_j^+/\partial \boldsymbol{u}_j$ 73
6.2.4.4 Computation of $\partial \mathbf{F}_j/\partial(\gamma_j \boldsymbol{u}_j)$ 74
6.2.4.5 Computation of $\partial \mathbf{C}_j/\partial(\gamma_j \boldsymbol{u}_j)$ 76
6.2.4.6 Computation of $\partial J^{-1}/\partial(\gamma_j \boldsymbol{u}_j)$ 78
6.2.4.7 Computation of $\partial \mathbf{S}_j/\partial(\gamma_j \boldsymbol{u}_j)$ 78
6.2.4.8 Computation of $\partial \boldsymbol{\sigma}_j^{NL}/\partial(\gamma_j \boldsymbol{u}_j)$ 78
6.2.4.9 Computation of $\partial g_j^+/\partial \check{\rho}_e$ 79
6.2.4.10 Computation of $\partial \boldsymbol{f}_{int\,j}/\partial \check{\rho}_e$ 79
6.2.4.11 Sensitivity Verification 79

7 Results 82
7.1 U-Shape 84
7.2 Cantilever Beam 88
7.3 Crack Notch Beam 90

8 Conclusions 93
8.1 Suggestions for Future Works 94

Bibliography 96

A Stress Constraints in Linear-Elastic Problems 109
A.1 Linear-Elastic Stress-Constrained Topology Optimization Problem 109
A.2 Stress Model 110
A.3 Singular Optimum Techniques 110
A.3.1 ε-relaxation 110
A.3.2 qp-approach 111

A.3.3 Relaxed Stress 112
A.3.4 Comparison of Different Strategies 114
A.4 Stress Aggregation 115
A.5 Stress Regionalization 120
A.5.1 Stress Adaptive Correction Factor 124
A.6 Comparison of Different Strategies 125
A.6.1 L-Bracket 126
A.6.2 Stress Aggregation Strategy 128
A.6.3 Stress Regionalization Strategy 134
A.6.4 Local Stresses Strategy 141
A.6.5 Remarks on the Different Strategies 142

B A Quick Discussion on Mesh-dependence **145**

List of Figures

1.1 Aircraft engine bracket: (a) original design, (b) von Mises stress distribution of (a) considering the worst load scenario, (c) reconstruction of stress-constrained topology, and (d) von Mises stress field of (c) also in the worst load case scenario (adapted from Wu *et al.*, 2021). 17

1.2 Soft gripper optimized by Wang *et al.* (2020): (a) optimal design and (b) testing manufactored gripper for large deformations in each in-plane direction. 18

2.1 Displacement field of a typical particle. 25

2.2 Displacement of a material fiber into a spatial fiber. 25

2.3 Element of area under deformation. 29

3.1 Load control method diagrammatic. 41

3.2 Block under homogeneous uniaxial deformation. 42

3.3 Cauchy stress vs. stretch for the homogeneous uniaxial deformation. 44

3.4 Block under uniaxial deformation. 44

3.5 von Mises stress vs. stretch for a simple uniaxial deformation. 45

4.1 Two-dimensional linear density filter: (a) application in a regular quadrilateral element mesh and (b) its conical form. 49

4.2 Relation between design variables before and after the filtering scheme. The arrows indicate the direction in which the exponent s grows. 50

4.3 Effect of polynomial exponent in the nonlinear filtering scheme: (a) no filter, (b) $s = 1$ (linear filter), (c) $s = 2$, (d) $s = 3$ and (e) $s = 5$, (f) $s = 10$. 50

6.1 Reduced convergence criterion, RCC. The indicated nodes are not part of the convergence criteria. 64

6.2 C-shape (consistent units applied). 68

6.3 Effect of direct approach, RCC, and EIS in the LCM for the SVK model. 69

6.4 Effect of direct approach, RCC, and EIS in the LCM for the nH-SC model. 69

6.5 Number of iterations per load increment for (a) SVK model and (b) for nH-SC model. 70

6.6 C-shape deformation. 71

6.7 Cantilever beam to validate the sensitivity analysis (consistent units applied). 80

7.1 Optimization fluxogram. 84
7.2 U-shape. 84
7.3 U-shape material and stress distributions considering different material models in plane strain or plane stress. 85
7.4 Initial stress distribution in the SVK model in (a) plane strain and (b) plane stress. 86
7.5 U-shape submitted to nonlinear FE routine with opposite states. 87
7.6 Cantilever beam. 88
7.7 Cantilever beam material and stress distributions for linear and nonlinear analyses. 88
7.8 Cantilever linear-optimized layout submitted to nonlinear analysis: (a) material distribution, and (b) stress distribution at deformed configuration. 90
7.9 Crack notch beam. 90
7.10 Crack notch beam material and stress distributions for linear and nonlinear analyses. 91
7.11 Crack notch beam linear-optimized layout submitted to nonlinear analysis: (a) material distribution, and (b) stress distribution at deformed configuration. 92

A.1 Stress interpolation functions ($\varepsilon = 0.2$, $p = 3$, $q = 2.5$ and $\delta_\sigma = 5$). 113
A.2 Behavior of stress constraints ($\varepsilon = 0.2$ and $p - q = 0.5$). 114
A.3 P-norm-based aggregation functions: (a) P-norm, and (b) P-mean. 116
A.4 KS function-based aggregation: (a) upper bound KS function, and (b) lower bound KS function. 118
A.5 Strategies for grouping the elements: (a) mesh numbering, (b) GBT, (c), EIT, (d) a possible case in which GBT results in the same block partition as EIT, (e) stress values, (f) SDT, (g) mSDT, and (h) SLT. 120
A.6 L-bracket. 127
A.7 L-bracket material and stress distributions for P-norm, with c_p, and varying p_a. 129
A.8 P-norm as a function of aggregation parameter. 130
A.9 L-bracket material and stress distributions for P-norm, without c_p, and varying p_a. 131
A.10 L-bracket material and stress distributions for different aggregation functions and $p_a = 12$. 132
A.11 L-bracket material and stress distributions for different meshes with $p_a = 48$ and P-norm. 134
A.12 L-bracket material and stress distributions with $p_a = 12$, P-norm and different block formation methods. 138
A.13 History of (a) mass, (b) stress, (c) computing time and (d) active elements versus the number of blocks. 139
A.14 L-bracket material and stress distributions with $p_a = 48$, P-norm and different block formation methods. 141
A.15 L-bracket material and stress distributions for different mesh sizes and ALM. 142

List of Tables

2.1 Out-of-plane deformation, C_{33}, in plane stress state. 36

3.1 σ_{11} component of SVK, mSVK and nH-SC models under homogeneous uniaxial deformation. 43

6.1 Sensitivity validation. 81

7.1 MMA parameters. 82
7.2 Optimization parameters. 83
7.3 Solution parameters for U-shape. 87
7.4 Solution parameters for cantilever beam. 89
7.5 Solution parameters for crack notch beam. 91

A.1 MMA parameters used in the L-bracket example. 128
A.2 Optimization parameters used in the L-bracket example. 128
A.3 Solution parameters based on P-norm, with c_p, and varying p_a. 130
A.4 Solution parameters based on P-norm, without c_p, and varying p_a. 132
A.5 Solution parameters for different aggregation functions and $p_a = 12$. 133
A.6 Solution parameters for different mesh size and P-norm. 133
A.6 Solution parameters for different mesh sizes and ALM. 142

List of Abbreviations

AHT – Additive Hyperelasticity Technique

ALM – Augmented Lagrangian Method

EIT – Element Index Technique

EIS – Energy Interpolation Scheme

EPM – Exterior Penalty Method

FE – Finite Element

GBT – Geometry-Based Technique

KKT – Karush-Kuhn-Tucker

KS – (Upper Bound) Kreisselmeier-Steinhauser

LKS – Lower Bound Kreisselmeier-Steinhauser

LCM – Load Control Method

mSVK – Modified St. Venant-Kirchoff

mSDT – Modified Stress Distribution Technique

MMA – Method of Moving Asymptotes

MR – Mooney-Rivlin

nH-SC – Neo-Hookean of Simo-Ciarlet

NRP – Newton-Raphson Procedure

PE – Plane Strain

PS – Plane Stress

PVC – Polynomial Vanishing Constraint

RCC – Reduced Convergence Criterion

SDT – Stress Distribution Technique

SLT – Stress Level Technique

SIMP – Solid Isotropic Material with Penalization

SVK – St. Venant-Kirchoff

TVC – Traditional Vanishing Constraint

"Fairy tales are more than true: not because they tell us that dragons exist, but because they tell us dragons can be beaten."

Chesterton, C.K.
Coraline

1
Introduction

> *"If we knew what it was we were doing, it would not be called research, would it?"*
>
> **Einstein, A. (1879–1955)**

Topology optimization has risen in importance over the last three decades, and it is currently an active research topic for many academics and engineers. One might think of it as a technique for finding the ideal layout, which, in its discrete approach, comprises identifying the optimal number and location of holes within a design domain while adhering to the imposed boundary requirements. Topology optimization is suitable for modeling complex structures and has attracted special attention in the early conceptual stages of projects, where the outcome has a substantial influence and relevance on the performance of the final layout (Deaton & Grandhi, 2014).

Furthermore, topology optimization may cope with a wide variety of applications: from structural mechanics and aerodynamics, e.g. stiffness maximization, to a range of multi-physics fields – like eigenfrequency (*apud.* Eschenauer & Olhoff, 2001), buckling (Russ & Waisman, 2021; Han & Wang, 2022), or thermomechanics coupling (Meng *et al.*, 2021); from a single material to multi-material structures (Tamijani, 2021); from deterministic to probabilistic or uncertainty analyses (da Silva *et al.*, 2019, 2020a), and so on.

In this chapter, we will go over the motivation, objective, and main contributions of this dissertation. Additionally, we shall present a bibliographic overview and provide the nomenclature used in the text. Lastly, we provide you with the remainder of this dissertation.

1.1
Motivation

In recent years, academics have been interested in the application of topology optimization to fulfill specific types of strength requirements, primarily to target allowable stresses under the premise of small deformations. This is a natural way of thinking. As strength is paramount for security and service life, designers do not want their structure to fail under certain conditions.

To demonstrate the significance of strength criteria, consider Figure 1.1 with the optimization of an aircraft bracket under stable load cases and linear analyses. The original structure of Figure 1.1(a) (with red loads from the supported oil tank and blue for clamped installation holes) has a maximum stress of 50.04 MPa – *vid.* Figure 1.1(b). This layout differs from the one attained by interpreting the optimized stress-constrained topology of Figure 1.1(c) which has a peak stress of 34.62 MPa according to Figure 1.1(d).

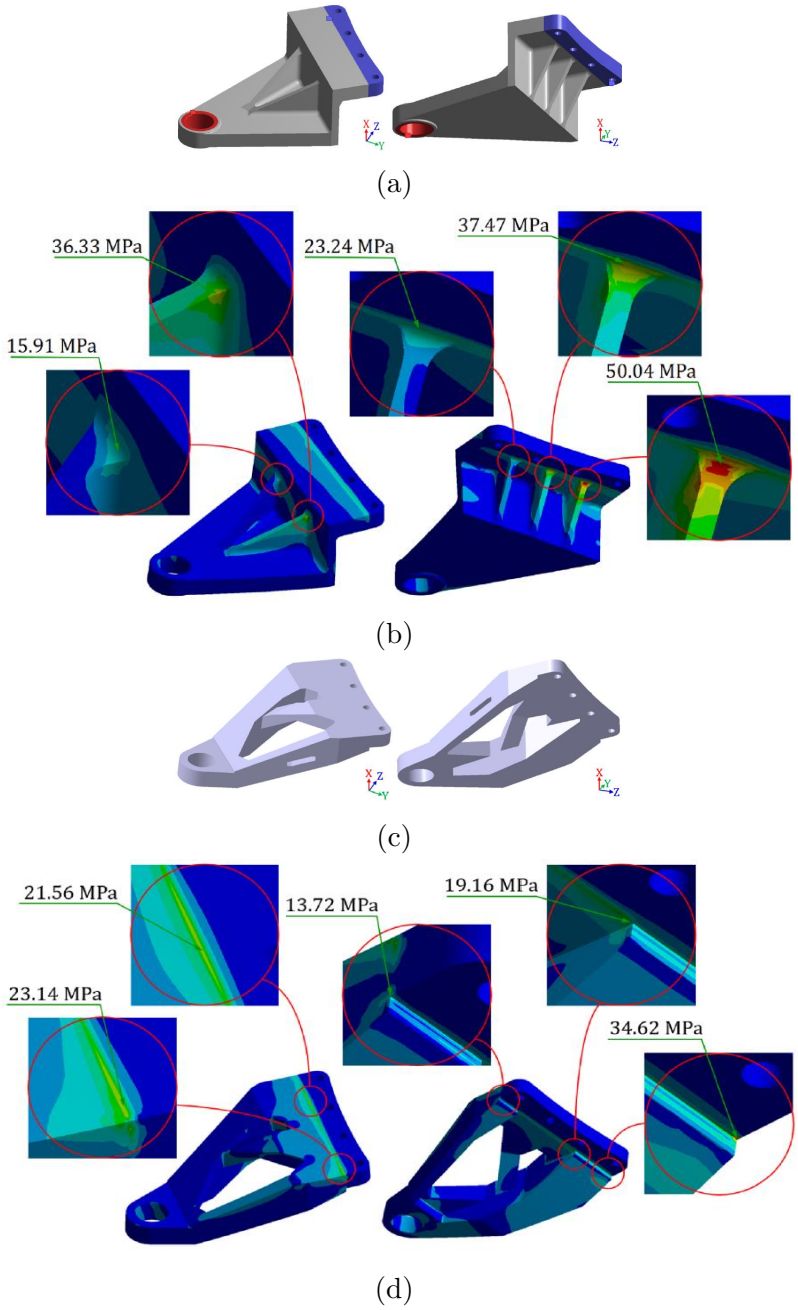

Figure 1.1: Aircraft engine bracket: (a) original design, (b) von Mises stress distribution of (a) considering the worst load scenario, (c) reconstruction of stress-constrained topology, and (d) von Mises stress field of (c) also in the worst load case scenario (adapted from Wu *et al.*, 2021).

On the other hand, numerous structures or mechanisms exhibit some degree of nonlinearity. This is the case of soft robots built of soft and/or extensible materials, such as the case of silicone rubbers (Rus & Tolley, 2015; Chen *et al.*, 2017). For instance, consider the soft gripper in Figure 1.2(a). The optimal layout should withstand significant displacements, as seen in Figure 1.2(b).

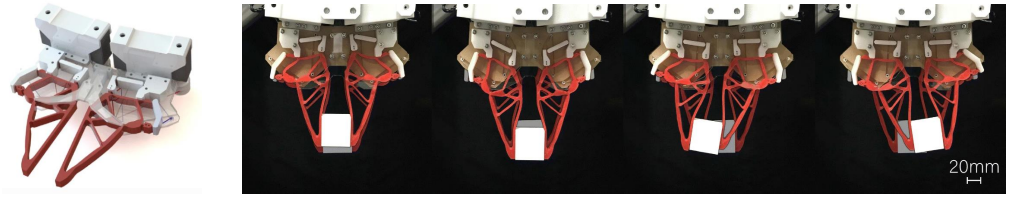

(a) (b)

Figure 1.2: Soft gripper optimized by Wang *et al.* (2020): (a) optimal design and (b) testing manufactored gripper for large deformations in each in-plane direction.

These two research fields can complement one another, allowing us to handle both strength and nonlinearities in the same optimization problem formulation. Nonetheless, each of them has distinct challenges that need to be appropriately addressed throughout the topology optimization process.

1.2 Objectives

The primary purpose of this dissertation is to present consistent solutions for stress-constrained topology optimization under geometrical and material nonlinear analysis. The material nonlinearity is computed for hyperelastic models using the well-established theory of continuum mechanics and takes advantage of the implementation of finite element (FE) analysis.

We also analyze the stress derivatives – notably the derivative of Cauchy stress with respect to (w.r.t.) the displacement field – required by gradient-based optimizers. This allows us to properly compute the derivatives regardless of whether we are assuming plane stress, plane strain, or three-dimensional scenarios.

1.3 Main Contributions

For convenience and easier comprehension, we separate the main contributions of this dissertation into the following:

- development of a computational framework for stress-constrained topology optimization of hyperelastic structures;

- inner routine to tackle the out-of-plane strain deformation in plane stress scenarios;
- comparative study to look at the various methods employed in stress-constrained topology optimization problems;
- description of an approach for dealing with numerical instability in low-stiffness zones of the mesh;
- proper and detailed analytical sensitivity computation;
- examples based on real-world material parameters.

1.4 Literature Review

Only a few studies have coupled strength criteria with nonlinear analyses. Deng *et al.* (2019) advocated that the strain energy density function of hyperelastic material models tends to increase without bounds, hence the strain energy cannot account for softening at large strains. This tendency, though, is nonphysical since no substance can store unlimited energy without failure. Given this scenario, they instructed limiting the failure energy of soft materials in their optimization formulation.

Many hyperelastic models are either incompressible or nearly-incompressible, so it is reasonable to infer that they preserve volume, with only the distortion component of the strain energy being significant[1]. The assumption of minimizing the strain energy then seems reasonable. The strain energy limit must be computed properly as the area of the stress-strain curve from the undeformed state to a desired point in tensile, compression, bending, or shear tests. Nevertheless, unlike stress limits, there are no standards for determining or estimating a material's strain energy limit, thus requiring experimental tests. Otherwise, we will be talking about fiction.

Following this scope, the study of Deng *et al.* (2020) focused on designing energy dissipation in lattice structures exploiting snap-through behavior. The premise lies in the soft materials' ability to absorb energy, making them effective as dampers or impact-prevention devices. A dual optimization strategy is developed; the first ensures that the structure has an initial snap-through point, and the second optimizes theoretical energy absorption while limiting the strain energy to prevent material failure. The procedure is consistent but limited to: (i) the computation of the absorbed energy, which is based on an

[1]The von Mises failure criterion is equal to the distortion energy criterion only when the assumption of infinitesimal strains is valid.

approximation of the contained area in the graphic force x displacement, and (ii) the empirical strain energy limit.

Ye *et al.* (2021) explored Deng *et al.* (2019)'s idea, converting local stress constraints into strain energy constraints and calculating the allowable yielding strain energy limit. During the research, they observed that the optimized designs still had stresses over the limit at the loading point and fixed boundaries, so they introduced a correction coefficient to the strain, decreasing the elements that exceeded the yield stress. Unfortunately, this coefficient depends on two constants derived from numerical experience – which, in our judgment, can vary substantially depending on the imposed boundary conditions and material properties. Furthermore, one must investigate the update conditions for the material parameters utilized in the additive hyperelastic technique (AHT) of Chen *et al.* (2019), employed to deal with substantial distortions of low-stiffness zones.

Solving compliant mechanisms is also a typical practice. These devices transfer part of the elastic strain from the input stimulus into kinematic motion, demanding accurate analyses following finite deformation assumptions. Furthermore, the strength requirements are beneficial for reducing the appearance of node-to-node connected hinges (de Leon *et al.*, 2015). In this context, we highlight a few studies that employed the density-based topology optimization formulation to address problems with global stress measures.

In Große (2019), the mechanism's output displacement was maximized while limiting the maximum stress and allowable material quantity. The P-norm was utilized to approximate the peak of relaxed stresses, and the energy interpolation scheme (EIS) from Wang *et al.* (2014) was implemented for coping with numerical instabilities in low-stiffness elements.

Capasso *et al.* (2020) suggested two optimization problems: minimizing material under stress, displacement, and/or compliance limitations, and optimizing relative displacement for stress and compliance constraints. Their research relies on a neo-Hookean model to achieve convergence of the Newton-Raphson iterations, as well as the unified aggregation and relaxation method from Verbart *et al.* (2017).

The work of de Leon *et al.* (2020) concentrated on maximizing displacement under stress and volume constraints. The P-norm was used to approximate the maximal stress, which was then relaxed using the *qp*-approach (Bruggi, 2008). The convergence of the nonlinear procedure also relies on the neo-Hookean material model adopted.

Reinisch *et al.* (2021) expanded Große (2019)'s approach for the multiresolution formulation (Nguyen *et al.*, 2010) to minimize computational costs for

high-resolution topologies – as they themselves state. Han *et al.* (2021) added stress constraints to the compliance minimization problem with geometrical and material nonlinearities, modeling the stress-strain relationship after yielding by a power law. They dealt with numerical difficulties at quasi-voids[2] using the bi-directional evolutionary structural optimization (BESO) technique. However, it is not clear which stress is being restricted.

Stankiewicz *et al.* (2022) combined both topology and shape optimization to build precise hinge designs for compliant mechanisms. Density-based topology optimization was used as an early process, resulting in a crude first design with coarse discretizations. At this stage, the authors aim to maximize a specified output displacement while limiting the amount of material. After proper interpretation, shape optimization was added to the formulation to enhance boundary representation – particularly the existence of blurred material with artificial stress. Here, the authors minimized the same degree of freedom while imposing curvature and stress constraints. The EIS was applied to cope with instabilities in quasi-void elements; meanwhile, stresses were handled as local quantities in an augmented Lagrangian formulation. As a result, this work modeled precise and smooth flexure hinges for compliant mechanisms by incorporating curvature constraints, which reduced the maximum stress.

All of the detached researches focus exclusively on two-dimensional analysis. But what worries us the most is that none of them demonstrated consistency in three-dimensional sensitivity studies. Even while the strain energy-based studies sound encouraging, further research is required as they cannot ensure that the stress will be within the allowable level. Since the author has no experience with shape optimization, using a framework for sequential topology and shape optimization is not practical. Nevertheless, it is still an excellent option.

1.5 Notation

Throughout this dissertation, we use proper notation to describe a range of quantities necessary at different phases of the study. Hence, we decided that the following form is the most acceptable for dealing with the involved quantities.

Scalars, or zeroth-order tensors, are written as plain text with no index:

$$c = a + b. \tag{1.1}$$

Vectors, or first-order tensors, are represented by small caption characters

[2]We refer to quasi-voids as the zones within the design domain with no material. This term is also known as low-stiffness or low-density elements.

in direct or tensor notation, or by a single subscript in index notation:

$$\boldsymbol{v} \Leftrightarrow v_i = \begin{bmatrix} v_1 \\ v_2 \\ v_3 \\ \vdots \\ v_n \end{bmatrix}. \tag{1.2}$$

The index is always a letter. In cases where it is a number, we are referring to a specific component. For example, v_1 corresponds to the first term of the vector v_i.

Second-order tensor components in a given basis can be written as matrices in the form of

$$\boldsymbol{M} \Leftrightarrow M_{ij} = \begin{bmatrix} M_{11} & M_{12} & M_{13} & \cdots & M_{1n} \\ M_{21} & M_{22} & M_{23} & \cdots & M_{2n} \\ M_{31} & M_{32} & M_{33} & \cdots & M_{3n} \\ & & \vdots & & \\ M_{m1} & M_{m2} & M_{m3} & \cdots & M_{mn} \end{bmatrix}. \tag{1.3}$$

Therefore, it is represented by capital letters in direct notation, and requires double digits in index notation. In cases, where dealing with physical quantities, $m, n \leqslant 3$.

We define fourth-order tensors as those with four indexes. This is the case for the elasticity tensor: $\boldsymbol{\mathcal{D}} \Leftrightarrow \mathcal{D}_{ijkl}$.

Symmetries can also be exploited to represent these quantities in a more concise format via Voigt notation. In this case, the components of a tensor $\boldsymbol{M}$ simplifies to

$$\mathsf{M} \Leftrightarrow \mathsf{M}_i = \begin{bmatrix} M_{11} \\ M_{22} \\ M_{33} \\ M_{12} \\ M_{23} \\ M_{13} \end{bmatrix}, \tag{1.4}$$

utilizing the 'Sans Serif' font. Likely, fourth-order tensors can be rewritten in matrix form (*vid.* Equation (2.26) of Section 2.4).

1.6 Outline

The organization of this dissertation is as follows:

Chapter 2 covers the fundamentals of continuum mechanics, while Chapter 3 introduces the FE implementation necessary to solve the state problem.

Chapter 4 details the basis of the density-based topology optimization procedures, whereas Chapter 5 discusses the main considerations involving stresses in this type of optimization. Chapter 6 shows the main formulation for the problem discussed in this dissertation and checks the sensitivity. Chapter 7 solves several problems to evaluate our formulation's capabilities, and, finally, Chapter 8 summarizes the main points and discusses future perspectives.

2
The Basics of Continuum Mechanics

"The noblest pleasure is the joy of understanding."

da Vinci, L.d.s.P. (1452–1519)

This chapter is dedicated to the basics of continuum mechanics, that is, we are interested in macroscopic behavior. Starting from the deformation gradient, we then introduce strain and stress measures. In the end, we detail the definition of hyperelastic materials and the main concepts required for the development of this dissertation, especially the computation of stress and constitutive relations from the strain measure. We have made some simplifications, so the more demanding reader can consult other references, like Lawrence (1969), Mase & Mase (1999), Holzapfel (2000) or Reddy (2008), among others.

2.1
Deformation

Consider Figure 2.1 representing a (continuum) body, $\mathcal{B}$. This body is made of a set of material points (or particles[3]), P. At the time $t = 0$, the particle P occupies a space position $\boldsymbol{X}$ from the inertial frame, and we say $\mathcal{B}$ is in the undeformed or reference configuration, ${}^0\Omega$.

Under the action of external stimuli, the body $\mathcal{B}$ will naturally occupy another position in space, and that same particle is now defined by the vector $\boldsymbol{x}$. Since it happens at a subsequent time $t > 0$, $\mathcal{B}$ occupies a region ${}^t\Omega$ called deformed or current configuration.

These two configurations induce a deformation mapping $\boldsymbol{\chi}(\boldsymbol{X}, t)$ from ${}^0\Omega \rightarrow {}^t\Omega$. This mapping is invertible, $\boldsymbol{\chi}^{-1}(\boldsymbol{x})$, and establishes a unique relation between the particle P at ${}^0\Omega$ and its counterpart p at ${}^t\Omega$. Then,

$$\begin{aligned} \boldsymbol{x} &= \boldsymbol{\chi}(\boldsymbol{X}, t) \quad \text{or} \quad x_a = \chi_a(X_1, X_2, X_3, t), \quad \text{and} \\ \boldsymbol{X} &= \boldsymbol{\chi}^{-1}(\boldsymbol{x}) \quad \text{or} \quad X_A = \chi_A^{-1}(x_1, x_2, x_3). \end{aligned} \tag{2.1}$$

Note that we use lowercase indexes to represent material (or referential) coordinates, while the uppercase ones refer to spatial (or current) coordinates.

[3]The concept of a particle in continuum mechanics refers to a part of a body, and, differently from Newtonian physics, it does not possess mass.

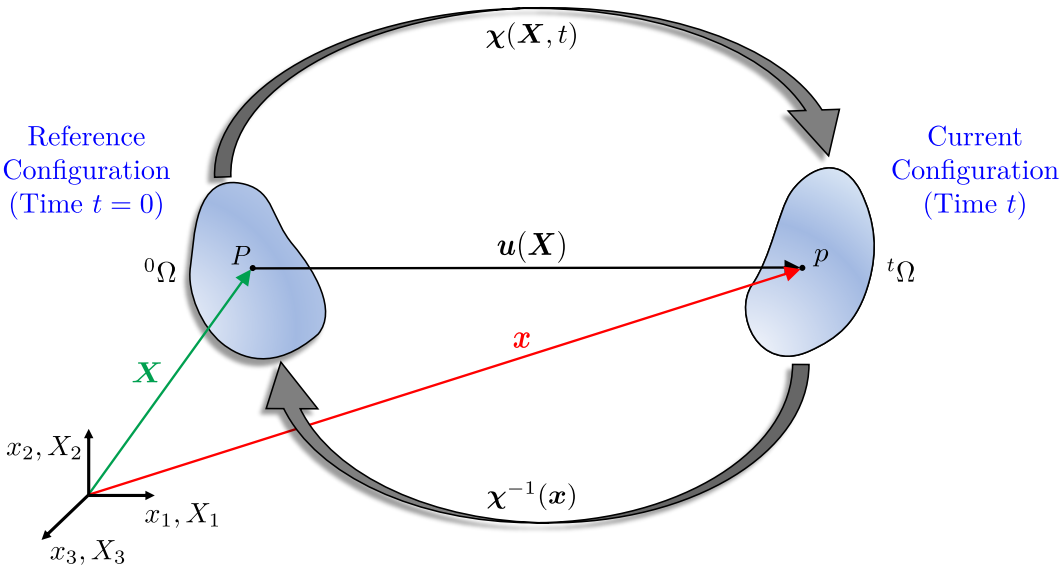

Figure 2.1: Displacement field of a typical particle.

To study the deformation, the position in both configurations must be known. The initial configuration is convenient and intuitively selected to be the undeformed state, devoid of external stimuli. If this is the case, we employ the Lagrangian description, in which motion analyses take into account the reference configuration.

Then, the displacement vector field is given by

$$\boldsymbol{u}(\boldsymbol{X}) = \boldsymbol{x} - \boldsymbol{X}, \tag{2.2}$$

where $\boldsymbol{u}$ describes the motion from the reference to the current configuration.

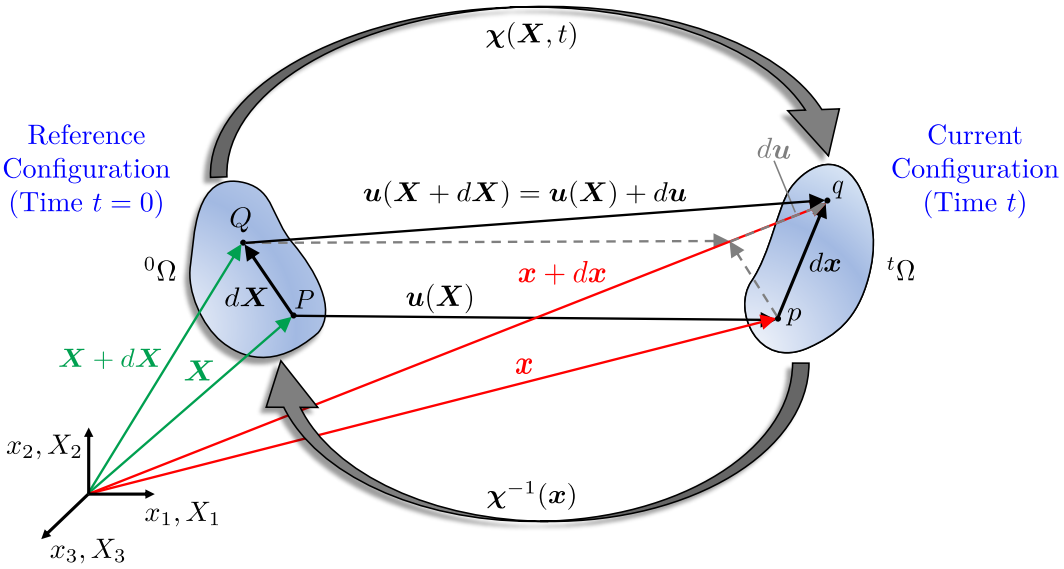

Figure 2.2: Displacement of a material fiber into a spatial fiber.

As pointed out by Albertyne (2014), the deformation of $\boldsymbol{X}$ does not solely depend on its position but also the deformation of all particles within a small

neighborhood of $\boldsymbol{X}$. In this sense, consider Figure 2.2. The infinitesimal fiber $d\boldsymbol{X}$ joins the material points P and Q in the reference configuration, while the fiber $d\boldsymbol{x}$ represents those same points p and q in the current configuration.

In the current configuration, we have

$$\overrightarrow{pq} = d\boldsymbol{x} = \boldsymbol{x} + d\boldsymbol{x} - \boldsymbol{x} = \boldsymbol{\chi}(\boldsymbol{X} + d\boldsymbol{X}) - \boldsymbol{\chi}(\boldsymbol{X}), \tag{2.3}$$

where the time t is dropped, as we are not interested in the sequence of deformations but only in the final state. Assuming the difference between p and q is infinitesimal, we can rewrite the right-hand side of Equation (2.3) using the Taylor expansion,

$$\boldsymbol{\chi}(\boldsymbol{X} + d\boldsymbol{X}) - \boldsymbol{\chi}(\boldsymbol{X}) = \nabla_0 \boldsymbol{\chi}(\boldsymbol{X} + d\boldsymbol{X}) d\boldsymbol{X} + \mathcal{O}(d\boldsymbol{X}^2),$$

where ∇_0 identifies the gradient w.r.t. the undeformed configuration.

Thus,

$$d\boldsymbol{x} = \nabla_0 \boldsymbol{\chi}(\boldsymbol{X} + d\boldsymbol{X}) d\boldsymbol{X} + \mathcal{O}(d\boldsymbol{X}^2), \quad \text{with}$$
$$\nabla_0 \boldsymbol{\chi} = \frac{\partial \boldsymbol{\chi}(\boldsymbol{X} + d\boldsymbol{X})}{\partial \boldsymbol{X}} = \frac{\partial \boldsymbol{x}}{\partial \boldsymbol{X}}.$$

Neglecting high-order terms, we end up with an expression relating an infinitesimal undeformed fiber, $d\boldsymbol{X}$, to its location in the deformed configuration, $d\boldsymbol{x}$,

$$d\boldsymbol{x} = \boldsymbol{F} d\boldsymbol{X}, \quad \text{where} \quad \boldsymbol{F} \coloneqq \frac{\partial \boldsymbol{x}}{\partial \boldsymbol{X}} \quad \text{or} \quad F_{aA} \coloneqq \frac{\partial x_a}{\partial X_A}, \tag{2.4}$$

is the *deformation gradient tensor*.

With the help of Equation (2.2), the relation of Equation (2.4) may be conveniently rewritten in terms of the *displacement gradient tensor*, $\boldsymbol{G}$, as

$$\boldsymbol{F} = \boldsymbol{G} + \boldsymbol{I} = \frac{\partial \boldsymbol{u}}{\partial \boldsymbol{X}} + \boldsymbol{I} \quad \text{or} \quad F_{aA} = G_{aA} + \delta_{aA} = \frac{\partial u_a}{\partial X_A} + \delta_{aA}, \tag{2.5}$$

in which $\boldsymbol{I}$ is the first-order identity tensor and

$$\delta_{aA} = \begin{cases} 1, & \text{if } a = A; \\ 0, & \text{if } a \neq A \end{cases} \tag{2.6}$$

is the Kronecker delta.

Finally, we emphasize that this theory does not even expect that: (i) a single fiber $d\boldsymbol{X}$ divides into two or more fibers $d\boldsymbol{x}^{(1)}, \ldots, d\boldsymbol{x}^{(n)}$, for $n > 1$, and (ii) neither two or more fibers $d\boldsymbol{X}^{(1)}, \ldots, d\boldsymbol{X}^{(n)}$ coalesces into a single fiber $d\boldsymbol{x}$. Mathematically, this information appears in the Jacobian,

$$J = \det(\boldsymbol{F}) > 0. \tag{2.7}$$

Therefore, J cannot vanish to preserve the reversibility of $\boldsymbol{\chi}$, and $J > 0$; otherwise, material may disappear or change the fiber orientation after

deformation.

2.2 Strain Measures

An objective measure of deformation should be unaffected by rigid body translation or rotation. Then, several measures of deformation were constructed throughout the years. Here, we will go over two of them.

The squared distance between particles p and q in the current configuration is

$$\begin{aligned} ||d\boldsymbol{x}||^2 &= (F_{kI}dX_I)(F_{kJ}dX_J) \\ &= F_{kI}F_{kJ}dX_IdX_J \\ &= C_{IJ}dX_IdX_J, \end{aligned} \tag{2.8}$$

where the *right Cauchy-Green deformation tensor* comes from:

$$\boldsymbol{C} = \boldsymbol{F}^T\boldsymbol{F} \quad \text{or} \quad C_{IJ} = F_{kI}F_{kJ}. \tag{2.9}$$

Now assume the deformation is given by the squared length of the distance between the particles P and Q, in both reference and current configurations. Thus,

$$\begin{aligned} ||d\boldsymbol{x}||^2 - ||d\boldsymbol{X}||^2 &= (F_{kI}dX_I)(F_{kJ}dX_J) - dX_IdX_J \\ &= F_{kI}F_{kJ}dX_IdX_J - \delta_{IJ}dX_IdX_J \\ &= (C_{IJ} - \delta_{IJ})dX_IdX_J. \end{aligned} \tag{2.10}$$

The quantity inside the parentheses is two times the so-called *Green-Lagrange strain tensor*,

$$\boldsymbol{E} = \frac{1}{2}(\boldsymbol{C} - \boldsymbol{I}) \quad \text{or} \quad E_{IJ} = \frac{1}{2}(C_{IJ} - \delta_{IJ}). \tag{2.11}$$

In terms of the displacement field, Equation (2.11) becomes

$$\begin{aligned} \boldsymbol{E} &= \frac{1}{2}\left(\nabla_0\boldsymbol{u} + \nabla_0\boldsymbol{u}^T + \nabla_0\boldsymbol{u}^T\nabla_0\boldsymbol{u}\right) \quad \text{or} \\ E_{IJ} &= \frac{1}{2}\left(u_{I,J} + u_{J,I} + u_{K,J}u_{K,I}\right). \end{aligned} \tag{2.12}$$

The main difference between tensors $\boldsymbol{C}$ and $\boldsymbol{E}$ is in the no-deformation scenario when $\boldsymbol{E} = \boldsymbol{0}$ and $\boldsymbol{C} = \boldsymbol{I}$. Notice that: (i), from the definition of $\boldsymbol{C}$,

$$\det(\boldsymbol{C}) = det(\boldsymbol{F}^T\boldsymbol{F}) = \det(\boldsymbol{F}^T)\det(\boldsymbol{F}) = J^2, \tag{2.13}$$

and (ii) due to the symmetries, we can set down

$$\mathsf{C} = \begin{bmatrix} C_{11} & C_{22} & C_{33} & C_{12} & C_{23} & C_{13} \end{bmatrix}^T \quad \text{and} \tag{2.14}$$

$$\mathsf{E} = \begin{bmatrix} E_{11} & E_{22} & E_{33} & 2E_{12} & 2E_{23} & 2E_{13} \end{bmatrix}^T, \tag{2.15}$$

which are of particular interest in the development of FE equations.

Remark the shear components of $\mathbf{E}$ are multiplied by 2. This is convenient when we want to express a linear relation between the stresses and strains: $\mathbf{S} = \mathbf{DE}$, in which $\mathbf{S}$ is written in the same format of Equation (2.14) and $\mathbf{D}$ follows Equation (2.26).

2.2.1 Strain Principal Invariants

Isotropic materials are those whose properties are unaffected by changes of basis, i.e., remain the same regardless of the direction (Truesdell & Noll, 1992). For instance, the principal invariants of tensor $\boldsymbol{C}$ are

$$I_1 = \mathrm{tr}(\boldsymbol{C}) = C_{II}, \tag{2.16a}$$

$$I_2 = \frac{1}{2}\left[\mathrm{tr}^2(\boldsymbol{C}) - \mathrm{tr}(\boldsymbol{C}^2)\right] = \frac{1}{2}\left[C_{II}C_{JJ} - C_{IJ}C_{JI}\right], \quad \text{and} \tag{2.16b}$$

$$I_3 = \det(\boldsymbol{C}) = J^2 = \epsilon_{IJK}\epsilon_{1I}\epsilon_{2J}\epsilon_{3K} \quad (\epsilon \text{ is the permutation symbol}), \tag{2.16c}$$

designated as the coefficients of the polynomial function

$$\det(\boldsymbol{C} - \Lambda\boldsymbol{I}) = \Lambda^3 + I_1\Lambda^2 + I_2\Lambda + I_3.$$

We may also write their volumetric counterparts, which do not depend on the dilation, known as reduced or modified invariants (*vid.* Holzapfel, 2000, p. 233):

$$\tilde{I}_1 = J^{-2/3}I_1, \tag{2.17a}$$

$$\tilde{I}_2 = J^{-4/3}I_2, \tag{2.17b}$$

$$\tilde{I}_3 = J^{-6/3}I_3 = 1. \tag{2.17c}$$

Remark in Equation (2.17c), we use the definition of Equation (2.16c).

2.3 Stress Measures

We start looking at a deformed body at a certain time t. This body occupies an arbitrary region ${}^t\Omega$ in the space and is enclosed by $\partial{}^t\Omega$. If we cut it in any arbitrary position, we will end up with two portions. Each of these portions will interact with each other, and we assume the existence of a force $\Delta\boldsymbol{f}$ located at point p, with spatial coordinates x_i from the inertial frame, as shown in Figure 2.3.

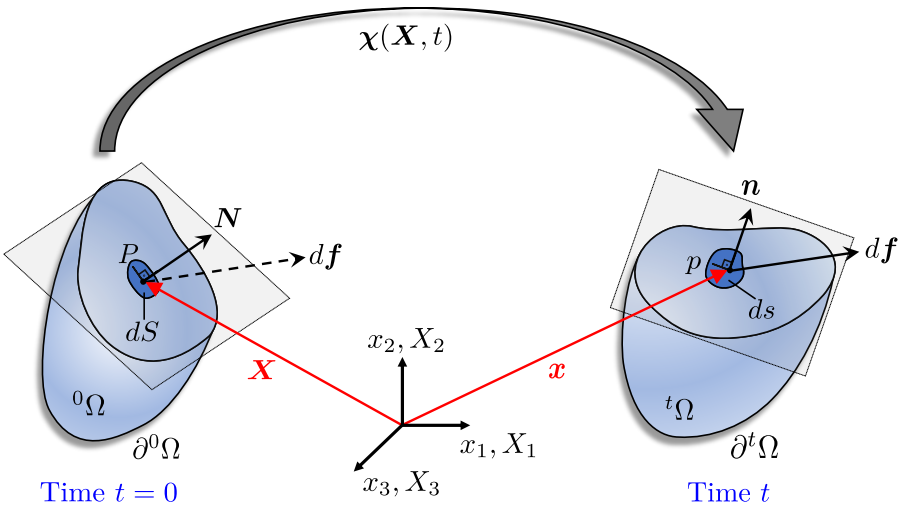

Figure 2.3: Element of area under deformation.

If the force $\Delta \boldsymbol{f}$ is acting on a small element of area denoted by $\Delta \boldsymbol{s} = \Delta s \boldsymbol{n}$, in which $\boldsymbol{n}$ is the unit outward normal, then the stress (or traction) vector can be described as

$$\boldsymbol{t}(\boldsymbol{n}, t) = \lim_{\Delta s \to 0} \frac{\Delta \boldsymbol{f}(\boldsymbol{n})}{\Delta s} = \frac{d\boldsymbol{f}(\boldsymbol{n})}{ds}, \quad \text{for} \quad t > 0, \tag{2.18}$$

where $d\boldsymbol{f}(\boldsymbol{n})$ is the force associated with the infinitesimal area in the current configuration ds.

This stress depends on the normal, $\boldsymbol{n}$. Nevertheless, as commented by Reddy (2008) "the stress tensor is a property of the medium that is independent of $\boldsymbol{n}$". To eliminate this dependence, we resort to the Cauchy stress formula, an axiom establishing that

$$\boldsymbol{t}(\boldsymbol{n}, t) = \boldsymbol{\sigma}(t)\boldsymbol{n} \quad \text{or} \quad t_i = \sigma_{ij} n_j, \tag{2.19}$$

where $\boldsymbol{\sigma}$ is the *Cauchy (or true) stress tensor*.

The term 'true' comes as a reminder from its definition: the relation of current force per unit of deformed area. σ_{ij} designates the stress on a plane perpendicular to the ith-coordinate and in the direction of jth-coordinate, for $i, j = 1, 2, 3$. Furthermore, it is symmetric, which allows us to rewrite it in the same manner as Equation (2.14).

By extending the above idea to a body in the undeformed state (see again Figure 2.3) we found that

$$d\boldsymbol{f} = \boldsymbol{t}(\boldsymbol{n}, t) ds = \boldsymbol{T}(\boldsymbol{N}) dS,$$

where $\boldsymbol{T}$ is the traction vector and $\boldsymbol{N}$ is the unit outward normal, both in the reference configuration. Here, $d\boldsymbol{f}$ has the same direction regardless of the configuration, but the magnitude is not preserved from one to another.

Using once more the Cauchy's formula, we introduce another stress measure, $\boldsymbol{P}$, the *first Piola-Kirchhoff (or PK1 or nominal) stress tensor*:

$$\boldsymbol{T}(\boldsymbol{N}) = \boldsymbol{P}\boldsymbol{N} \quad \text{or} \quad T_I = P_{iJ}N_J. \tag{2.20}$$

Here, we are still considering the current force $d\boldsymbol{f}$. This happens because $\boldsymbol{P}$ takes into account the effect of imposing $d\boldsymbol{f}$ on the undeformed configuration. In this sense, the PK1 stress tensor is responsible for relating the current force per unit of undeformed area – as one can observe by the lowercase and uppercase indexes – and, as a consequence, PK1 stress is not symmetric.

In several analyses, though, $\boldsymbol{P}$ is not a suitable measure since the force $d\boldsymbol{f}$ is unknown at time $t = 0$. A new stress metric is required. This is the *second Piola-Kirchhoff (or PK2 or material) stress tensor*, $\boldsymbol{S}$, which associates the force $d\boldsymbol{\mathcal{F}}$ with its infinitesimal area in the undeformed configuration, dS:

$$d\boldsymbol{\mathcal{F}} = \boldsymbol{S}d\boldsymbol{S} = \boldsymbol{S}dS\boldsymbol{N}.$$

PK2 is a symmetric tensor and is a fundamental stress measure, especially in the study of solid mechanics. The relationship[4] between all the mentioned stress tensors is:

$$\boldsymbol{S} = \boldsymbol{F}^{-1}\boldsymbol{P} = J\boldsymbol{F}^{-1}\boldsymbol{\sigma}\boldsymbol{F}^{-T}. \tag{2.21}$$

2.3.1 Equivalent Stress

The measure considered herein is the von Mises equivalent stress, defined as

$$\sigma_j^{vM} = \sqrt{\boldsymbol{\sigma}_j^T \boldsymbol{V} \boldsymbol{\sigma}_j}, \tag{2.22}$$

for

$$\boldsymbol{\sigma}_j = \begin{bmatrix} \sigma_{11} & \sigma_{22} & \sigma_{33} & \sigma_{12} & \sigma_{23} & \sigma_{13} \end{bmatrix}^T,$$

and

$$\boldsymbol{V} = \begin{bmatrix} 1 & -\frac{1}{2} & -\frac{1}{2} & 0 & 0 & 0 \\ -\frac{1}{2} & 1 & -\frac{1}{2} & 0 & 0 & 0 \\ -\frac{1}{2} & -\frac{1}{2} & 1 & 0 & 0 & 0 \\ 0 & 0 & 0 & 3 & 0 & 0 \\ 0 & 0 & 0 & 0 & 3 & 0 \\ 0 & 0 & 0 & 0 & 0 & 3 \end{bmatrix}. \tag{2.23}$$

[4]Operations transforming variables from the reference configuration to the current configuration are known as *push-forward*. The inverse is the *push-back* operation.

This approach is valid provided the deformations are reversible since it disregards the effects of hydrostatic stresses. Also note that the von Mises stresses are stated in terms of the Cauchy values, which require stress transformation given in Equation (2.21).

2.4 Hyperelasticity

Elastic materials are characterized when, upon removal of the external stimuli – in general, an applied force – the body recovers its original configuration. An *simple elastic or Cauchy elastic* material is one whose state of stress in the current configuration is uniquely determined by its state of deformation relative to the reference configuration.

Hyperelastic or Green elastic constitutive laws encounter their major application to model rubbery behavior or polymeric foams under large reversible changes of shape. Traditionally, hyperelastic solids presume the existence of a *strain (or stored) energy density function* per unit undeformed volume, W. As its name suggests, W is the energy stored in the material as a result of deformations under consistent thermodynamic conditions (Mooney, 1940; Bower, 2009).

If we treat the material as homogeneous, then the strain energy can be computed solely from deformation metrics. Considering $\boldsymbol{C}$ to be the strain measure, then we have that $W \equiv W(\boldsymbol{C})$.

The tensors $\boldsymbol{S}$ and $\boldsymbol{E}$ are work-conjugated (Hackett, 2016). So, we can define the PK2 stress tensor as

$$\boldsymbol{S} = \frac{\partial W}{\partial \boldsymbol{E}} = 2\frac{\partial W}{\partial \boldsymbol{C}} \quad \text{or} \quad S_{IJ} = \frac{\partial W}{\partial E_{IJ}} = 2\frac{\partial W}{\partial C_{IJ}}, \tag{2.24}$$

and the elasticity tensor as

$$\boldsymbol{\mathcal{D}} = \frac{\partial^2 W}{\partial \boldsymbol{E}\partial \boldsymbol{E}} = 4\frac{\partial^2 W}{\partial \boldsymbol{C}\partial \boldsymbol{C}} \quad \text{or} \quad \mathcal{D}_{IJKL} = \frac{\partial^2 W}{\partial E_{IJ}\partial E_{KL}} = 4\frac{\partial^2 W}{\partial C_{IJ}\partial C_{KL}}. \tag{2.25}$$

Tensor $\boldsymbol{\mathcal{D}}$ has $3^4 = 81$ components. Assuming the material is also isotropic, only 21 of its terms are independent (Lawrence, 1969). Exploiting this effect, we are able to condense it in matrix form as

$$\mathbf{D} \Leftrightarrow \mathsf{D}_{IJ} = \begin{bmatrix} \mathcal{D}_{1111} & \mathcal{D}_{1122} & \mathcal{D}_{1133} & \mathcal{D}_{1112} & \mathcal{D}_{1123} & \mathcal{D}_{1113} \\ & \mathcal{D}_{2222} & \mathcal{D}_{2233} & \mathcal{D}_{2212} & \mathcal{D}_{2223} & \mathcal{D}_{2213} \\ & & \mathcal{D}_{3333} & \mathcal{D}_{3312} & \mathcal{D}_{3323} & \mathcal{D}_{3313} \\ & & & \mathcal{D}_{1212} & \mathcal{D}_{1223} & \mathcal{D}_{1213} \\ & \text{sym.} & & & \mathcal{D}_{2323} & \mathcal{D}_{2313} \\ & & & & & \mathcal{D}_{1313} \end{bmatrix}. \tag{2.26}$$

Sometimes Equations (2.24) and (2.25) may not be the most convenient way to express W. From isotropy, the stored energy can be described in terms of the invariants of a deformation tensor. Considering the right Cauchy-Green tensor, $\boldsymbol{C}$, then, we may establish that

$$W(\boldsymbol{C}) \equiv W(I_1, I_2, J), \tag{2.27}$$

where I_3 was replaced by J for convenience.

From Equation (2.27), we have now

$$\boldsymbol{S} = 2\left(\frac{\partial W}{\partial I_1}\frac{\partial I_1}{\partial \boldsymbol{C}} + \frac{\partial W}{\partial I_2}\frac{\partial I_2}{\partial \boldsymbol{C}} + \frac{\partial W}{\partial J}\frac{\partial J}{\partial \boldsymbol{C}}\right) \tag{2.28}$$

and, of course,

$$\boldsymbol{\mathcal{D}} = 2\left(\frac{\partial \boldsymbol{S}}{\partial I_1}\frac{\partial I_1}{\partial \boldsymbol{C}} + \frac{\partial \boldsymbol{S}}{\partial I_2}\frac{\partial I_2}{\partial \boldsymbol{C}} + \frac{\partial \boldsymbol{S}}{\partial J}\frac{\partial J}{\partial \boldsymbol{C}}\right) \tag{2.29}$$

for

$$\frac{\partial I_1}{\partial \boldsymbol{C}} = \boldsymbol{I}, \tag{2.30a}$$

$$\frac{\partial I_2}{\partial \boldsymbol{C}} = I_1\boldsymbol{I} - \boldsymbol{C} \quad \text{and} \tag{2.30b}$$

$$\frac{\partial J}{\partial \boldsymbol{C}} = \frac{1}{2}J\boldsymbol{C}^{-1}. \tag{2.30c}$$

Equations (2.28), (2.29) and (2.30) are very popular forms to tackle the constitutive relations (*cf.* Bonet & Wood, 2008, p. 160–165). Nevertheless, we developed a MATLAB tool called `HyperSym` that automates the computation of tensors $\boldsymbol{S}$ and $\boldsymbol{\mathcal{D}}$: we express the strain energies in terms of their invariants and automatically replace each of them with the components of C_{IJ}, from which we calculate the derivatives, term by term. Then, we end up with a MATLAB file containing the required tensors. For more details, please refer to Fontes *et al.* (to appear).

Some hyperelastic materials, as is the case of foams, are modeled considering a certain level of compressibility. On the other hand, rubbers usually resist changes in volume. To account for this effect, the stored energy is typically described by three formulations, as detailed below.

2.4.1 Incompressible Formulations

Materials whose volume is constant during motion are conveniently approximated as perfectly incompressible. In this case, they are usually characterized by the constraint $J = 1$.

When we apply pressure to incompressible solids, they respond with relevant changes of shape. It implies that their stress-strain laws only account

for the distortion effects. To maintain the incompressibility, one will find the hydrostatic (or spherical) pressure, p, must be added to the Cauchy stress,

$$\boldsymbol{\sigma}(\boldsymbol{C}, p) = 2J^{-1}\boldsymbol{F}\frac{\partial W}{\partial \boldsymbol{C}}\boldsymbol{F}^T - p\boldsymbol{I}, \tag{2.31}$$

where Equation (2.21) is applied to convert $\boldsymbol{S}$ to $\boldsymbol{\sigma}$, and the scalar p is determined from the equilibrium and boundary conditions. We direct the interested reader to take a look at the book of Holzapfel (2000).

2.4.2 Nearly Incompressible Formulations

Nearly incompressible (isotropic) models are those whose stored energy can be split into two parts: W^{iso}, considering isochoric (or distortional or deviatoric) elastic response, and W^{vol}, accounting for volumetric (or dilational or spherical) elastic response. Thus, we have that

$$W(\tilde{I}_1, \tilde{I}_2, J) \equiv W^{iso}(\tilde{I}_1, \tilde{I}_2) + W^{vol}(J), \tag{2.32}$$

which uses the reduced invariants of Equation (2.17).

There is more than one way to define the volumetric term. One of them considers

$$W^{vol}(J) = \frac{1}{2}\kappa_0(J-1)^2, \tag{2.33}$$

for

$$\kappa_0 = \lambda_0 + \frac{2}{3}\mu_0 \tag{2.34}$$

being the bulk modulus. The terms λ_0 and μ_0 are the Lamé's parameters, related to Young's modulus, E_0, and the Poisson's ratio, ν_0, by

$$\lambda_0 = \frac{\nu_0 E_0}{(1+\nu_0)(1-2\nu_0)} \quad \text{and} \quad \mu_0 = G_0 = \frac{E_0}{2(1+\nu_0)}, \tag{2.35}$$

where μ_0 is the shear modulus for small deformations. Finally, according to Bonet & Wood (2008), the level of incompressibility can be approximated by setting

$$10^3\mu_0 \leqslant \kappa_0 \leqslant 10^4\mu_0. \tag{2.36}$$

2.4.3 Compressible Formulations

Some materials can experience certain measurable changes in volume. In the following, we present some compressible material models. Of particular interest to those forms including the Jacobian, J, which introduces some resistance to volume change in the strain energy functions.

In this context, except for the St. Venant-Kirchhoff law, one can argue that the compressible models below are, somehow, nearly incompressible. This

is true. What distinguishes them from those in the form of Section 2.4.2 is that the following material models are coupled. The term 'coupled' means W^{vol} is directly added to the strain energy function, and, in general, one is not able to define who is W^{iso}, since this is not written in terms of reduced invariants.

We also like to think the level of incompressibility does not necessarily follow Equation (2.36). Thus, these models express a simple form to avoid unrealistic behaviors, especially in large compressions.

2.4.3.1 St. Venant-Kirchhoff Model

The strain energy for the St. Venant-Kirchhoff (SVK) material model is

$$W^{SVK}(\boldsymbol{E}) = \frac{\lambda_0}{2}\,\mathrm{tr}^2(\boldsymbol{E}) + \mu_0\,\mathrm{tr}(\boldsymbol{E}^2). \tag{2.37}$$

With the help of Equations (2.11), (2.16a) and (2.16b), one is able to reformulate Equation (2.37) in terms of Cauchy-Green invariants:

$$W^{SVK}(I_1, I_2) = \frac{\lambda_0}{8}\,(I_1 - 3)^2 + \frac{\mu_0}{4}(I_1^2 - 2(I_1 + I_2) + 3). \tag{2.38}$$

The SVK law does not preserve volume under significant deformations. Furthermore, it fails to predict the material behavior under very large compressions (Klarbring & Strömberg, 2013, *i.a.*), which may be a crucial point in topology optimization analyses.

As a matter of fact, this model results in a linear stress-strain relation,

$$\boldsymbol{S} = \boldsymbol{\mathcal{D}} : \boldsymbol{E} \quad \text{or} \quad S_{IJ} = \mathcal{D}_{IJKL} E_{KL},$$

where : operator represents tensor contraction (by definition, $\boldsymbol{A} : \boldsymbol{B} = A_{ij}B_{ij} = \mathrm{tr}(\boldsymbol{A}^T\boldsymbol{B}) = \mathrm{tr}(\boldsymbol{A}\boldsymbol{B}^T)$), and is more suitable for small or large displacements, provided the strains are infinitesimal. In this sense, the SVK law can be properly rewritten as

$$W^{L}(\boldsymbol{\epsilon}) = \frac{\lambda_0}{2}\,\mathrm{tr}^2(\boldsymbol{\epsilon}) + \mu_0\,\mathrm{tr}(\boldsymbol{\epsilon}^2). \tag{2.39}$$

where ϵ is the infinitesimal strain tensor:

$$\boldsymbol{\epsilon} = \frac{1}{2}\left(\nabla_0 \boldsymbol{u} + \nabla_0 \boldsymbol{u}^T\right) \quad \text{or} \quad \epsilon_{IJ} = \frac{1}{2}\left(u_{I,J} + u_{J,I}\right). \tag{2.40}$$

2.4.3.2 Modified St. Venant-Kirchhoff Model

Among other attempts to address the issues linked to the SVK are their modified versions (mSVK). From those, we highlight Curnier's (Curnier, 1994)

strain energy function[5]:

$$W^{mSVK}(I_1, I_2, J) = \lambda_0 \left(J - \ln(J) - 1\right) + \frac{\mu_0}{4}(I_1^2 - 2(I_1 + I_2) + 3). \quad (2.41)$$

Notice that Equation (2.41) depends on J, and this model presents a certain level of compressibility. For curiosity, the parcel $J - \ln(J) - 1$ matches $W^{vol}(J) = \beta^{-2}(\beta \ln(J) + J^{-\beta} - 1)$ described by Ogden (1972), for $\beta = -1$.

2.4.3.3 Simo-Ciarlet Neo-Hookean Model

Despite the variations detached by Klarbring & Strömberg (2013), we will focus our attention on the version known as neo-Hookean of Simo-Ciarlet (nH-SC) (Simo & Pister, 1984; Ciarlet, 1988; Hashiguchi, 2020):

$$W^{nH\text{-}SC}(I_1, J) = \frac{\lambda_0}{4}(J^2 - 2\ln(J) - 1) + \frac{\mu_0}{2}(I_1 - 3 - 2\ln(J)). \quad (2.42)$$

Just like the SVK law, Equation (2.42) has an analytical solution for the out-of-plane strain component, C_{33}, required in plane stress investigations. Then, one does not have to iteratively solve a nonlinear equation to determine C_{33}, as explained below.

2.5 Two-dimensional Analysis

The computation of three-dimensional stresses and strains is straightforward. These quantities are evaluated by coupling the FE analysis (see Chapter 3) and the continuum mechanics theory discussed above. Considering the Lagrangian description of motion, one is only required to compute tensors $\boldsymbol{F}$, $\boldsymbol{C}$, and $\boldsymbol{S}$, respectively, from Equations (2.4), (2.9) and (2.24). The laborious task of deriving the strain energy function w.r.t. to strains is eliminated by either assuming a function already defined in literature or by using our `HyperSym` tool (Fontes *et al.*, to appear).

Yet, when dealing with two-dimensional approaches, things change. In this scenario, we have plane strain (PE) or plane stress (PS) approximations.

In plane strain, the deformations are constrained to the plane, which means the out-of-plane deformation components are null: $E_{13} = E_{23} = E_{31} = E_{32} = E_{33} = 0$. By Equation (2.11), we can link $\boldsymbol{E}$ to $\boldsymbol{C}$ to achieve

$$\boldsymbol{C}^{PE} = \begin{bmatrix} C_{11} & C_{12} & 0 \\ C_{21} & C_{22} & 0 \\ 0 & 0 & 1 \end{bmatrix}, \quad (2.43)$$

[5]To be fair, Curnier (1994) wrote down the stress-strain relation, from which one can go back and obtain W.

where the non-zero components are evaluated in the same manner as they are in three-dimensional analyses. Therefore, we can take advantage of two-dimensional FE implementations and manually add the third row and column to $\boldsymbol{C}^{PE}$ in Equation (2.43).

In plane stress, we are enforcing the out-of-plane true stress components to be null: $\sigma_{13} = \sigma_{23} = \sigma_{31} = \sigma_{32} = \sigma_{33} = 0$. One question arises: what are the values of C_{I3} and C_{3J}, for $I, J = 1, 2, 3$, that nullify the respective stresses?

To answer this question, we must take into account that:

(i) $\boldsymbol{C}$ is a symmetric tensor, and

(ii) we can relate $\boldsymbol{\sigma}$ to $\boldsymbol{S}$ from Equation (2.21).

Item (i) tells us the number of unknowns is reduced to C_{13}, C_{23} and C_{33}, while Item (ii) informs us we can look directly to $\boldsymbol{S}$, since nullifying σ_{ij} is equivalent to nullifying the correspondent S_{IJ}.

We observed that the shear stress components have the form of $S_{IJ} \equiv S_{IJ}(C_{IJ})$, for $I, J = 1, 2, 3$ and $I \neq J$. This means each shear stress is written only in terms of its deformation component. Therefore, we have $S_{I3} = 0$, for $I = 1, 2$, if and only if $E_{I3} = C_{I3} = 0$, and

$$\boldsymbol{C}^{PS} = \begin{bmatrix} C_{11} & C_{12} & 0 \\ C_{21} & C_{22} & 0 \\ 0 & 0 & C_{33} \end{bmatrix}. \tag{2.44}$$

$C_{33} \neq 0$ must be determined accordingly from the strain energy. Thanks to Equation (2.44), we are able to express $S_{33} \equiv S_{33}(C_{33})$, since all the in-plane deformations are known.

Table 2.1 shows the out-of-plane deformation value, C_{33}, for the models aborded in Section 2.4. We start by differentiating Equations (2.38) and (2.41) or (2.42) to obtain the PK2 stress. Then, we rewrite the result in terms of C_{33} and, finally, solve $S_{33} = 0$.

Model	PK2 stress, $\boldsymbol{S}$	Out-of-plane deformation, C_{33}
SVK	$\frac{\lambda_0}{2}\boldsymbol{I}(I_1 - 3) - \mu_0(\boldsymbol{I} - \boldsymbol{C})$	$\frac{2\mu_0 - \lambda_0(C_{11} + C_{22} - 3)}{2\mu_0 + \lambda_0}$
mSVK	$\lambda_0(J-1)\boldsymbol{C}^{-1} - \mu_0(\boldsymbol{I} - \boldsymbol{C}^{-1})$	$\frac{\lambda_0}{C_{33}}(\sqrt{C_{33}\mathcal{J}} - 1) = \mu_0(1 - C_{33})$
nH-SC	$\frac{\lambda_0}{2}(J^2 - 1)\boldsymbol{C}^{-1} + \mu_0(\boldsymbol{I} - \boldsymbol{C}^{-1})$	$\frac{2\mu_0 + \lambda_0}{2\mu_0 + \lambda_0\mathcal{J}}$

Note: $\mathcal{J} = C_{11}C_{22} - C_{12}^2$.

Table 2.1: Out-of-plane deformation, C_{33}, in plane stress state.

As can be seen, for the modified SVK model, mSVK, there is no analytical solution. To determine who C_{33} is, we resort to numerical methods. Here, we used Newton's method where, at the $(i+1)$-th iteration, the corresponding value is

$$C_{33}^{(i+1)} = C_{33}^{(i)} - r\left(\frac{dr}{dC_{33}}\right)^{-1}. \tag{2.45}$$

We assumed an initial guess, $C_{33}^{(0)} = \mathcal{J}^{-1}$ (*vid.* Table 2.1), which corresponds to the undeformed configuration where $J = 1$, and r is the expression obtained from nullifying S_{33}. For mSVK, we have

$$r = \frac{\lambda_0}{C_{33}}(\sqrt{C_{33}\mathcal{J}} - 1) - \mu_0(1 - C_{33}) \quad \text{and} \quad \frac{dr}{dC_{33}} = \mu_0 + \frac{\lambda_0}{C_{33}^2}\left(\sqrt{\frac{\mathcal{J}}{C_{33}}} - 1\right).$$

The iterative procedure ends when one of the following criteria is met:

$$\max\{|C_{33}^{(i+1)} - C_{33}^{(i)}|, |r|\} \leqslant 10^{-9},$$

or it takes 10 iterations.

3
A Brief Review to the Finite Element Method

> *"Come then, and let us pass a leisure hour in storytelling, and our story shall be the education of our heroes."*
>
> **Plato (428 b.C.–348 b.C.)**

This chapter will introduce the main concepts behind the finite element (FE) method used to approximate the solution of boundary-value problems. We focus on the application of FE in hyperelasticity and only consider the material description or the Total Lagrangian formulation, where the stress and strain quantities are taken at the initial (undeformed) geometry. For further details on FE basis, please refer to the textbooks of Bonet & Wood (2008), Bathe (2014), or Kim (2015).

3.1
The Finite Element Method Applied to Hyperelasticity

The design domain is divided into smaller pieces, the elements. For each piece, we associate the displacement of the e-th element by interpolating its n nodal coordinates. This is done through the relation

$$\boldsymbol{u}_e = \sum_{c=1}^{n} N^c(\xi_i)\boldsymbol{u}_e^c, \tag{3.1}$$

where N^c are the shape functions, given in terms of a fixed local coordinate system, ξ_i, for $i = 1$, 2 or 3, and $\boldsymbol{u}_e^c$ refers to displacements at node c.

For isoparametric formulations, *vid.* Bathe (2014), we know the geometry is interpolated similarly to the displacements, i.e.,

$$\boldsymbol{x}_e = \sum_{c=1}^{n} N^c(\xi_i)\boldsymbol{x}_e^c. \tag{3.2}$$

Then, substituting (3.1) into Equation (2.5), the deformation gradient is now expressed in terms of the local coordinate system as

$$\begin{aligned}\boldsymbol{F} &= \frac{\partial \boldsymbol{u}}{\partial \boldsymbol{X}} + \boldsymbol{I} \\ &= \frac{\partial \boldsymbol{u}}{\partial \boldsymbol{\xi}} \frac{\partial \boldsymbol{\xi}}{\partial \boldsymbol{X}} + \boldsymbol{I} \\ &= \sum_{c=1}^{n} \frac{\partial N^c(\xi_i)}{\partial \boldsymbol{\xi}} \boldsymbol{U}\boldsymbol{J}^{-1} + \boldsymbol{I} \quad \text{or} \\ F_{aA} &= \sum_{c=1}^{n} \frac{\partial N^c(\xi_i)}{\partial \xi_A} U_{ca} J_{aA}^{-1} + \delta_{aA},\end{aligned} \tag{3.3}$$

where $\boldsymbol{J}$ is the Jacobian operator (tensor) linking the natural coordinate derivatives (X_i, for i = 1,2, or, 3) to the local coordinate derivatives, ξ_i:

$$\frac{\partial}{\partial \boldsymbol{\xi}} = \boldsymbol{J} \frac{\partial}{\partial \boldsymbol{X}}, \quad \text{for} \quad \boldsymbol{J} = \begin{bmatrix} \dfrac{\partial X_1}{\partial \xi_1} & \dfrac{\partial X_2}{\partial \xi_1} & \dfrac{\partial X_3}{\partial \xi_1} \\ \dfrac{\partial X_1}{\partial \xi_2} & \dfrac{\partial X_2}{\partial \xi_2} & \dfrac{\partial X_3}{\partial \xi_2} \\ \dfrac{\partial X_1}{\partial \xi_3} & \dfrac{\partial X_2}{\partial \xi_3} & \dfrac{\partial X_3}{\partial \xi_3} \end{bmatrix}. \tag{3.4}$$

The weak form of a nonlinear elastic system may be derived using the principle of minimum potential energy, which is the difference between the work done by external forces, Π_{ext}, and the stored strain energy, Π_{int}. The work done by applied forces is calculated by multiplying displacement by the applied forces, assuming that external loads do not depend on deformation, i.e., they are conservative. The strain energy is typically computed by integrating the strain energy density functions over the initial geometry. In this sense, we have

$$\Pi = \Pi_{ext}(\boldsymbol{u}) - \Pi_{int}(\boldsymbol{u}) = \int_{{}^0\Omega} \boldsymbol{b}^T \boldsymbol{u} \, \mathrm{d}V + \int_{\partial {}^0\Omega} \boldsymbol{t}^T \boldsymbol{u} \, \mathrm{d}\Gamma - \int_{{}^0\Omega} W \, \mathrm{d}V, \tag{3.5}$$

where $\boldsymbol{b}$ is the body force (vector) acting on ${}^0\Omega$ and $\boldsymbol{t}$ is the surface traction vector at the boundary $\partial {}^0\Omega$.

To minimize Equation (3.5), we take its derivative w.r.t. to an infinitesimal displacement field, $\delta \boldsymbol{u}$. Then, we have

$$\frac{\partial \Pi}{\partial (\delta \boldsymbol{u})} = \frac{\partial}{\partial (\delta \boldsymbol{u})} \int_{{}^0\Omega} \boldsymbol{b}^T \delta \boldsymbol{u} \, \mathrm{d}V + \frac{\partial}{\partial (\delta \boldsymbol{u})} \int_{\partial {}^0\Omega} \boldsymbol{t}^T \delta \boldsymbol{u} \, \mathrm{d}\Gamma - \frac{\partial}{\partial (\delta \boldsymbol{u})} \int_{{}^0\Omega} W \, \mathrm{d}V = \boldsymbol{0},$$

which requires the Newton-Raphson iterative method through a sequence of linearizations. There are several incremental-iterative methods to solve nonlinear problems. In this dissertation, we selected the load control method, described in Section 3.1.1.

3.1.1 Incremental-Iterative Newton-Raphson Procedure

We want to find the displacement field, $\boldsymbol{u}$, such that the internal forces, $\boldsymbol{f}_{int}$, are in equilibrium with the external loads, $\boldsymbol{f}_{ext}$. So, we may define the residue or out-of-balance force as

$$\boldsymbol{r}(\boldsymbol{u}) = \boldsymbol{f}_{ext} - \boldsymbol{f}_{int}(\boldsymbol{u}) = \boldsymbol{0}. \tag{3.6}$$

In our analyses, the external force corresponds to applied loads with fixed direction and magnitude, while the internal force is defined in terms of the energy interpolation scheme (EIS). Section 6.2.2 explains how to deal with the EIS.

A typical approach is to split $\boldsymbol{f}_{ext}$ into smaller load steps, s. To each load step, we can define the load factor, $\Delta\lambda_s^{(i)}$ – which may be seen as a percentage of the applied load. As a consequence, we are interested in tackling incremental-iterative approaches in the form of

$$\boldsymbol{r}(\boldsymbol{u})_s^{(i)} = \Delta\lambda_s^{(i)}\boldsymbol{f}_{ext} - \boldsymbol{f}_{int}(\boldsymbol{u})_s^{(i)}, \tag{3.7}$$

where i represents the iterations required to solve Equation (3.7) for each load step.

The load factor and displacement vector at load step s take into account the contribution from the previously converged step, $s-1$, and its increment at the current iteration. Then,

$$\lambda_s = \lambda_{s-1} + \Delta\lambda_s, \quad \text{and} \tag{3.8}$$

$$\boldsymbol{u}_s = \boldsymbol{u}_{s-1} + \Delta\boldsymbol{u}_s \tag{3.9}$$

with

$$\Delta\boldsymbol{u}_s = \Delta\boldsymbol{u}_s^{(i-1)} + \Delta\boldsymbol{u}_s^{(i)} \tag{3.10}$$

and $\Delta\boldsymbol{u}_s^{(0)} = 0$.

The load control method (LCM) is a particular case of the Newton-Raphson technique that imposes a constant force constraint. Thus,

$$\Delta\lambda_s^{(i)} = \begin{cases} \overline{\Delta\lambda}_s, & \text{for } i = 1 \\ 0, & \text{otherwise,} \end{cases} \tag{3.11}$$

where $\overline{\Delta\lambda}_s$ is a prescribed load increment. Figure 3.1 schematics the LCM.

To find the incremental displacement, $\Delta\boldsymbol{u}_s^{(i)}$, the equilibrium path is locally linearized. Suppose the solution at the i-th iteration is known and is $\boldsymbol{u}_s^{(i)}$. The displacement at the $(i+1)$-th iteration can be approximated via the first-order Taylor series as

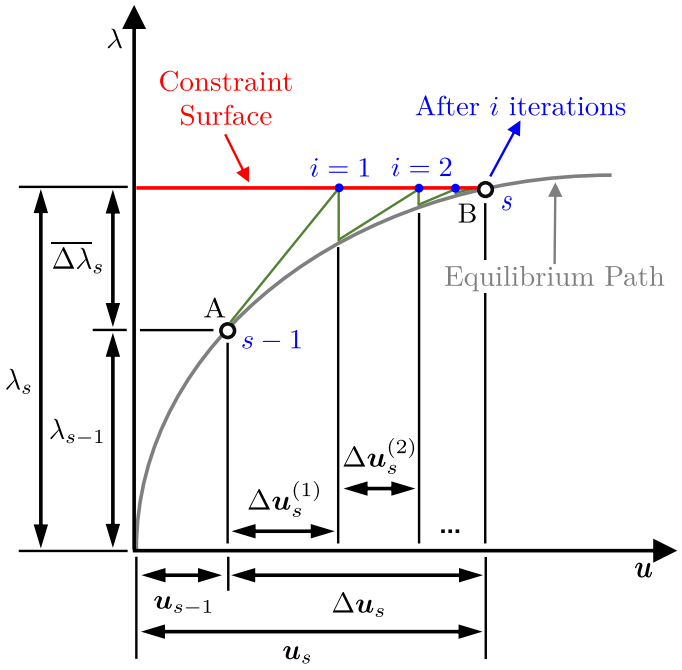

Figure 3.1: Load control method diagrammatic.

$$\begin{aligned} \boldsymbol{r}(\boldsymbol{u})_s^{(i+1)} &\approx \boldsymbol{r}(\boldsymbol{u})_s^{(i)} + \frac{\partial \boldsymbol{r}(\boldsymbol{u})_s^{(i)}}{\partial \boldsymbol{u}_s^{(i)}} \Delta \boldsymbol{u}_s^{(i)} \\ &\approx \boldsymbol{r}(\boldsymbol{u})_s^{(i)} - \underbrace{\frac{\partial \boldsymbol{f}_{int}(\boldsymbol{u})_s^{(i)}}{\partial \boldsymbol{u}_s^{(i)}}}_{\boldsymbol{K}_{T_s}^{(i)}} \Delta \boldsymbol{u}_s^{(i)} = \boldsymbol{0}, \end{aligned} \tag{3.12}$$

where: (i) we take advantage of $\boldsymbol{f}_{ext}$ being deformation-independent, and (ii) $\boldsymbol{f}_{ext} \approx \boldsymbol{f}_{int}$ at the equilibrium. Rearranging Equation (3.12) yields in

$$\boldsymbol{K}_{T_s}^{(i)} \Delta \boldsymbol{u}_s^{(i)} = \boldsymbol{r}(\boldsymbol{u})_s^{(i)}. \tag{3.13}$$

Similarly to the internal force vector, the EIS also affects the expression for the tangent stiffness matrix, $\boldsymbol{K}_T$ (*vid.* Section 6.2.2).

The LCM fails to determine equilibrium paths in the vicinity of (load) limit points, where the stiffness matrix becomes singular and the iterative updated displacement vector, $\Delta \boldsymbol{u}_s^{(i)}$, tends to be unbounded. But this limitation had no effect on our simulations since we observed that they did not involve any type of limit points. Those interested in tracing more intricate equilibrium paths can consult Leon *et al.* (2011).

3.1.2 Finite Element Verification

To verify our FE implementations, we consider two examples. First we solve a simple block under homogenous uniaxial deformation. This allows us to

compare our FE routine with analytical stress solutions for each of the material models of Chapter 2. Sadly, this example can only be applied to PE or three-dimensional cases, because the PS lacks analytical expression for the stress distribution. Alternatively, one can construct functions to incorporate these models in commercial softwares, but, as this is not an easy undertaking, we will leave it for future works.

Afterward, we run another similar example to verify our code in the PS state using Mooney-Rivlin material (Mooney, 1940; Rivlin, 1948). This makes it simple for us to check our routine with commercial softwares – here, ANSYS®. Then, we can ensure that the evaluation of the LCM and the stress computation are done accurately.

3.1.2.1 Block Under Homogeneous Uniaxial Deformation

Examine the block of Figure 3.2. In this scenario, we assume a single element, where all degrees of freedom are prescribed, but only the horizontal displacements of nodes 2 and 3 on the right face are nonzero.

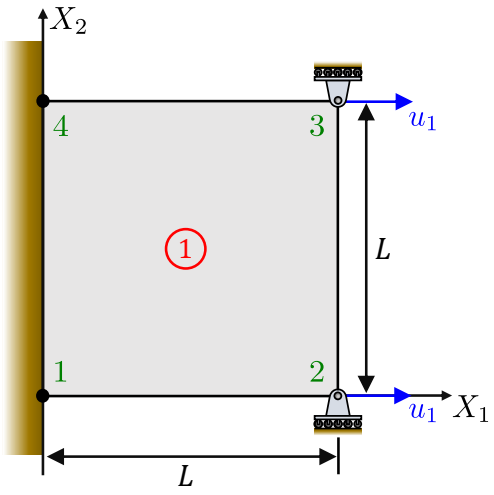

Prescribed Disp. & Geometry:
$u_1 = 1$
$L = 1$
$t = 1$

Material Properties:
$E_0 = 1,000$
$\nu_0 = 0.3$

Data for LCM:
Step factor, $\overline{\Delta\lambda}_s = 0.1$
Max. iter. per step = 50

Figure 3.2: Block under homogeneous uniaxial deformation.

The homogeneous uniaxial deformation is described by (Klarbring & Strömberg, 2013)

$$x_1 = \Lambda X_1, \quad x_2 = X_2, \quad \text{and} \quad x_3 = X_3,$$

where X_i and x_i are the material and spatial coordinates, respectively, and Λ is the stretch in direction 1.

In this particular case, the final configuration of the block is easily verified; for the prescribed displacement of $u_1 = 1$, the maximum expected

stretch in that direction is $\Lambda = 2$. So, we can define, in the PE state, that

$$F_{iI} = \begin{bmatrix} \Lambda & 0 & 0 \\ 0 & 1 & 0 \\ 0 & 0 & 1 \end{bmatrix}, \quad C_{IJ} = F_{Ii}F_{iJ} = \begin{bmatrix} \Lambda^2 & 0 & 0 \\ 0 & 1 & 0 \\ 0 & 0 & 1 \end{bmatrix}, \quad \text{and} \quad J = \det(F_{iI}) = \Lambda.$$

From the hyperelasticity theory (*vid.* Chapter 2) the PK2 stress, $\boldsymbol{S}$, can be derived from Equation (2.25) or Equation (2.28), whereas the Cauchy stress, $\boldsymbol{\sigma}$, is acquired by the push-forward operation in Equation (2.21). So, for the material models of Section 2.4.3, the expressions for $\sigma_{11}(\Lambda, \lambda_0, \mu_0)$ – analytically calculated – are shown in Table 3.1 in terms of Lamé's parameters (λ_0 and μ_0).

Model	$\sigma_{11}(\Lambda, \lambda_0, \mu_0)$
SVK	$\frac{\Lambda\lambda_0}{2}(\Lambda^2 - 1) + \Lambda\mu_0(\Lambda^2 - 1)$
mSVK	$\frac{\lambda_0}{\Lambda}(\Lambda - 1) + \Lambda\mu_0(\Lambda^2 - 1)$
nH-SC	$\frac{\lambda_0}{2\Lambda}(\Lambda^2 - 1) + \frac{\mu_0}{\Lambda}(\Lambda^2 - 1)$

Table 3.1: σ_{11} component of SVK, mSVK and nH-SC models under homogeneous uniaxial deformation.

We compare the analytical and numerical Cauchy stress responses of this block as it stretches. Figure 3.3 details this comparison, where the highlighted region represents the area where the materials perform similarly.

For all the investigated models, one can observe that not only did the final deformation reach the expected value, but also the Cauchy stresses coincide with the analytical responses. The analytical solution was also plotted in the range $0.2 \leqslant \Lambda \leqslant 2$, which corresponds to both the block's compression and tension – as compression and tension are different problems, for conciseness, we opt to plot the numerical solution only for the latter.

Figure 3.3 also reveals that the SVK model changes the slope sign at $\Lambda = \sqrt{3}/3$ – the minimum point of σ_{11}, where $\partial\sigma_{11}/\partial\Lambda = 0$, and $\partial^2\sigma_{11}/\partial\Lambda^2 > 0$. This variation during compression indicates a sudden change in the deformation direction, which is clearly incompatible with the physical behavior and explains why the SVK model is deprecated in applications involving large compressions. The other models are designed to overcome this limitation, which can be seen when $\sigma_{11} \to -\infty$ as $\Lambda \to 0$.

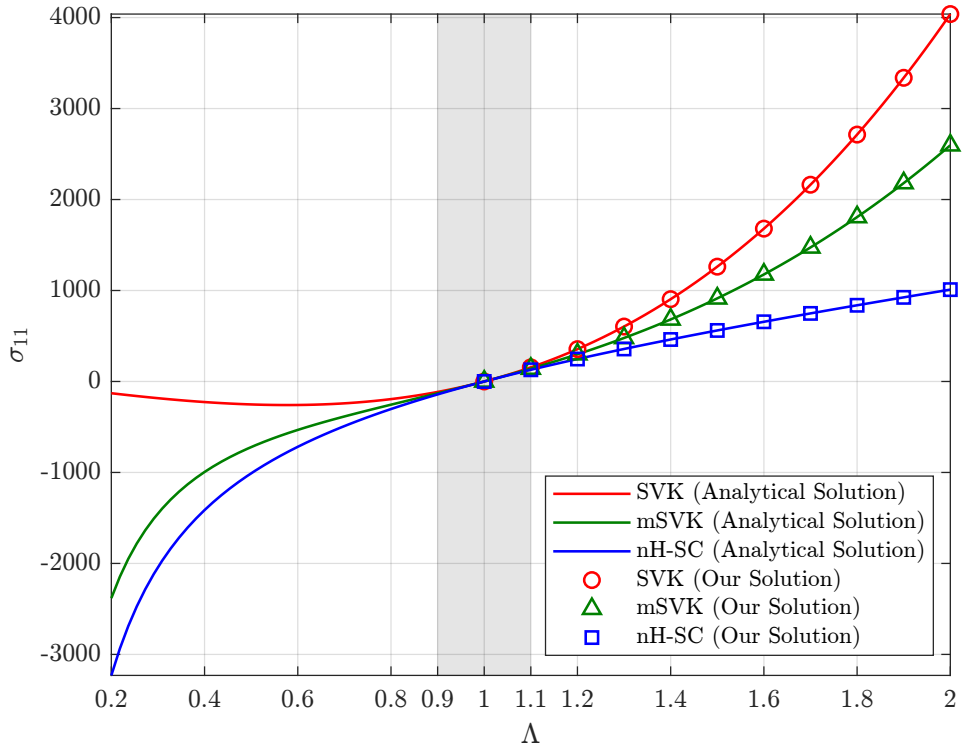

Figure 3.3: Cauchy stress vs. stretch for the homogeneous uniaxial deformation.

3.1.2.2 Block Under Uniaxial Deformation

As illustrated in Figure 3.4, the example of this section is somewhat similar to the one of Section 3.1.2.1, except that node 3 is now allowed to move in both in-plane directions. Additionally, we modify the dimensions and material properties to make it consistent with the analysis conducted by Kim (2015).

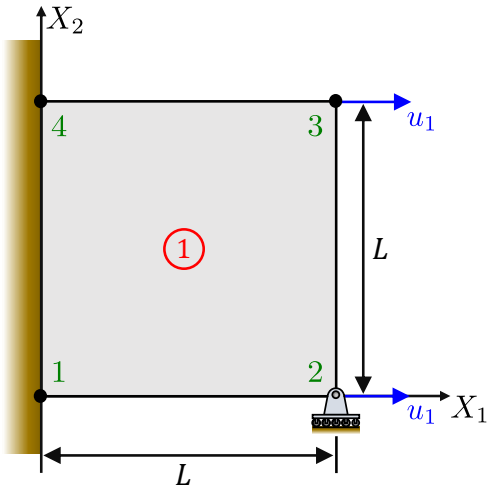

Prescribed Disp. & Geometry:
$u_1 = 200$
$L = 100$
$t = 1$

Material Properties:
$E_0 = 7,100$
$\nu_0 = 0.3$

Data for LCM:
Step factor, $\overline{\Delta\lambda}_s = 0.1$
Max. iter. per step = 50

Figure 3.4: Block under uniaxial deformation.

Particularly, here, we employ the Mooey-Rivlin (MR) material model, which is characterized by

$$W^{MR}(\tilde{I}_1, \tilde{I}_2) = A_{10}(\tilde{I}_1 - 3) + A_{01}(\tilde{I}_2 - 3) + \frac{\kappa_0}{2}(J-1)^2, \tag{3.14}$$

where $\tilde{I}_i$, for $i = 1, 2$, are the reduced stress invariants defined in Section 2.2.1. The parameters A_{mn}, for $m, n = 0, 1$, are material constants estimated in terms of the shear modulus, μ_0, as

$$A_{10} = 0.4\mu_0 \quad \text{and} \quad A_{01} = 0.1\mu_0,$$

and the bulk modulus, κ_0, is defined by Equation (2.34).

To verify our PS implementation, we track the von Mises stress at the element's centroid during deformation. Plotting this result in Figure 3.5, we observe a good agreement between stresses computed through our nonlinear FE routine and the one provided by ANSYS®.

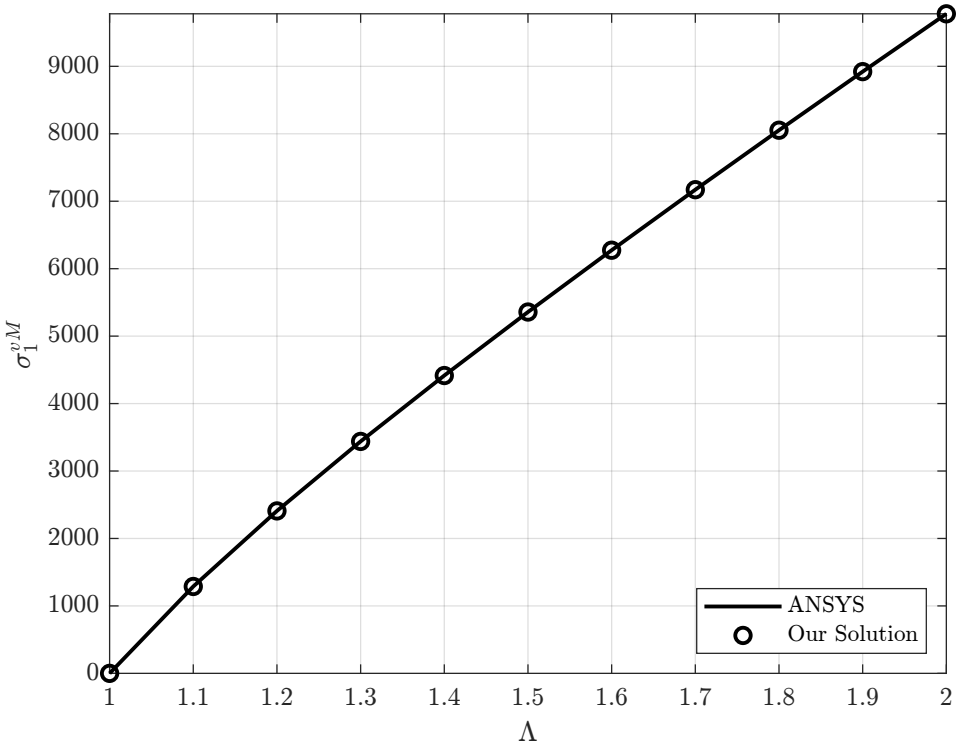

Figure 3.5: von Mises stress vs. stretch for a simple uniaxial deformation.

4
Topology Optimization

> *"Be like water making its way through cracks. Do not be assertive, but adjust to the object, and you shall find a way around or through it. If nothing within you stays rigid, outward things will disclose themselves (...) Now, water can flow or it can crash. Be water, my friend."*
>
> **Lee, B. (Lǐ XiǎoLóng) (1940–1973)**

The topology optimization method is used in structural optimization to achieve the most efficient material layout within a given design space under a given set of loads and boundary conditions. The goal is to improve structural performance by maximizing stiffness or natural frequencies, minimizing weight, and so on, while restricting the amount of allowable material, maximum displacement, stress limits, or manufacturing constraints, among others. This chapter will cover the techniques required by the classic density-driven approach.

4.1
Density-driven Topology Optimization Procedures

The material distribution can be modeled by different topology optimization strategies. For instance:

- homogenization method (Bendsøe & Kikuchi, 1988), which introduces composite micro-structures into the design space;
- density-driven approaches, which parameterize a continuous set of design variables through a density interpolation function. SIMP (see Section 4.1.3) and RAMP (Stolpe & Svanberg, 2001) are two examples;
- hard-kill or discrete methods, including ESO (Xie & Steven, 1993) and BESO (Huang & Xie, 2007), which directly handle discrete variables, and the material removal and/or addition are controlled by heuristic criterion defined in terms of the sensitivity number;
- boundary variation methods (Sethian & Wiegmann, 2000; Wang *et al.*, 2003), where the surfaces boundaries are implicitly represented by scalar level set functions;

- geometric component approaches, like moving morphable components (or bars) (Guo *et al.*, 2014).

Interested readers are directed to Sigmund & Maute (2013), Deaton & Grandhi (2014) and Wang *et al.* (2021) for additional information on the aforementioned methods.

A typical approach, by computational means, – and the one used in this dissertation – is to divide the design domain into small elements. In density-driven methods, to each design variable is associated a density[6] interpolation function, which is then attributed to the elements. Commonly, this function is constant within elements, so the design variable assumes the value given by this function: zero for void elements and one for solid (or structural) ones.

The discrete nature of the problem, though, makes it computationally impracticable, especially when a large number of design variables are involved (Sigmund, 2011, apud Wang et al., 2021). Then, the design variables are relaxed in order to employ gradient-based optimizers, like the Method of Moving Asymptotes, MMA, (Svanberg, 1987, 2002). This means the original binary formulation is transformed into a continuous problem, where the design variables are now spanning the range (0, 1].

4.1.1 Regularization Techniques

In general, the introduction of more holes within the design domain, without changing the structural volume, will increase the efficiency of a given structure. Bendsøe & Sigmund (2003) point out that in the limit of this process, it is possible to obtain microstructural variations that improve the use of the material.

In this sense, regularization methods are employed to reduce the space of admissible designs by some sort of global or local restriction on the variation of design variables, thus difficulting the formation of fine bars. Different methods are at our disposal. Some of them are: perimeter control (Haber *et al.*, 1996), which imposes an additional constraint on the optimization problem and globally controls the number of admissible holes in the domain; local gradient constraint (Petersson & Sigmund, 1998), which introduces a restriction in the design variables derivatives; and filtering schemes, which act similarly to convolutions and are recognized to avoid the well-known checkerboard-like

[6]In the context of this dissertation, density is not the ratio of mass to volume. Over the years, though, this name has been the most widely accepted interpretation for the design variables in topology optimization formulations (Bendsøe & Sigmund, 2003).

pattern[7]. Two of the most used filtering schemes are the sensitivity and design variable filters.

4.1.1.1 Linear Filtering Schemes

The sensitivity filter (Sigmund, 1994; Bendsøe & Sigmund, 2003) modifies the design variable derivatives in a heuristic way. It requires no extra constraint, thus reducing its CPU cost in comparison to other methods. However, since these derivatives are not consistent with the problem formulation, it is hard to establish the optimization problem being solved.

Similarly to the sensitivity filter, the design variable filter (Bruns & Tortorelli, 2001; Bourdin, 2001) appears as an alternative. Also known as the density filter, it allows local control on material distribution and ensures a smooth transition in the density field.

This scheme modifies the e-th design variable, z_e, based on a weighted average of the element densities on a fixed neighborhood. For the discrete case and the design variable located in the centroid of e-th element, $\bar{z}_e$, the filter can be defined as

$$\begin{aligned} \boldsymbol{\rho} = \boldsymbol{M}\boldsymbol{z} \text{ or } \rho_e = M_{ei} z_i, \quad \text{with} \\ M_{ei} = \frac{w_i\left(\overline{z}_e, \overline{z}_i\right)}{\sum\limits_{i \in N_e} w_i\left(\overline{z}_e, \overline{z}_i\right)}, \end{aligned} \tag{4.1}$$

where z_i is the initial design variable, ρ_e is the density of the e-th element, and N_e is the number of elements in the design domain.

The weight distribution function, w_i, for polynomial-like functions, is

$$w_i\left(\overline{z}_e, \overline{z}_i\right) = \max\left\{\left(1 - \frac{d_i}{r_{min}}\right)^s,\ 0\right\}, \tag{4.2}$$

where $d_i = ||\overline{z}_e - \overline{z}_i||$ is the distance between the centroids of elements e and i. The parameters r_{min} and s are the filter radius and the filter exponent, respectively.

When $s = 1$, the density filter represents a linear hat kernel since the weight distributions decays linearly with the distance from element e: it has magnitude 1 at element centroid to 0 at r_{min} – giving it the shape of a birthday party hat as in Figure 4.1. Other weight function kernels can be used, such as Green (Lazarov & Sigmund, 2011) or Gaussian (Lazarov *et al.*, 2016).

[7]That is the name given to the pattern of alternating solid and void material in a checkerboard-like fashion. The origin of this phenomenon is related to features of the FE approximations that maximize the strain energy (Diaz & Sigmund, 1995), and result in a layout with overestimated, artificially high stiffness.

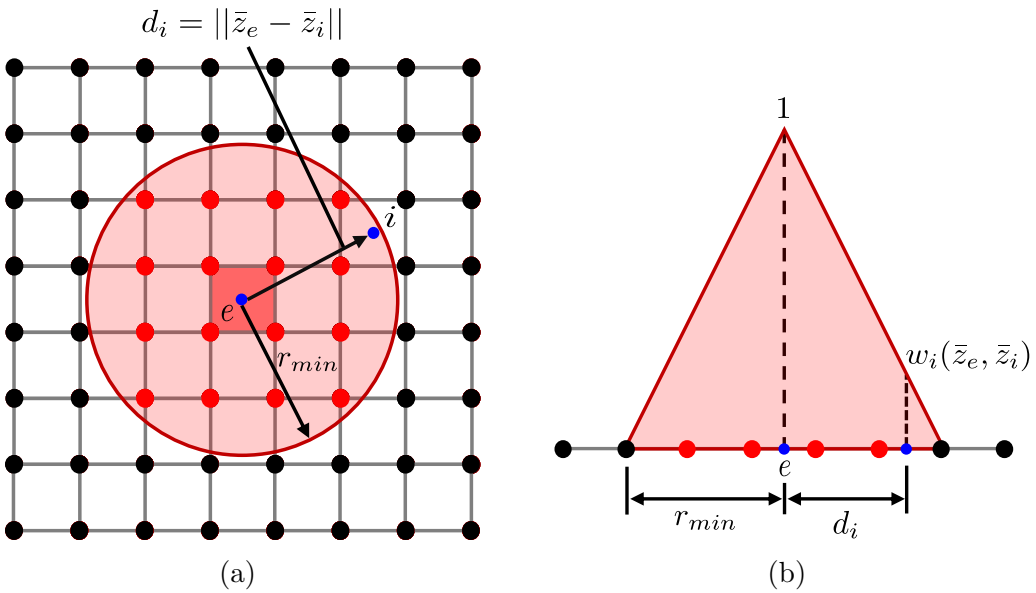

Figure 4.1: Two-dimensional linear density filter: (a) application in a regular quadrilateral element mesh and (b) its conical form.

One drawback of the linear filter has been the transition between solids and quasi-voids in the boundaries of optimized topologies. However, these intermediate densities can be alleviated using nonlinear projection functions or removing the filter effect – by gradually decreasing the value of r_{min} – as the optimization procedure converges.

4.1.2 Nonlinear Projection Functions

As stated by Guest *et al.* (2004), linear filters are inevitably submitted to the fading effect that occurs along the edges of structural members. Thus, nonlinear projection functions can be incorporated into topology optimization procedures to reduce the gray spectrum on the boundaries of structural members. Here, we will discuss two of them: the nonlinear filter scheme and the tanh projection function.

4.1.2.1 Nonlinear Filtering Scheme

Nonlinear filter schemes are also described by Equation (4.1). The exponent $s > 1$ should be employed to establish a nonlinear relation between design variables before and after the filtering process, *vid.* Figure 4.2.

Figure 4.3 illustrates the nonlinear filter scheme acting on the quasi-void to solid transition to simulate a possible design boundary obtained via topology optimization. We search for solutions that resemble Figure 4.3(a),

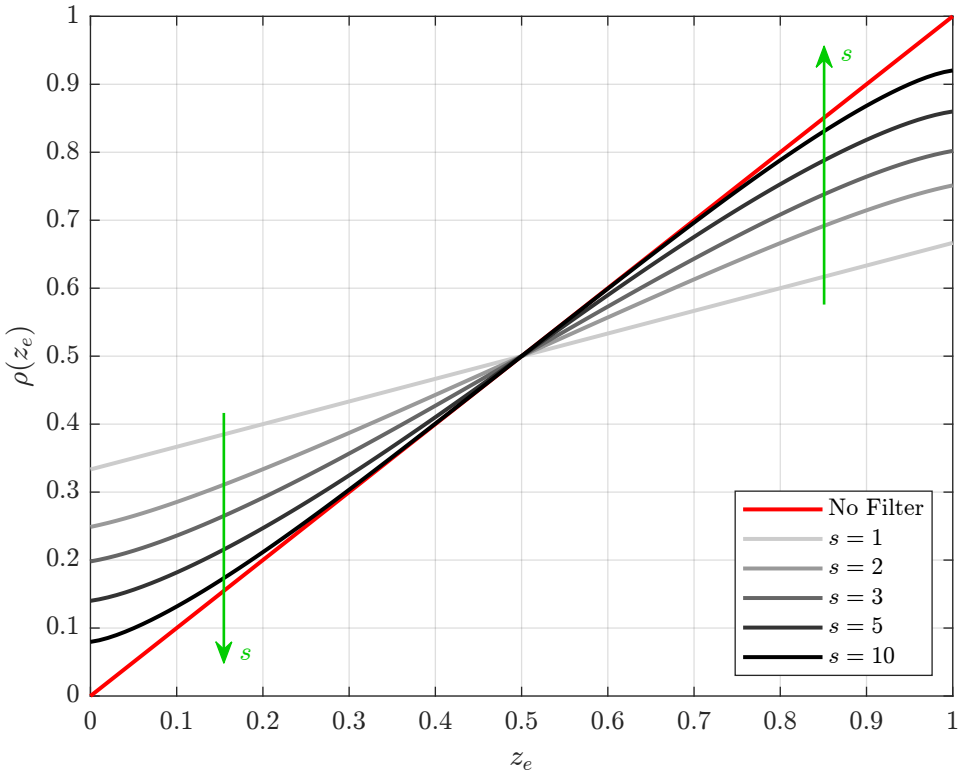

Figure 4.2: Relation between design variables before and after the filtering scheme. The arrows indicate the direction in which the exponent s grows.

thus, assuming the linear filter yields a solution in the form of Figure 4.3(b), with a thicker layer of grays between the quasi-void and solid phases.

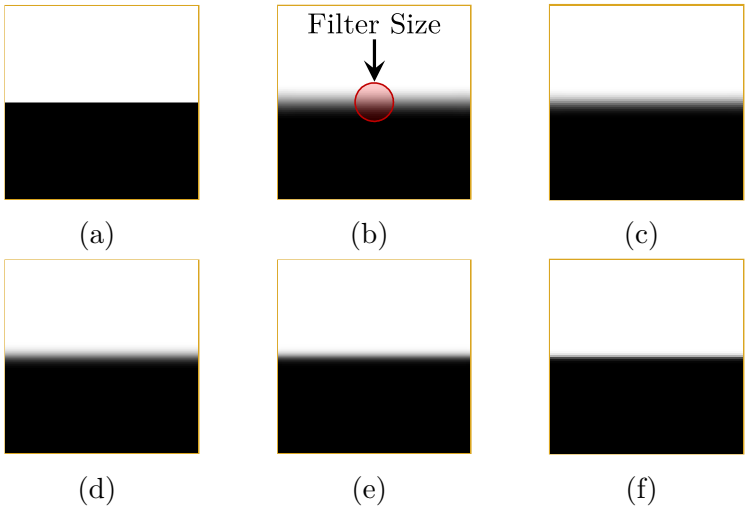

Figure 4.3: Effect of polynomial exponent in the nonlinear filtering scheme: (a) no filter, (b) $s = 1$ (linear filter), (c) $s = 2$, (d) $s = 3$ and (e) $s = 5$, (f) $s = 10$.

Increasing the filter exponent, s, introduces a nonlinear relation, culminating in the reduction of the grayish layer, as seen in Figures 4.3(c), 4.3(d), 4.3(e) and 4.3(f). Unfortunately, when increasing this exponent, the optimiza-

tion solution may degenerate, and, in general, it is easier to find adequate solutions for smaller values of s.

4.1.2.2 Hyperbolic Tangent Projection Function

A nonlinear Heaviside-based projection function was studied by Wang *et al.* (2011),

$$\tilde{\rho}_e(\beta, \eta, \rho_e) = \frac{\tanh(\beta\eta) + \tanh(\beta(\rho_e - \eta))}{\tanh(\beta\eta) + \tanh(\beta(1 - \eta))}, \tag{4.3}$$

where, typically, $\eta = 0.5$ and β is responsible for the sharpness of the projection.

Then, (i) $\beta = 1$ induces a linear relation between ρ_e and $\tilde{\rho}_e$, and (ii) the higher β, the closer this projection is to the Heaviside function. Other projections are available in the literature, e.g., the popular exponential projection function of Guest *et al.* (2004).

4.1.3 Material Representation

The intermediate values (grayish zones) introduced within the design domain by the continuous formulation, in general, have no physical meaning, whereas we seek for modeling isotropic materials (Bendsøe, 1989). Therefore, the design variables must be penalized to recover the discrete nature of the problem.

A widespread technique in topology optimization applications is the Solid Isotropic Material with Penalization, SIMP, (Bendsøe, 1989; Zhou & Rozvany, 1991). Its equation can be expressed in many forms. One of them is

$$\eta_E(\tilde{\rho}_e) = \check{\rho}_e = \epsilon + (1 - \epsilon)\tilde{\rho}_e(\boldsymbol{z})^p, \quad \text{for } p \geqslant 1, f \tag{4.4}$$

in which ϵ is a small positive number to ensure non-singularity of the stiffness matrix when $\tilde{\rho}_e \to 0$. Sigmund (2022) discourages values higher than 10^{-6}, hence we assume $\epsilon = 10^{-8}$, unless stated otherwise. The power, p, is a penalty term that steers the solution to a black and white configuration, and its maximum magnitude is usually restricted to the set $p \in [3, 5]$. Higher values of p will approximate the discrete formulation and can bring back the difficulties associated with it.

The density interpolation function of Equation (4.4) can be viewed as a simple parameter modification, which must be properly associated to material properties. This can be done by means of the elasticity tensor of the solid material, $\boldsymbol{\mathcal{D}}^0$:

$$\boldsymbol{\mathcal{D}} = \eta_E(\tilde{\rho}_e(\rho_e(\boldsymbol{z})))\boldsymbol{\mathcal{D}}^0. \tag{4.5}$$

5
Stress Formulations in Topology Optimization

"The only real mistake is the one from which we learn nothing."

Ford, H. (1863–1947)

In the past decades, the classical topology optimization problem, the minimization of compliance subject to material (or volume) constraints, went through a maturation process. Questions about the existence/uniqueness of solutions and key discussions involving mesh-dependence and checkerboards are no longer at the center of the debate.

When dealing with global measures, such as compliance, strength is usually not taken into account in the optimization problem. Recalling its importance in practical designs, one may be asking the reason(s) for that. This chapter will explore some features of stress-constrained topology optimization.

5.1
Difficulties of Stresses Constraints

The stress-constrained topology optimization has four major issues: (i) the 'singularity' or singular optimum phenomenon, (ii) the local nature of stress, also known as a large-scale problem, (iii) the nonlinear stress behavior due to material redistribution, and (iv) the accuracy of stress assessments.

We conducted a comprehensive review on the first two topics in Appendix A. Consequently, in this chapter, we only address the techniques we judged most pertinent to the rest of this dissertation.

5.1.1
Singular Optimum

The singular optimum was first reported by Sved & Ginos (1968). They studied the optimum solution of a three-bar truss subjected to stress constraints and concluded that all bars must remain in the final structure. But they also observed that if one of the bars were eliminated – so that the solution remains statically determined – the volume of the truss could be reduced even further. This happens because none of the bars can be eliminated from the optimum solution without violating the stress constraints.

This phenomenon is associated with the degeneration or irregularity in the space of admissible solutions formed thanks to discontinuities at quasi-void zones (Cheng & Jiang, 1992). As a consequence, the true optimal is not found in the initial feasible region[8], and the optimization algorithms (based on first-order conditions) converge to a value that does not meet the Karush-Kuhn-Tucker conditions (KKT) conditions (Kirsch, 1989, 1990). The reader interested in this theme can consult Rozvany (2001), who presented an extensive review on the scope of truss optimization.

5.1.1.1 *Traditional Vanishing Constraints*

In density-driven topology optimization approaches, stresses are design-variable-dependent. When the optimization algorithms try to remove material from the design domain, the stresses will assume a finite value – in order to not violate the constraints –, and material will not be removed from the design domain, as it is necessary to resist the high stresses acting there.

One possible way to solve this issue is to replace the stress constraints with "some well-behaved constraints", as detached by Cheng & Jiang (1992). Following this approach, the stress constraints[9] are rewritten in the form of

$$g_j(\boldsymbol{z}) = \tilde{\rho}_j(\boldsymbol{z}) \left(\frac{\sigma_j^{vM}(\boldsymbol{z})}{\sigma_{lim}} - 1 \right) \leqslant 0, \quad \text{for } j = 1, 2, \ldots, N_c, \tag{5.1}$$

where N_c is the number of constraints.

As the stresses are physically not defined at low-stiffness zones, stress-constrained optimization problems belong to a class termed mathematical programs with vanishing constraints, MPVC, (Achtziger & Kanzow, 2008) and Equation (5.1) is known as *traditional vanishing constraint* (TVC).

5.1.1.2 *Polynomial Vanishing Constraints*

Giraldo-Londoño & Paulino (2020) introduced a new stress constraint, named *polynomial vanishing constraint* (PVC):

$$g_j(\boldsymbol{z}) = \eta_E(\tilde{\rho}_j)\Lambda_j \left(\Lambda_j^2 + 1 \right) \leqslant 0, \quad \text{for } j = 1, 2, \ldots, N_c, \tag{5.2}$$

[8] A feasible region is the set of constraints that satisfies a certain optimization problem. It is also known by the names of feasible set or search space. In any case, we expand this last term so it refers to the set in which the solver searches for the solution.

[9] In the original formulation, the design variables were not projected. Therefore, instead of $\tilde{\rho}_j$, the constraints were functions of ρ_j. This is still the case if one uses solely density-driven methods without projections.

with

$$\Lambda_j = \frac{\sigma_j^{vM}(\boldsymbol{z})}{\sigma_{lim}} - 1,$$

and η_E is the material interpolation function displayed in Equation (4.4).

This constraint is a modified version of TVC, which has the main benefit that when $\sigma_j^{vM}(\boldsymbol{z})/\sigma_{lim} \gg 1$ the term $\Lambda_j^3 = \left(\sigma_j^{vM}(\boldsymbol{z})/\sigma_{lim} - 1\right)^3$ is dominant, and $\sigma_j^{vM}(\boldsymbol{z})$ is highly violated. More details about the PVC can be found in Giraldo-Londoño & Paulino (2021).

5.1.2 Large Number of Constraints

Stresses are local quantities that, theoretically, should be measured at each point of a body $\mathcal{B}$. As this is not possible, each stress value is directly computed on the element using the FE method. We opt to evaluate the stresses in the element centroid[10]. In this sense, a mesh of N_e elements will have $N_c = N_e$ constraints.

In general, the mesh is refined to get high-resolution results with sufficient details to represent the model. Gradient-based solvers are widely employed in optimization; nonetheless, these solvers require information from the derivatives of both the objective and constraints. Particularly, the sensitivity analysis is directly affected by the number of stress constraints, since one must derive them at each evaluation point and for each variable. Consequently, the optimization procedure becomes complex, and the optimization involving stress constraints is called a large-scale problem.

An alternative is to convert the stress constraints into global quantities in an attempt to approximate the local properties of stresses. This can be accomplished by utilizing one or more regionalization approaches and aggregated measures – see Appendix A for more details. Another possibility is tackling unconstrained optimization formulations through the Augmented Lagrangian method, in which the stresses are assessed locally and penalized according to the level of infeasibility. We detail this approach in Section 5.2.

[10]Stresses can be evaluated in: (i) the element centroid, (ii) the Gauss' (integration) point, or (iii) the nodes. This choice varies from one to another and is also influenced by the applied integration method. Of course, if one opts for options (ii) and (iii), the number of constraints tends to increase significantly. For example, in the bilinear isoparametric element, while option (i) presents one constraint per element, options (ii) and (iii) will have four constraints if the full integration method is used.

5.1.3
Nonlinear Response of Stresses

The stress field is directly affected by changes in the material distribution, which is especially pronounced in critical points, such as sharp and re-entrant corners, or any other location with a large spatial gradient. In the scope of density-driven topology optimization, this means the stress at a point j is affected not only by the changes in the density but also by those in the nearby points. This effect is known as the nonlinear response (or behavior) of stresses.

The optimization process and its methods must be capable of dealing with this behavior; otherwise, the algorithm may fail to converge because large gradient points will dictate the process. Le *et al.* (2010) found that density filters (*vid.* Section 4.1.1.1) can assist with this. After filtering, we end up with a regularized mesh and, thus, a uniform stress distribution.

5.1.4
Accuracy of Stress Assessments

The inaccuracy in the evaluation of the stress field is related to the jagged nature of the optimized design that originated from the FE discretization. These jagged contours create artificially high-stress levels at the optimized structure's boundaries. Even though these artificial stresses do not affect the stress assessments in the structure's interior, they will, undoubtedly, culminate in heavier designs, since more material is required in the design domain to compensate for these artificial values.

According to Svärd (2015), one may increase the quality of stress by extrapolating the design's internal values to its boundaries. Some efforts couple shape and topology optimization to create more 'finished' products (Nguyen & Kim, 2020; Dev *et al.*, 2022; Stankiewicz *et al.*, 2022). Nonetheless, we understand that: (i) the presence of grayish intermediate densities can alleviate these artificial stresses, and (ii) this issue is not easy to solve and perhaps is better treated during post-processing stages.

5.2
Solution via Local Stresses

As discussed in Section 5.1.2, stresses are local quantities. Instead of approximating stress levels with a global measure through aggregation techniques, one can directly compute their local value. This is achieved using penalty methods, in which the main idea (Bertsekas, 1999) is to eliminate some or all of the constraints by adding to the objective function a penalty term, Φ. To this term is attributed a high cost for the unfeasible points.

One of these penalty methods is the Augmented Lagrangian method (ALM) (Hestenes, 1969). We first discuss the ALM for equality constraints and next, extend it to inequality-constrained problems.

This dissertation just provides the foundation for understanding how the ALM is applied to stress-constrained optimization problems. To interested readers, we recommend the books of Bertsekas (1999) and Nocedal & Wright (2006), and the references therein. We also detach the book of Birgin & Martínez (2014, chapter 4), where one can study an ALM variation with shifted constraints.

5.2.1
Augmented Lagrangian Method in Equality-Constrained Problems

Consider the general optimization problem with n equality constraints, $h_j(\boldsymbol{x})$,

$$\begin{aligned} \min_{\boldsymbol{x}} \quad & f(\boldsymbol{x}) \\ \text{s.t.:} \quad & h_j(\boldsymbol{x}) = 0, \quad \text{for } j = 1, 2, \ldots, n, \end{aligned} \tag{5.3}$$

where $f\colon \mathbb{R}^n \mapsto \mathbb{R}$, $h\colon \mathbb{R}^n \mapsto \mathbb{R}^m$, for $m \leqslant n$. Its unconstrained penalized variant may be stated in terms of the augmented Lagrangian function. Then, the optimization problem becomes

$$\min_{\boldsymbol{x}} \quad \mathcal{L}_A(\boldsymbol{x}, \boldsymbol{\lambda}, \varphi) = \underbrace{f(\boldsymbol{x}) + \sum_{j=1}^{n} \lambda_j h_j(\boldsymbol{x})}_{\text{Lagrangian method, } \mathcal{L}(\boldsymbol{x})} + \underbrace{\sum_{j=1}^{n} \frac{\varphi}{2} h_j^2(\boldsymbol{x})}_{\text{Penalty term, } \Phi(\boldsymbol{x})}, \tag{5.4}$$

for φ being a positive penalty parameter. The solution of the Subproblem (5.4), $\boldsymbol{x}$, converges to the solution of Problem (5.3), $\boldsymbol{x}^\star$, provided that certain regularity conditions are met (see Bertsekas (1999) and Nocedal & Wright (2006) for further details).

The Subproblem (5.4) is similar to the Lagrangian method, in which the original problem is transformed into an unconstrained version with the inclusion of Lagrange multipliers associated with equality constraints, λ_j. In this sense, the addition of the penalty term explains this method's name: augmented Lagrangian.

As mentioned by Nocedal & Wright (2006), the use of Lagrange multipliers also reduces the possibility of ill-conditioning. Historically, though, this benefit was not known in the early days, and problems in the form of Equation (5.3) were solved by minimizing f plus a quadratic penalty term, Φ. This is called the exterior penalty method (EPM) or method of penalty functions,

$$\min_{\boldsymbol{x}} \quad \mathcal{Q}(\boldsymbol{x}, \varphi) = f(\boldsymbol{x}) + \sum_{j=1}^{n} \frac{\varphi}{2} h_j^2(\boldsymbol{x}),$$

and explains why the ALM is also labeled as a penalty method.

Back to Problem (5.3), it relies on iteratively solving the Subproblem (5.4). the first-order optimality criterion requires that for the i-th iteration,

$$\nabla_{\boldsymbol{x}} \mathcal{L}_A^{(i)}(\boldsymbol{x}, \boldsymbol{\lambda}^{(i)}, \varphi^{(i)}) = \nabla_{\boldsymbol{x}} f(\boldsymbol{x}) + \sum_{j=1}^{n} \left[\lambda_j^{(i)} + \varphi^{(i)} h_j(\boldsymbol{x})\right] \nabla_{\boldsymbol{x}} h_j(\boldsymbol{x}) \approx \mathbf{0}. \quad (5.5)$$

Comparing Equation (5.5) to the KKT optimality condition, the optimal Lagrange multiplier (see the proof in Bertsekas, 1999, p. 392–393) is

$$\lambda_j^{\star} \approx \lambda_j^{(i)} + \varphi^{(i)} h_j(\boldsymbol{x}). \quad (5.6)$$

Rearranging Equation (5.6) as

$$h_j(\boldsymbol{x}) \approx \frac{1}{\varphi^{(i)}} (\lambda_j^{\star} - \lambda_j^{(i)}), \quad (5.7)$$

it is clear that a feasible solution ($h_j(\boldsymbol{x}) \to 0$) is achieved when:

(i) $\lambda_j^{(i)}$ is close to $\lambda_j^{\star}$, or

(ii) $\varphi^{(i)} \to \infty$.

In practice, one does not know who is $\lambda_j^{\star}$, and Item (i) loses its sense. On the other hand, Item (ii) is quite useful since it can generate a decent estimate of $\boldsymbol{x}^{\star}$ with 'modest' values of $\varphi^{(i)}$ – a great benefit of the ALM.

Finally, motivated by Equation (5.6), the Lagrange multipliers can be updated by

$$\lambda_j^{(i+1)} = \lambda_j^{(i)} + \varphi^{(i)} h_j(\boldsymbol{x}), \quad \text{for } j = 1, 2, \ldots, n, \quad (5.8)$$

and the penalty parameter is usually actualized by

$$\varphi^{(i+1)} = \min\{\phi \varphi^{(i)}, \varphi_{max}\}, \quad (5.9)$$

where $\phi > 1$ is a constant. In general, $\lambda_j^{(0)} = 0$, whereas the choice for $\varphi^{(0)}$ is not trivial and may need some experimentation to find the best value.

5.2.2 Augmented Lagrangian Method in Inequality-Constrained Problems

Contemplate the following optimization problem with r inequality constraints, $c_j(\boldsymbol{x})$:

$$\begin{aligned} \min_{\boldsymbol{x}} \quad & f(\boldsymbol{x}) \\ \text{s.t.:} \quad & c_j(\boldsymbol{x}) \leqslant 0, \quad \text{for } j = 1, 2, \ldots, r. \end{aligned} \quad (5.10)$$

The Problem (5.10) can be converted to an equality-constrained problem through a simple transformation based on the observation that $c_j(\boldsymbol{x}) \leqslant 0$ if

and only if there is a variable $s_j \geqslant 0$ such that $c_j(\boldsymbol{x}) + s_j = 0$ (Boyd & Vandenberghe, 2004).

Thus, with the addition of *slack variables*, s_j, we have to

$$\begin{aligned} \min_{\boldsymbol{x},\boldsymbol{s}} \quad & f(\boldsymbol{x}) \\ \text{s.t.:} \quad & c_j(\boldsymbol{x}) + s_j = 0, \quad \text{for } j = 1, 2, \ldots, r, \\ & s_j \geqslant 0, \quad \text{for } j = 1, 2, \ldots, r, \end{aligned} \tag{5.11}$$

which has the following format when using the ALM:

$$\begin{aligned} \min_{\boldsymbol{x},\boldsymbol{s}} \quad & \mathcal{L}_A^0(\boldsymbol{x}, \boldsymbol{s}, \boldsymbol{\mu}, \varphi) = f(\boldsymbol{x}) + \sum_{j=1}^{r} \left[\mu_j \left(c_j(\boldsymbol{x}) + s_j \right) + \frac{\varphi}{2} \left(c_j(\boldsymbol{x}) + s_j \right)^2 \right] \\ \text{s.t.:} \quad & s_j \geqslant 0, \quad \text{for } j = 1, 2, \ldots, r. \end{aligned} \tag{5.12}$$

Problem (5.12) is analogous to Problem (5.4). Here, however, μ_j indicates the Lagrange multiplier associated with the j-th inequality constraint.

To solve optimizations like that, we first optimize $\mathcal{L}_A^0$ w.r.t. $\boldsymbol{s}$,

$$\begin{aligned} \min_{\boldsymbol{s}} \quad & \mathcal{L}_A(\boldsymbol{x}, \boldsymbol{\mu}, \varphi) = \mathcal{L}_A^0(\boldsymbol{x}, \boldsymbol{s}, \boldsymbol{\mu}, \varphi)\Big|_{\boldsymbol{x} \text{ fix}}, \\ \text{s.t.:} \quad & s_j \geqslant 0, \quad \text{for } j = 1, 2, \ldots, r, \end{aligned} \tag{5.13}$$

and, then, its result, we optimize $\mathcal{L}_A$ w.r.t. $\boldsymbol{x}$.

Problem (5.13) may be readily solved by taking the first derivative of $\mathcal{L}_A^0$, equating it to zero, and solving it for each s_j individually. Then,

$$\begin{aligned} \frac{\partial \mathcal{L}_A^0}{\partial s_j} &= \mu_j + \varphi \left(c_j(\boldsymbol{x}) + s_j \right) = 0 \\ s_j &= \max \left\{ 0, -\left(\frac{\mu_j}{\varphi} + c_j(\boldsymbol{x}) \right) \right\}, \end{aligned} \tag{5.14}$$

where the $\max\{\bullet\}$ function was added to Equation (5.14) to incorporate the fact that the *slack variables* must assume non-negative values.

Denoting $c_j^+(\boldsymbol{x}, \boldsymbol{\mu}, \varphi) = c_j(\boldsymbol{x}) + s_j$, we may establish that

$$c_j^+(\boldsymbol{x}, \boldsymbol{\mu}, \varphi) = \max \left\{ c_j(\boldsymbol{x}), -\frac{\mu_j}{\varphi} \right\}, \tag{5.15}$$

and the ALM-based optimization problem with inequality constraints becomes

$$\min_{\boldsymbol{x}} \quad f(\boldsymbol{x}) + \sum_{j=1}^{r} \left[\mu_j^{(i)} c_j^+(\boldsymbol{x}, \boldsymbol{\mu}^{(i)}, \varphi^{(i)}) + \frac{\varphi^{(i)}}{2} c_j^+(\boldsymbol{x}, \boldsymbol{\mu}^{(i)}, \varphi^{(i)})^2 \right], \tag{5.16}$$

where the superscript $(\bullet)^{(i)}$ was added as a reminder that the parameters correspond to the Subproblem at the i-th iteration.

Similarly to Equation (5.8), the Lagrange multipliers associated with inequality constraints are updated using the relation

$$\mu_j^{(i+1)} = \mu_j^{(i)} + \varphi^{(i)} c_j^+(\boldsymbol{x}, \boldsymbol{\mu}^{(i)}, \varphi^{(i)}), \quad \text{for } j = 1, 2, \ldots, r, \tag{5.17}$$

with $\mu_j^{(0)} = 0$. In turn, the penalty coefficient for the $(i+1)$-th iteration, $\varphi^{(i+1)}$, is calculated as stated in Equation (5.9).

According to da Senhora *et al.* (2020), the Lagrangian multiplier, $\mu_j^{(i)}$, and the penalty parameter, $\varphi^{(i)}$, stay constant for each ALM subproblem. This means the augmented Lagrangian function is continuously differentiable at each step even with the non-differentiable $\max\{\bullet\}$ function.

5.2.3 Augmented Lagrangian Method in Stress-Constrained Topology Optimization

The discussion of this section is based on the works of da Senhora *et al.* (2020) and Giraldo-Londoño & Paulino (2021). Assuming a linear elastic response, the optimization problem by means of ALM is

$$\begin{aligned} \min_{\boldsymbol{z}} \quad & m(\boldsymbol{z}) = \frac{1}{V_0} \sum_{e=1}^{N_e} \tilde{\rho}_e(\boldsymbol{z}) V_e \\ \text{s.t.:} \quad & g_j(\boldsymbol{z}, \boldsymbol{u}) \leqslant 0, \quad \text{for } j = 1, 2, \ldots, N_c \\ & 0 \leqslant z_k \leqslant 1, \quad \text{for } k = 1, 2, \ldots, N_d \\ \text{with} \quad & \boldsymbol{K}(\boldsymbol{z})\boldsymbol{u} = \boldsymbol{f}, \end{aligned} \tag{5.18}$$

where V_0 is the initial amount of volume, V_e is the volume of the e-th element – which is parameterized by $\tilde{\rho}_e$ –, g_j may be one of the constraints of Section 5.1.1, N_d is the number of design variables, and $\boldsymbol{f}$ is the vector of applied forces.

The corresponding augmented Lagrangian function at the i-th iteration is

$$\mathcal{L}_A^{(i)}(\boldsymbol{z}, \boldsymbol{\mu}^{(i)}, \varphi^{(i)}) = m(\boldsymbol{z}) + \zeta \sum_{j=1}^{N_c} \left[\mu_j^{(i)} g_j(\boldsymbol{z}, \boldsymbol{u}) + \frac{\varphi^{(i)}}{2} g_j(\boldsymbol{z}, \boldsymbol{u})^2 \right]. \tag{5.19}$$

The magnitude of the second term[11] in Equation (5.19) (that is, the term under the summation symbol) is impacted by the number of constraints, N_c: the higher N_c is, the higher will be the contribution of this term, and vice versa. So, the factor

$$\zeta = \frac{1}{N_c} \tag{5.20}$$

was introduced as an attempt to keep the augmented Lagrangian function independent of the number of constraints (da Senhora *et al.*, 2020).

[11] This is sometimes called a penalty term. Nevertheless, following the traditional nomenclature, the penalty term corresponds uniquely to the quadratic function, i.e., to the third term in Equation (5.19).

To summarize, the optimization problem for the ALM involves solving the i-th subproblem

$$\begin{aligned} \min_{\boldsymbol{z}} \quad & \mathcal{L}_A^{(i)}(\boldsymbol{z}, \boldsymbol{\mu}^{(i)}, \varphi^{(i)}) = m(\boldsymbol{z}) + \zeta \mathcal{A}^{(i)}(\boldsymbol{z}, \boldsymbol{\mu}^{(i)}, \varphi^{(i)}), \\ \text{s.t.:} \quad & 0 \leqslant z_k \leqslant 1, \quad \text{for } k = 1, 2, \ldots, N_d \\ \text{with} \quad & \boldsymbol{K}(\boldsymbol{z})\boldsymbol{u} = \boldsymbol{f}, \end{aligned} \tag{5.21}$$

and

$$\mathcal{A}^{(i)}(\boldsymbol{z}, \boldsymbol{\mu}^{(i)}, \varphi^{(i)}) = \sum_{j=1}^{N_c} \left[\mu_j^{(i)} g_j^+(\boldsymbol{z}, \boldsymbol{u}) + \frac{\varphi^{(i)}}{2} g_j^+(\boldsymbol{z}, \boldsymbol{u})^2 \right] \tag{5.22}$$

is an auxiliary term that combines the Lagrangian form, $\mathcal{L}$, and the penalty term, Φ, whereas g_j^+ is equivalent to c_j^+ in Section 5.2.2. We extend the formulation of Equations (5.21) and (5.22) to geometrical and material nonlinearities in Chapter 6.

6
Topology Optimization Under Nonlinearities

"We are here to help each other get through this thing, whatever it is."

Vonnegut, K. (1922–2007)

In this chapter, we formulate the optimization problem we seek to solve. We also explore the challenges that large deformations offer to density-driven topology optimization approaches and discuss possible ways to mitigate those effects. We thoroughly developed the sensitivity computation, which must account for issues related to both large deformations and stress constraints. Lastly, our sensitivity investigation is validated, evoking a simple clamped beam.

6.1
Problem Formulation

We want to

$$\begin{aligned}
\min_{\boldsymbol{z}} \quad & m(\boldsymbol{z}) = \frac{1}{V_0}\sum_{e=1}^{N_e} \tilde{\rho}_e(\boldsymbol{z}) V_e && \text{(6.1a)}\\
\text{s.t.:} \quad & g_e(\boldsymbol{z}) = \frac{\sigma_e^{vM}(\boldsymbol{z})}{\sigma_{lim}} - 1 \leqslant 0, \quad \text{for } e = 1, 2, \ldots, N_e && \text{(6.1b)}\\
& 0 \leqslant z_e \leqslant 1, \quad \text{for } e = 1, 2, \ldots, N_e && \text{(6.1c)}\\
\text{with} \quad & \boldsymbol{r} = \boldsymbol{f}_{ext} - \boldsymbol{f}_{int} = \boldsymbol{0}, && \text{(6.1d)}
\end{aligned}$$

in which Equation (6.1d) corresponds to the equilibrium in nonlinear problems.

To solve Problem (6.1), we evoke the ALM of Section 5.2. Therefore, we have to deal with the statement

$$\begin{aligned}
\min_{\boldsymbol{z}} \quad & \mathcal{L}_A^{(i)}(\boldsymbol{z}, \boldsymbol{\mu}^{(i)}, \varphi^{(i)}) = m(\boldsymbol{z}) + \zeta \mathcal{A}^{(i)}(\boldsymbol{z}, \boldsymbol{\mu}^{(i)}, \varphi^{(i)}),\\
\text{s.t.:} \quad & 0 \leqslant z_e \leqslant 1, \quad \text{for } e = 1, 2, \ldots, N_e\\
\text{with} \quad & \boldsymbol{r} = \boldsymbol{f}_{ext} - \boldsymbol{f}_{int} = \boldsymbol{0}
\end{aligned} \qquad (6.2)$$

at the i-th iteration, where ζ is the defined in Equation (5.20), the auxiliary term, $\mathcal{A}^{(i)}$, follows Equation (5.22), and the stress constraints are in the form

of TVC or PVC, as detailed in Sections 5.1.1.1 and 5.1.1.2.

6.2 Nonlinear Analysis in Density-based Topology Optmization

In general, we work with fixed grids in topology optimization. This circumvents recreating the mesh at every iteration, which is even more time-consuming in nonlinear studies, due largely to incremental-iterative methods like the LCM of Section 3.1.1.

Low-density zones within the design domain are not resistant to significant deformations, particularly when compressed. Consequently, the mesh may become substantially distorted, leading to: (i) local buckling, and (ii) loss of ellipticity, i.e., the tangent stiffness matrix loses its positive definition, causing the nonlinear FE routine to break down. We draw our attention to this second issue because it may result in no convergence of the optimization procedure, which relies on satisfying Equation (6.1d).

Furthermore, if one views the second issue through the classical continuous mechanics' bias, one may encounter non-positive Jacobian ($J \leqslant 0$), leading to elements with null or negative volume – which is not contemplated in the theory. Alternatively, from the FE perspective, interpenetrated elements might lose their bi-univocal mapping between local and global coordinates. In this case, we are transgressing basic principles in both fields!

The literature has offered numerous strategies to deal with this kind of difficulty. Bruns & Tortorelli (1998) assumed a modified SVK material model to enhance the stiffness in large compressions. This option, though, has not proven to be trustworthy since it is not sufficiently robust and only occasionally solves the problem. Buhl *et al.* (2000) modified the NRP's convergence criterion, which we called the reduced convergence criterion (RCC), detailed in Section 6.2.1. Nevertheless, depending on the level of nonlinearity imposed, we found that the final layout becomes a tangle of wires, making deciphering the optimal topology an exceedingly hard task, if not impossible. Bruns & Tortorelli (2003) introduced an element removal and reintroduction technique, in which the eliminated material is freely reinserted in the design domain.

Yoon & Kim (2005) and Yoon *et al.* (2011) devised an approach using artificial zero-length elastic links. Following this idea, a node is connected to another by an elastically deformable link – the design variable –, and properly penalized to represent material. If a link has very low stiffness, no connection is set between the nodes; if a link has a high stiffness, the connection between nodes is maintained. Links with intermediate densities are evaluated as linear-elastic stiffness.

Kawamoto (2009) compared the NRP and the Levenberg-Marquardt method for solving incremental-iterative procedures in FE analysis. He found compliance mechanisms with a single input/output port performed better when employing the Levenberg-Marquardt method, whereas those with multiple inputs or outputs did better using the NRP. Lee & Park (2012) employed the equivalent static load method to turn the response of a static nonlinear optimization problem into a linear one. To deal with high distortions in quasi-voids, a variable transformation strategy was utilized and derived using linear static optimization findings, and an updating technique based on comparable static loads was proposed.

Lahuerta *et al.* (2013) used a specific function in combination with the polyconvex Simo-Ciarlet neo-Hookean material model to stabilize the distortion of low-density elements. Gomes & Senne (2014) developed the sequential piecewise linear programming to handle geometrical nonlinear topology optimization problems. Wang *et al.* (2014) interpolates the strain energy function between linear and nonlinear values according to the density, resulting in what is called the energy interpolation scheme (EIS) – *vid.* Section 6.2.1. Several studies have effectively used the EIS, such as Zhu *et al.* (2021), which addresses geometrical nonlinear topology optimization problems in the FreeFEM open-source framework (Hecht, 2012).

Luo *et al.* (2015) presented the additive hyperelasticity technique (AHT). The idea is to superimpose two equal meshes with the same degrees of freedom: one characterized by the desired (hyperelastic) model, which describes the structural material, and another defined by a softer material model, typically Yeoh. Blending two materials in a linear interpolation produces a composite that can converge in the NRP. The most challenging aspect is the updating scheme required for the Yeoh parameters, based on the von Mises deformation level, in which we are not sure how well it will perform in circumstances other than compliance-related problems. Chen *et al.* (2019) recently connected the AHT to ANSYS®, leading to a more reliable and quick FE analysis.

Senne *et al.* (2023) investigated inexact approximations of NRP to reduce the computational cost of performing the incremental-iterative techniques in nonlinear FE. The authors claim that this method reduced the overall optimization cost by 70%. Yet, it is still confined to compliance minimization problems, and more studies are needed to demonstrate its generalizability. Wang *et al.* (2023) explored geometrical nonlinearity in topology optimization under pressure loads. They provided an accurate pressure-imposition technique and demonstrated its significance in the optimal layout.

In the following, we will discuss the RCC and EIS, which, alongside the

AHT, are the most prominent methods for dealing with numerical instabilities in void elements.

6.2.1 Reduced Convergence Criterion

Incremental-iterative algorithms typically cease when the accepted convergence criteria fall below the stated tolerance. In continuous topology optimization with finite deformations, the NRP oscillates and may not converge. Buhl *et al.* (2000) found that these oscillations occur at nodes surrounded by quasi-voids. Since these nodes (*vid.* Figure 6.1) are not part of the final structural layout, they recommended removing them from the convergence criteria. Thus, commonly, density values less than 0.001 are removed.

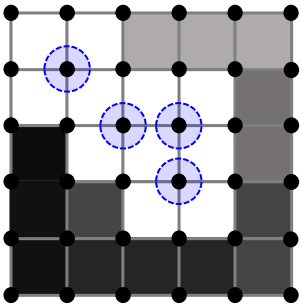

Figure 6.1: Reduced convergence criterion, RCC. The indicated nodes are not part of the convergence criteria.

No further modifications are necessary to evaluate the sensitivities. However, over the years, this technique has shown to be less reliable than at the time of its creation, and new options are welcome – see, for instance, Section 6.2.3.

6.2.2 Energy Interpolation Scheme

The energy interpolation scheme, EIS, of Wang *et al.* (2014), consists of interpolating the strain energy function between its finite and infinitesimal deformation theories, respectively, W^{NL}, and W^{L}. Essentially, the EIS may be characterized as

$$W_e(\check{\rho}_e, \gamma_e, \boldsymbol{u}_e) = [W_e^{NL}(\gamma_e(\check{\rho}_e)\boldsymbol{u}_e) - W_e^{L}(\gamma_e(\check{\rho}_e)\boldsymbol{u}_e) + W_e^{L}(\boldsymbol{u}_e)]\check{\rho}_e, \tag{6.3}$$

where $\check{\rho}_e$ and $\boldsymbol{u}_e$ are, respectively, the design variable and displacement associated with the e-th element.

The interpolation factor, γ_e, dictates the transition from modest to big deformations. If $\gamma_e \to 0 \therefore W_e \to W_e^L(\boldsymbol{u}_e)\check{\rho}_e$; otherwise, if $\gamma_e \to 1 \therefore W_e \to W_e^{NL}(\boldsymbol{u}_e)\check{\rho}_e$.

To attain a smooth differentiable expression, Wang *et al.* (2014) proposed that the transition between these two zones is regulated by

$$\gamma_e(\check{\rho}_e, \beta_1, \eta_1) = \frac{\tanh(\beta_1\eta_1) + \tanh(\beta_1(\check{\rho}_e - \eta_1))}{\tanh(\beta_1\eta_1) + \tanh(\beta_1(1 - \eta_1))} \tag{6.4}$$

with $\beta_1 = 500$ and $\eta_1 = 0.01$. The parameter β_1 controls the smoothness of the transition, while η_1 is the cutoff variable: values below it assume a linear behavior, whereas those above it present large deformations.

Zhang *et al.* (2018) introduced another expression in the form of

$$\gamma_e(\check{\rho}_e, \beta_2, \eta_2) = \frac{\mathrm{e}^{\beta_2\check{\rho}_e}}{\mathrm{e}^{\beta_2\check{\rho}_e} + \mathrm{e}^{\beta_2\rho_2}}, \tag{6.5}$$

with β_2 and η_2, variable. Nevertheless, notice that when $\check{\rho}_e = 0$, $\gamma_e \neq 0$. This means Equation (6.5) will invariably include a certain amount of nonlinearity, impacting the inherent behavior of the EIS, particularly that of its derivatives.

6.2.2.1 Practical Implementation

The deformation gradient must be recalculated to comply with the EIS. So, to the e-th element,

$$\boldsymbol{F}_e^{EIS} = \gamma_e \frac{\partial \boldsymbol{u}_e}{\partial \boldsymbol{X}} + \boldsymbol{I}. \tag{6.6}$$

To recall, the linear stored energy function of the e-th element is

$$W_e^L(\boldsymbol{u}_e) = \frac{1}{2}\boldsymbol{f}_{exte}^T\boldsymbol{u}_e = \frac{1}{2}\boldsymbol{u}_e^T\boldsymbol{K}_{Te}\boldsymbol{u}_e \tag{6.7}$$

and the strain energy is $W_e^L(\gamma_e\boldsymbol{u}_e) = \gamma_e^2 W_e^L(\boldsymbol{u}_e)$. Putting this result into Equation (6.3) and rearranging it, we may write the EIS as

$$W_e(\check{\rho}_e, \gamma_e, \boldsymbol{u}_e) = [W_e^{NL}(\gamma_e\boldsymbol{u}_e) + (1 - \gamma_e^2)W_e^L(\boldsymbol{u}_e)]\check{\rho}_e. \tag{6.8}$$

Now, consider the definition of internal force:

$$\boldsymbol{f}_{inte}(\check{\rho}_e, \gamma_e, \boldsymbol{u}_e) = \frac{\partial}{\partial \boldsymbol{u}_e}\int_{\Omega_0} W_e \,\mathrm{d}V \equiv \int_{\Omega_0} \frac{\partial W_e(\check{\rho}_e, \gamma_e, \boldsymbol{u}_e)}{\partial \boldsymbol{u}_e}\,\mathrm{d}V. \tag{6.9}$$

Substituting Equation (6.9) into Equation (6.8), after a few manipulations, yields

$$\begin{aligned}\boldsymbol{f}_{inte}(\check{\rho}_e, \gamma_e, \boldsymbol{u}_e) = &\int_{\Omega_0} \frac{\partial W_e^{NL}(\gamma_e\boldsymbol{u}_e)}{\partial(\gamma_e\boldsymbol{u}_e)}\frac{\partial(\gamma_e\boldsymbol{u}_e)}{\partial \boldsymbol{u}_e}\check{\rho}_e \,\mathrm{d}V + \\ &(1 - \gamma_e^2)\int_{\Omega_0} \frac{\partial W_e^L(\boldsymbol{u}_e)}{\partial \boldsymbol{u}_e}\check{\rho}_e \,\mathrm{d}V,\end{aligned} \tag{6.10}$$

or, in a simpler version,

$$\boldsymbol{f}_{inte}(\check{\rho}_e, \gamma_e, \boldsymbol{u}_e) = \left(\gamma_e\boldsymbol{f}_{inte}^{NL}(\gamma_e\boldsymbol{u}_e) + (1 - \gamma_e^2)\boldsymbol{f}_{inte}^L(\boldsymbol{u}_e)\right)\check{\rho}_e, \tag{6.11}$$

which expresses the interpolation scheme operating on each element e as a function of the internal force vector, composed of the linear and nonlinear terms, respectively, $\boldsymbol{f}_{inte}^{L}$ and $\boldsymbol{f}_{inte}^{NL}$.

Equation (6.11) is particularly relevant for linking with FE equations since one can simply add the interpolation factor, γ_e, to the computation of deformation measures to get $\boldsymbol{f}_{inte}^{NL}$, while $\boldsymbol{f}_{inte}^{L}$ is a straightforward calculation. In this sense, the linear and nonlinear internal force parcels of the e-th element are, respectively,

$$\boldsymbol{f}_{inte}^{L} = \int_{\Omega_0} \boldsymbol{B}_L^T \mathbf{S} \, \mathrm{d}V \tag{6.12}$$

$$\boldsymbol{f}_{int\ e}^{NL} = \int_{\Omega_0} \boldsymbol{B}_N^T \mathbf{S} \, \mathrm{d}V, \tag{6.13}$$

where

$$\boldsymbol{B}_L = \begin{bmatrix} N_{1,1} & 0 & 0 & N_{2,1} & 0 & 0 & \cdots & N_{n,1} & 0 & 0 \\ 0 & N_{1,2} & 0 & 0 & N_{2,2} & 0 & \cdots & 0 & N_{n,2} & 0 \\ 0 & 0 & N_{1,3} & 0 & 0 & N_{2,3} & \cdots & 0 & 0 & N_{n,3} \\ N_{1,2} & N_{1,1} & 0 & N_{2,2} & N_{2,1} & 0 & \cdots & N_{n,2} & N_{n,1} & 0 \\ 0 & N_{1,3} & N_{1,2} & 0 & N_{2,3} & N_{2,2} & \cdots & 0 & N_{n,3} & N_{n,2} \\ N_{1,3} & 0 & N_{1,1} & N_{2,3} & 0 & N_{2,1} & \cdots & N_{n,3} & 0 & N_{n,1} \end{bmatrix}, \tag{6.14}$$

$$\boldsymbol{B}_N = \begin{bmatrix} F_{11}N_{n,1} & F_{21}N_{n,1} & F_{31}N_{n,1} \\ F_{12}N_{n,2} & F_{22}N_{n,2} & F_{32}N_{n,2} \\ F_{13}N_{n,3} & F_{23}N_{n,3} & F_{33}N_{n,3} \\ F_{11}N_{n,2} + F_{12}N_{n,2} & F_{21}N_{n,2} + F_{22}N_{n,2} & F_{31}N_{n,2} + F_{32}N_{n,2} \\ F_{12}N_{n,3} + F_{22}N_{n,2} & F_{22}N_{n,3} + F_{23}N_{n,2} & F_{32}N_{n,3} + F_{33}N_{n,2} \\ F_{13}N_{n,1} + F_{11}N_{n,3} & F_{23}N_{n,1} + F_{21}N_{n,3} & F_{34}N_{n,1} + F_{31}N_{n,3} \end{bmatrix}, \tag{6.15}$$

with n being the number of nodes in the element. $\mathbf{S}$ corresponds to the PK2 stress vector attained from the reduction of the PK2 stress tensor, $\boldsymbol{S}$, and $N_{a,b} = \partial N_a / \partial x_b$ is the derivative of the shape functions at node a.

Notably, Equations (6.14) and (6.15) are three-dimensional expressions. Though, two-dimensional matrices are easily obtained by eliminating the variables associated with the third dimension.

The EIS also involves an alteration in the stiffness matrix computation. Thus, we have

$$\begin{aligned}\boldsymbol{K}_{Te}(\check{\rho}_e,\gamma_e,\boldsymbol{u}_e) &= \frac{\partial \boldsymbol{f}_{inte}(\check{\rho}_e,\gamma_e,\boldsymbol{u}_e)}{\partial \boldsymbol{u}_e}\\ &= \check{\rho}_e\gamma_e\frac{\partial \boldsymbol{f}^{NL}_{inte}(\gamma_e\boldsymbol{u}_e)}{\partial(\gamma_e\boldsymbol{u}_e)}\frac{\partial(\gamma_e\boldsymbol{u}_e)}{\partial \boldsymbol{u}_e} + \check{\rho}_e(1-\gamma_e^2)\frac{\partial \boldsymbol{f}^{L}_{inte}(\boldsymbol{u}_e)}{\partial \boldsymbol{u}_e}\\ &= \left(\gamma_e^2\boldsymbol{K}^{NL}_{Te}(\gamma_e\boldsymbol{u}_e) + (1-\gamma_e^2)\boldsymbol{K}^{L}_{Te}(\boldsymbol{u}_e)\right)\check{\rho}_e,\end{aligned} \tag{6.16}$$

where $\boldsymbol{K}^L_{Te}$ corresponds to the stiffness matrix obtained by small deformation theory, and $\boldsymbol{K}^{NL}_{Te}$ represents the same quantity assuming finite deformations. Correspondingly,

$$\boldsymbol{K}^L_{Te} = \int_{\Omega_0} \boldsymbol{B}_L^T\mathbf{D}\boldsymbol{B}_L\,\mathrm{d}V \tag{6.17}$$

$$\boldsymbol{K}^{NL}_{Te} = \int_{\Omega_0} \boldsymbol{B}_N^T\mathbf{D}\boldsymbol{B}_N + \boldsymbol{B}_G^T\boldsymbol{\Sigma}\boldsymbol{B}_G\,\mathrm{d}V, \tag{6.18}$$

in which

$$\boldsymbol{\Sigma} = \begin{bmatrix} S_{11} & S_{12} & S_{13} & 0 & 0 & 0\\ S_{21} & S_{22} & S_{23} & 0 & 0 & 0\\ S_{31} & S_{32} & S_{33} & 0 & 0 & 0\\ 0 & 0 & 0 & S_{11} & S_{12} & S_{13}\\ 0 & 0 & 0 & S_{21} & S_{22} & S_{23}\\ 0 & 0 & 0 & S_{31} & S_{32} & S_{33}\end{bmatrix}, \quad \text{and} \tag{6.19}$$

$$\boldsymbol{B}_G = \begin{bmatrix} N_{1,1} & 0 & 0 & N_{2,1} & 0 & 0 & \cdots & N_{n,1} & 0 & 0\\ N_{1,2} & 0 & 0 & N_{2,2} & 0 & 0 & \cdots & N_{n,2} & 0 & 0\\ N_{1,3} & 0 & 0 & N_{2,3} & 0 & 0 & \cdots & N_{n,3} & 0 & 0\\ 0 & N_{1,1} & 0 & 0 & N_{2,1} & 0 & \cdots & 0 & N_{n,1} & 0\\ 0 & N_{1,3} & 0 & 0 & N_{2,2} & 0 & \cdots & 0 & N_{n,2} & 0\\ 0 & N_{1,3} & 0 & 0 & N_{2,3} & 0 & \cdots & 0 & N_{n,3} & 0\\ 0 & 0 & N_{1,1} & 0 & 0 & N_{2,1} & \cdots & 0 & 0 & N_{n,1}\\ 0 & 0 & N_{1,2} & 0 & 0 & N_{2,2} & \cdots & 0 & 0 & N_{n,2}\\ 0 & 0 & N_{1,3} & 0 & 0 & N_{2,3} & \cdots & 0 & 0 & N_{n,3}\end{bmatrix}. \tag{6.20}$$

Again, these are three-dimensional equations that can be easily reduced to two-dimensional instances.

Considering the contributions of all N_e elements in the design domain, we assemble

$$\boldsymbol{f}_{int} = \bigwedge_{e=1}^{N_e} \boldsymbol{f}_{inte} \quad \text{and} \quad \boldsymbol{K}_T = \bigwedge_{e=1}^{N_e} \boldsymbol{K}_{Te}. \tag{6.21}$$

6.2.3
C-Shape

Consider the short C-shape geometry of Figure 6.2. The dark element represents the structural part with $\check{\rho} = 1$, whereas the light one corresponds to low-stiffness elements ($\check{\rho} = \epsilon = 10^{-8}$). Here, we study the impact of different tactics on the nonlinear FE routine by comparing the so-called direct approach (i.e., solving nonlinear FE without further techniques), the RCC, and the EIS.

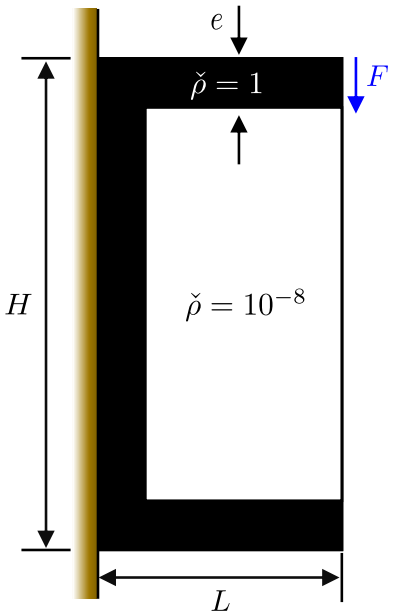

Load & Geometry:
$F = 2$
$L = 40$
$H = 80$
$e = 10$
$t = 1$

Material Properties:
$E_0 = 10$
$\nu_0 = 0.4$

Data for LCM:
Step factor, $\overline{\Delta\lambda}_s = 0.1$
Max. iter. per step = 10

Figure 6.2: C-shape (consistent units applied).

In this example, we assume the residual tolerance $||\boldsymbol{r}|| \leqslant 10^{-6}$ as the convergence criterion, and the simulations are carried out under plane stress conditions on meshes with 40 x 80 bilinear elements. The load is uniformly distributed among the nodes of the line in the upper right corner, whereas the left side of the structure is limited to in-plane motions.

Figure 6.3 presents solutions with SVK as the material model. We were unable to achieve convergence in the NRP for the studied methods since the algorithm ceased after reaching the maximum number of allowable iterations. According to Figure 6.5(a), both the direct approach and the RCC halted at just 30% of load, whereas the EIS withstood double the force until failure. In particular, the RCC-achieved design formed a tangle of lines, which, in complex analysis, may render the interpretation of the optimum design impossible. In contrast, the EIS solution produced a layout where material was interpenetrated. This is because the SVK model did not provide enough compressibility to withstand the deformations, resulting in quasi-voids shifting to the left. As a result, we must resort to alternative strategies.

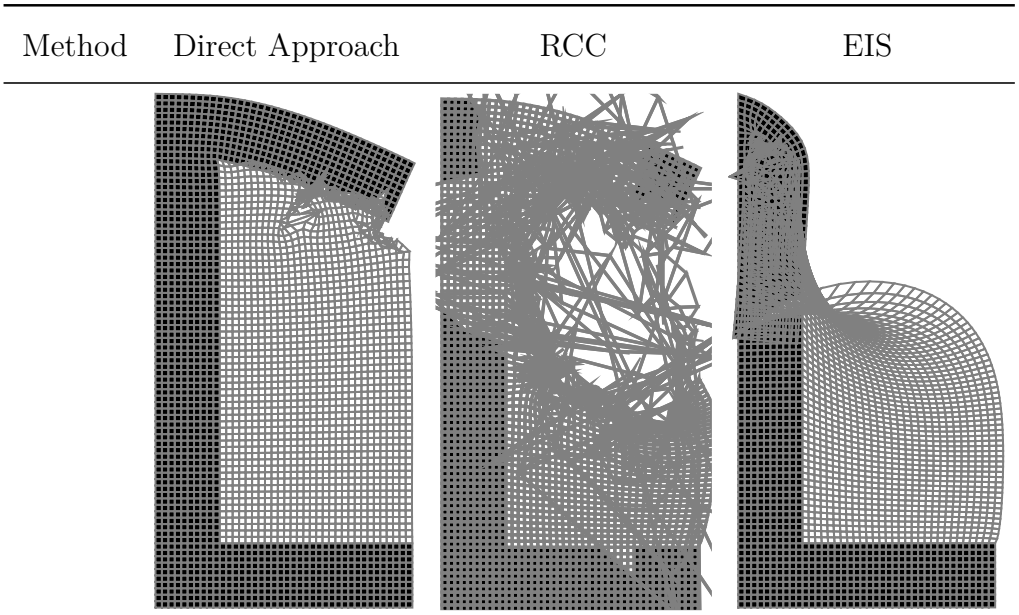

Figure 6.3: Effect of direct approach, RCC, and EIS in the LCM for the SVK model.

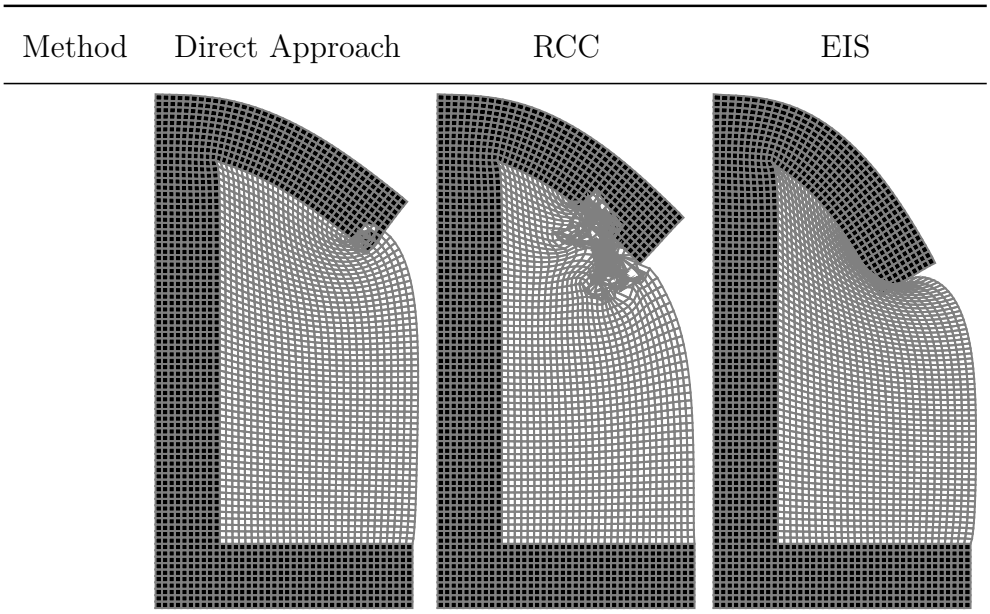

Figure 6.4: Effect of direct approach, RCC, and EIS in the LCM for the nH-SC model.

Using a model resistant to large compressions results in clearer (and less distorted) designs, as illustrated in Figure 6.4. We could not achieve convergence using either the direct approach or the RCC. As seen in Figure 6.5(b), the direct approach failed at 50% of load, whereas the solution using the RCC diverges in the next load step. In turn, the EIS generated a well-defined deformed structure, capable of bearing the imposed load. Observing Figure 6.6, the C-shape deformation made solely of structural elements corresponds to the same achieved by employing the EIS and nH-SC material model.

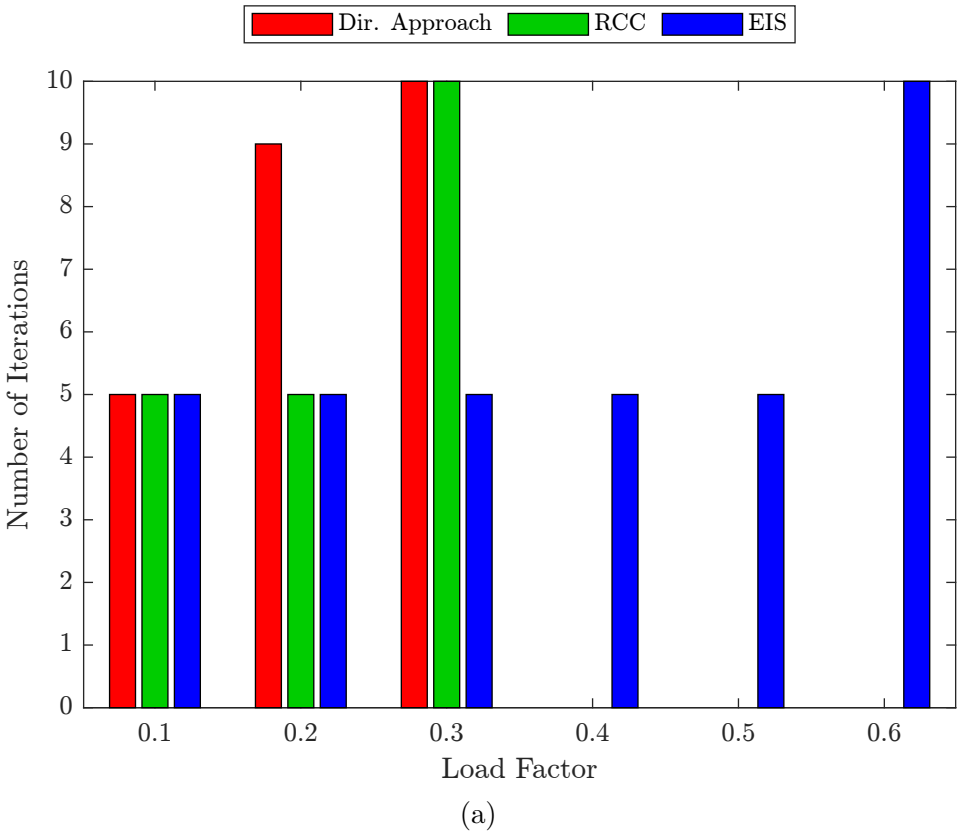

(a)

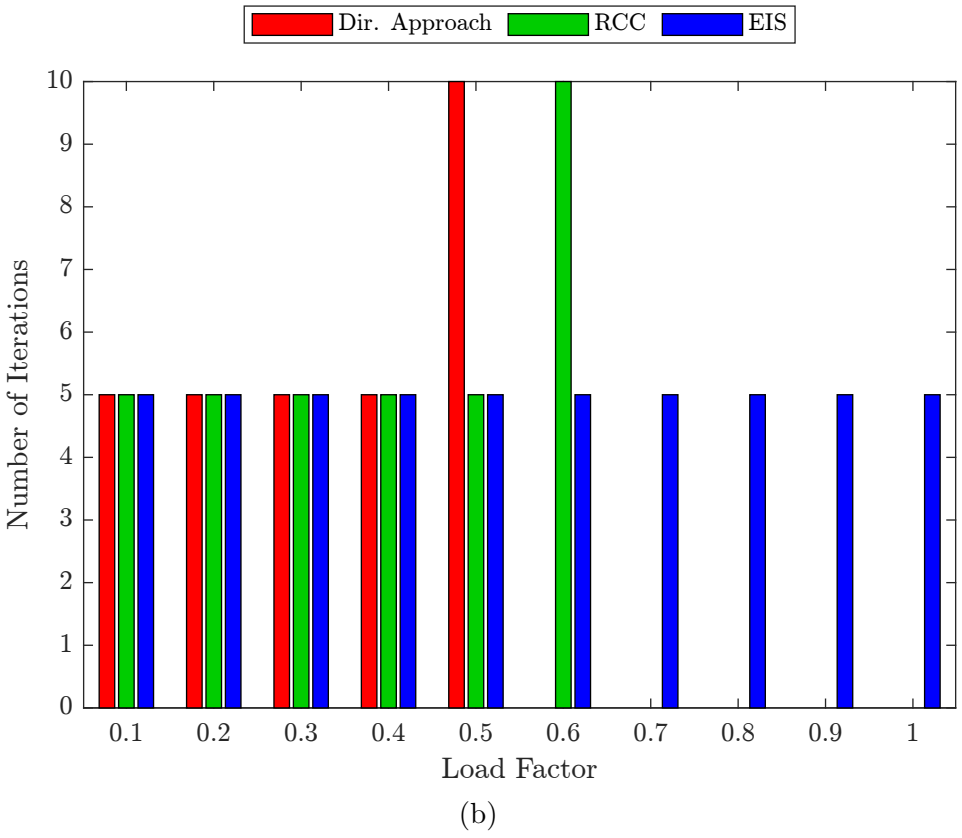

(b)

Figure 6.5: Number of iterations per load increment for (a) SVK model and (b) for nH-SC model.

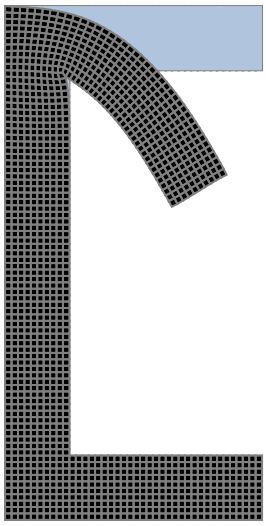

Figure 6.6: C-shape deformation.

From this simple example, we can infer that:

(i) nH-SC material model seems to outperform the SVK law,

(ii) nH models alone may not be enough to overcome void instabilities, and

(iii) the RCC and the direct approach have downsides, such as material interpretation, which may complicate postprocessing studies of the optimized layout.

6.2.4 Sensitivity Analysis

To deduce the derivatives, we go back to the augmented Lagrangian function:

$$\mathcal{L}_A^{(i)}(\boldsymbol{z}, \boldsymbol{\mu}^{(i)}, \varphi^{(i)}) = m(\boldsymbol{z}) + \frac{1}{N_c} \underbrace{\sum_{j=1}^{N_c} \left[\mu_j^{(i)} g_j^+(\boldsymbol{z}, \boldsymbol{u}) + \frac{\varphi^{(i)}}{2} g_j^+(\boldsymbol{z}, \boldsymbol{u})^2 \right]}_{\mathcal{A}^{(i)}(\boldsymbol{z}, \boldsymbol{\mu}^{(i)}, \varphi^{(i)})}. \tag{6.22}$$

Owing to the variables at play, the derivative of Equation (6.22) may be split into two halves, expressed in terms of the chain rule:

$$\frac{\partial \mathcal{L}_A^{(i)}}{\partial \boldsymbol{z}} = \left(\frac{\partial m}{\partial \tilde{\boldsymbol{\rho}}} + \frac{1}{N_c} \frac{\partial \mathcal{A}^{(i)}}{\partial \check{\boldsymbol{\rho}}} \frac{\partial \check{\boldsymbol{\rho}}}{\partial \tilde{\boldsymbol{\rho}}} \right) \frac{\partial \tilde{\boldsymbol{\rho}}}{\partial \boldsymbol{\rho}} \frac{\partial \boldsymbol{\rho}}{\partial \boldsymbol{z}} \tag{6.23}$$

with

$$\frac{\partial \check{\boldsymbol{\rho}}}{\partial \tilde{\boldsymbol{\rho}}} = p(1-\epsilon)\tilde{\boldsymbol{\rho}}^{p-1}, \tag{6.24}$$

$$\frac{\partial \tilde{\boldsymbol{\rho}}}{\partial \boldsymbol{\rho}} = \frac{-\beta(\tanh^2(\beta(\eta - \boldsymbol{\rho})) - 1)}{\tanh(\beta\eta) - \tanh(\beta(\eta - 1))}, \quad \text{and} \tag{6.25}$$

$$\frac{\partial \boldsymbol{\rho}}{\partial \boldsymbol{z}} = \boldsymbol{M}, \tag{6.26}$$

according to Equations (4.4), (4.3) and (4.1), respectively. The remaining terms will be defined below.

6.2.4.1 Computation of $\partial m/\partial\tilde{\rho}_e$

The objective's derivative in Equation (6.1a) is just as simple as

$$\frac{\partial m}{\partial\tilde{\rho}_e} = \frac{V_e}{\sum_e V_e}, \tag{6.27}$$

where V_e is the volume of the e-th element. We consider a fixed thickness, t, in two-dimensional analyses, and only the in-plane dimensions vary.

6.2.4.2 Computation of $\partial\mathcal{A}^{(i)}/\partial\check{\rho}_e$

The auxiliary term derivative, $\mathcal{A}^{(i)}$, is given by

$$\frac{\partial\mathcal{A}^{(i)}}{\partial\check{\rho}_e} = \sum_{j=1}^{N_c}\left(\mu_j^{(i)} + \varphi^{(i)} g_j^+(\boldsymbol{z},\boldsymbol{u})\right)\left(\frac{\partial g_j^+}{\partial\check{\rho}_e}\bigg|_{\boldsymbol{u}\,\text{fix}} + \frac{\partial g_j^+}{\partial\boldsymbol{u}_j}\frac{\partial\boldsymbol{u}_j}{\partial\check{\rho}_e}\right). \tag{6.28}$$

Observe the constraint g_j^+ is affected by both the design variable, $\check{\rho}_e$, and the displacement field, $\boldsymbol{u}_j$. This culminates in two different terms: one explicit, $\partial g_j^+/\check{\rho}_e$, and another implicit, $\partial g_j^+/\partial\boldsymbol{u}_j \times \partial\boldsymbol{u}_j/\partial\check{\rho}_e$.

We adopt the adjoint approach for the sensitivity analysis to prevent the expensive computation of $\partial\boldsymbol{u}_j/\partial\check{\rho}_e$. With the help of Equation (6.1d), and assuming equilibrium, we get

$$\begin{aligned}\frac{\partial\boldsymbol{r}}{\partial\check{\rho}_e} &= \cancelto{0}{\frac{\partial\boldsymbol{f}_{ext}}{\partial\check{\rho}_e}} - \left(\frac{\partial\boldsymbol{f}_{int}}{\partial\check{\rho}_e}\bigg|_{\boldsymbol{u}\,\text{fix}} + \frac{\partial\boldsymbol{f}_{int}}{\partial\boldsymbol{u}}\frac{\partial\boldsymbol{u}}{\partial\check{\rho}_e}\right)\\ &= -\left(\frac{\partial\boldsymbol{f}_{int}}{\partial\check{\rho}_e}\bigg|_{\boldsymbol{u}\,\text{fix}} + \boldsymbol{K}_T\frac{\partial\boldsymbol{u}}{\partial\check{\rho}_e}\right) = \boldsymbol{0},\end{aligned} \tag{6.29}$$

where $\boldsymbol{K}_T$ is the global (tangent) stiffness matrix defined in Equation (6.16) and computed by means of Equation (6.21). We assume here the external force is design-variable independent, canceling the indicated term in Equation (6.29).

Without affecting the mathematical response, we may combine Equations (6.28) and (6.29) like

$$\begin{aligned}\frac{\partial\mathcal{A}^{(i)}}{\partial\check{\rho}_e} =& \sum_{j=1}^{N_c}\left[\mu_j^{(i)} + \varphi^{(i)} g_j^+(\boldsymbol{z},\boldsymbol{u})\right]\left(\frac{\partial g_j^+}{\partial\check{\rho}_e} + \frac{\partial g_j^+}{\partial\boldsymbol{u}_j}\frac{\partial\boldsymbol{u}_j}{\partial\check{\rho}_e}\right) -\\ & \boldsymbol{\xi}^T\left(\frac{\partial\boldsymbol{f}_{int}}{\partial\check{\rho}_e} + \boldsymbol{K}_T\frac{\partial\boldsymbol{u}}{\partial\check{\rho}_e}\right)\end{aligned} \tag{6.30}$$

with the inclusion of the adjoint vector $\boldsymbol{\xi}$.

Reorganizing Equation (6.30) yields

$$\begin{aligned}\frac{\partial \mathcal{A}^{(i)}}{\partial \check{\rho}_e} =& \sum_{j=1}^{N_c} \left[\mu_j^{(i)} + \varphi^{(i)} g_j^+(\boldsymbol{z}, \boldsymbol{u})\right] \frac{\partial g_j^+}{\partial \check{\rho}_e} - \boldsymbol{\xi}^T \frac{\partial \boldsymbol{f}_{int}}{\partial \check{\rho}_e} + \\ & \left(\sum_{j=1}^{N_c} \left[\mu_j^{(i)} + \varphi^{(i)} g_j^+(\boldsymbol{z}, \boldsymbol{u})\right] \frac{\partial g_j^+}{\partial \boldsymbol{u}_j} - \boldsymbol{\xi}^T \boldsymbol{K}_T\right) \frac{\partial \boldsymbol{u}}{\partial \check{\rho}_e},\end{aligned} \tag{6.31}$$

where the adjoint vector is evaluated nullifying the second term of Equation (6.31):

$$\boldsymbol{\xi}^T \boldsymbol{K}_T = \sum_{j=1}^{N_c} \left[\mu_j^{(i)} + \varphi^{(i)} g_j^+(\boldsymbol{z}, \boldsymbol{u})\right] \frac{\partial g_j^+}{\partial \boldsymbol{u}_j}. \tag{6.32}$$

Finally, the auxiliary term derivative is:

$$\boxed{\frac{\partial \mathcal{A}^{(i)}}{\partial \check{\rho}_e} = \sum_{j=1}^{N_c} \left[\mu_j^{(i)} + \varphi^{(i)} g_j^+(\boldsymbol{z}, \boldsymbol{u})\right] \frac{\partial g_j^+}{\partial \check{\rho}_e} - \boldsymbol{\xi}^T \frac{\partial \boldsymbol{f}_{int}}{\partial \check{\rho}_e}} \tag{6.33}$$

We still have to weigh the following derivatives: $\partial g_j^+ / \partial \boldsymbol{u}_j$, $\partial g_j^+ / \partial \check{\rho}_e$ and $\partial \boldsymbol{f}_{int} / \partial \check{\rho}_e$.

6.2.4.3 Computation of $\partial g_j^+ / \partial \boldsymbol{u}_j$

From the definition of c_j^+ in Equation (5.15), we conclude that

$$\frac{\partial g_j^+}{\partial \boldsymbol{u}_j} = \begin{cases} 0, & \text{if } g_j^+ < -\mu_j/\varphi, \text{ or} \\ \dfrac{\partial g_j^+}{\partial \sigma_j^{vM}} \dfrac{\partial \sigma_j^{vM}}{\partial \boldsymbol{\sigma}_j} \dfrac{\partial \boldsymbol{\sigma}_j}{\partial \boldsymbol{u}_j}, & \text{otherwise} \end{cases} \tag{6.34}$$

where

$$\frac{\partial g_j^+}{\partial \sigma_j^{vM}} = \begin{cases} \dfrac{\check{\rho}_j}{\sigma_{lim}}, & \text{in TVC, or} \\ \dfrac{\check{\rho}_j}{\sigma_{lim}} \left(3(g_j^+)^2 + 1\right), & \text{in PVC,} \end{cases} \tag{6.35}$$

and

$$\frac{\partial \sigma_j^{vM}}{\partial \boldsymbol{\sigma}_j} = \frac{\boldsymbol{V} \boldsymbol{\sigma}_j}{\sigma_j^{vM}}, \tag{6.36}$$

for $\boldsymbol{V}$ being defined by Equation (2.23). Keep in mind in Equations (6.34) and (6.36) we referred to the Cauchy stress vector, written in terms of the Voigt notation (see Section 1.5).

As stated in Section 6.2.2, we consider the EIS to address numerical instabilities in low-density elements, so the stresses must also be interpolated. Consequently, we adopted the following interpolation for the Cauchy stress:

$$\begin{aligned}\boldsymbol{\sigma}_j(\gamma_j, \boldsymbol{u}_j) &= \boldsymbol{\sigma}_j^{NL}(\gamma_j \boldsymbol{u}_j) - \boldsymbol{\sigma}_j^{L}(\gamma_j \boldsymbol{u}_j) + \boldsymbol{\sigma}_j^{L}(\boldsymbol{u}_j) \\ &= \boldsymbol{\sigma}_j^{NL}(\gamma_j \boldsymbol{u}_j) + (1 - \gamma_j) \boldsymbol{\sigma}_j^{L}(\boldsymbol{u}_j).\end{aligned} \tag{6.37}$$

Here, we drop the variable $\check{\rho}_j$ since its effect was already accounted for when calculating the stress constraints using either the TVC or the PVC. To ensure consistency with our implementation: (i) we utilize matrix notation to describe the stresses, and (ii) we do not square the interpolation factor, γ_j, which should be a linear function of the displacement.

The derivative Equation (6.37) w.r.t. displacement is

$$\begin{aligned}\frac{\partial \boldsymbol{\sigma}_j}{\partial \boldsymbol{u}_j} &= \left(\frac{\partial \boldsymbol{\sigma}_j^{NL}}{\partial(\gamma_j \boldsymbol{u}_j)} - \frac{\partial \boldsymbol{\sigma}_j^{L}}{\partial(\gamma_j \boldsymbol{u}_j)}\right)\frac{\partial(\gamma_j \boldsymbol{u}_j)}{\partial \boldsymbol{u}_j} + \frac{\partial \boldsymbol{\sigma}_j^{L}}{\partial \boldsymbol{u}_j} \\ &= \left(\frac{\partial \boldsymbol{\sigma}_j^{NL}}{\partial(\gamma_j \boldsymbol{u}_j)} - \frac{\partial \boldsymbol{\sigma}_j^{L}}{\partial(\gamma_j \boldsymbol{u}_j)}\right)\gamma_j + \frac{\partial \boldsymbol{\sigma}_j^{L}}{\partial \boldsymbol{u}_j},\end{aligned} \tag{6.38}$$

where

$$\frac{\partial \boldsymbol{\sigma}_j^{L}}{\partial(\gamma_j \boldsymbol{u}_j)} = \mathbf{D}^{SVK}\boldsymbol{B}_L, \quad \text{and} \tag{6.39}$$

$$\frac{\partial \boldsymbol{\sigma}_j^{L}}{\partial \boldsymbol{u}_j} = \mathbf{D}^{SVK}\boldsymbol{B}_L, \tag{6.40}$$

for $\mathbf{D}^{SVK}$ being the SVK elasticity matrix under small deformation theory, while $\boldsymbol{B}_L$ is the (linear) strain-displacement matrix (*vid.* e.g. Bathe, 2014).

The first term of Equation (6.38) is the most challenging of this study. Previous papers have looked into it. Both de Leon *et al.* (2015) and Große (2019) concentrated solely on two-dimensional analyses, and we found their notation is somewhat confusing – in a way that those formulations lack consistency in three-dimensional cases.

We know from Equation (2.21) that

$$\begin{aligned}\frac{\partial \boldsymbol{\sigma}_j^{NL}}{\partial(\gamma_j \boldsymbol{u}_j)} =& \frac{\partial J^{-1}}{\partial(\gamma_j \boldsymbol{u}_j)}\boldsymbol{F}_j \boldsymbol{S}_j \boldsymbol{F}_j^T + J^{-1}\frac{\partial \boldsymbol{F}_j}{(\gamma_j \boldsymbol{u}_j)}\boldsymbol{S}_j \boldsymbol{F}_j^T + \\ & J^{-1}\boldsymbol{F}_j \frac{\partial \boldsymbol{S}_j}{\partial(\gamma_j \boldsymbol{u}_j)}\boldsymbol{F}_j^T + J^{-1}\boldsymbol{F}_j \boldsymbol{S}_j \frac{\partial \boldsymbol{F}_j^T}{(\partial \gamma_j \boldsymbol{u}_j)}.\end{aligned} \tag{6.41}$$

But, transforming this result to be compatible with FE expressions is not straightforward. In the following, we will walk you through the process of determining $\partial \boldsymbol{\sigma}_j^{NL}/\partial(\gamma_j \boldsymbol{u}_j)$ – notice we want the nonlinear parcel of Cauchy stress vector. To accomplish this, we must first introduce partial derivatives necessary for its computation.

6.2.4.4 Computation of $\partial \mathbf{F}_j/\partial(\gamma_j \boldsymbol{u}_j)$

Since the deformation gradient tensor, $\boldsymbol{F}_j$, is unsymmetric, we must adapt our notation to one that is fully consistent. This is accomplished by converting $\boldsymbol{F}_j$

into

$$\mathsf{F}_j = \begin{bmatrix} F_{11} & F_{21} & F_{31} & F_{12} & F_{22} & F_{32} & F_{13} & F_{23} & F_{33} \end{bmatrix}^T = \begin{bmatrix} \mathsf{F}_1 & \mathsf{F}_2 & \mathsf{F}_3 & \dots & \mathsf{F}_8 & \mathsf{F}_9 \end{bmatrix}^T.$$

The displacement gradient, $\boldsymbol{G}_j$, also must be redefined. In light of this, we have

$$\mathsf{G}_j = \boldsymbol{B}_M \gamma_j \boldsymbol{u}_j, \tag{6.42}$$

where

$$\boldsymbol{B}_M = \begin{bmatrix} N_{1,1} & 0 & 0 & N_{2,1} & 0 & 0 & \cdots & N_{n,1} & 0 & 0 \\ 0 & N_{1,1} & 0 & 0 & N_{2,1} & 0 & \cdots & 0 & N_{n,1} & 0 \\ 0 & 0 & N_{1,1} & 0 & 0 & N_{2,1} & \cdots & 0 & 0 & N_{n,1} \\ N_{1,2} & 0 & 0 & N_{2,2} & 0 & 0 & \cdots & N_{n,2} & 0 & 0 \\ 0 & N_{1,2} & 0 & 0 & N_{2,2} & 0 & \cdots & 0 & N_{n,2} & 0 \\ 0 & 0 & N_{1,2} & 0 & 0 & N_{2,2} & \cdots & 0 & 0 & N_{n,2} \\ N_{1,3} & 0 & 0 & N_{2,3} & 0 & 0 & \cdots & N_{n,3} & 0 & 0 \\ 0 & N_{1,3} & 0 & 0 & N_{2,3} & 0 & \cdots & 0 & N_{n,3} & 0 \\ 0 & 0 & N_{1,3} & 0 & 0 & N_{2,3} & \cdots & 0 & 0 & N_{n,3} \end{bmatrix} \tag{6.43}$$

is the *modified strain-displacement transformation matrix*.

Equation (6.43) is designed for three-dimensional scenarios, although it may be readily adapted for two-dimensional applications. To do so, one should appropriately delete rows and columns containing $N_{a,3}$, resulting in a 4 x $2N_n$ matrix, for N_n being the number of nodes in the element.

The importance of Equation (6.42) stems from its simplicity in calculating the derivative. Afterwards, the deformation gradient vector, F_j, and its derivative w.r.t. $\gamma_j \boldsymbol{u}_j$ are

$$\mathsf{F}_j = \mathsf{G}_j + \mathsf{I} \quad \text{and} \tag{6.44}$$

$$\frac{\partial \mathsf{F}_j}{\partial(\gamma_j \boldsymbol{u}_j)} = \frac{\partial \mathsf{F}_j}{\partial(\gamma_j \boldsymbol{u}_j)} = \boldsymbol{B}_M, \tag{6.45}$$

where I is the column-wise stacked first-identity vector:

$$\mathsf{I} = \begin{cases} [1\ 0\ 0\ 0\ 1\ 0\ 0\ 0\ 1]^T, & \text{in 3D, or} \\ [1\ 0\ 0\ 1]^T, & \text{in 2D.} \end{cases}$$

In three-dimensional applications, Equation (6.45) is fully defined. Unfortunately, this is not true in two dimensions. Since $\boldsymbol{B}_M$ has only four rows, we need to alter $\partial \mathsf{F}_j / \partial(\gamma_j \boldsymbol{u}_j)$ for the remaining shear and out-of-plane components of F_j.

In this sense, we have

$$\frac{\partial \mathbf{F}_j}{\partial(\gamma_j \boldsymbol{u}_j)} = \begin{bmatrix} [B_M]_{1*} \\ [B_M]_{2*} \\ 0 \\ [B_M]_{3*} \\ [B_M]_{4*} \\ 0 \\ 0 \\ 0 \\ \dfrac{\partial \mathsf{F}_9}{\partial(\gamma_j \boldsymbol{u}_j)} \end{bmatrix}, \tag{6.46}$$

for $*$ denoting 'all columns', and

$$\frac{\partial \mathsf{F}_9}{\partial(\gamma_j \boldsymbol{u}_j)} = \frac{\partial F_{33}}{\partial(\gamma_j \boldsymbol{u}_j)} = \begin{cases} 0, & \text{in PE or} \\ \dfrac{\partial F_{33}}{\partial C_{33}} \dfrac{\partial C_{33}}{\partial(\gamma_j \boldsymbol{u}_j)} = \dfrac{1}{2F_{33}} \dfrac{\partial C_{33}}{\partial(\gamma_j \boldsymbol{u}_j)}, & \text{in PS.} \end{cases} \tag{6.47}$$

Next, we detailed explain how to calculate $\partial C_{33}/\partial(\gamma_j \boldsymbol{u}_j)$.

6.2.4.5 Computation of $\partial \mathbf{C}_j/\partial(\gamma_j \boldsymbol{u}_j)$

The right Cauchy-Green deformation vector given in terms of $\mathbf{F}_j$[12] is:

$$\mathbf{C}_j = \begin{cases} \begin{bmatrix} \mathsf{F}_1^2 + \mathsf{F}_2^2 + \mathsf{F}_3^2 \\ \mathsf{F}_4^2 + \mathsf{F}_5^2 + \mathsf{F}_6^2 \\ \mathsf{F}_7^2 + \mathsf{F}_8^2 + \mathsf{F}_9^2 \\ \mathsf{F}_1\mathsf{F}_4 + \mathsf{F}_2\mathsf{F}_5 + \mathsf{F}_3\mathsf{F}_6 \\ \mathsf{F}_4\mathsf{F}_7 + \mathsf{F}_5\mathsf{F}_8 + \mathsf{F}_6\mathsf{F}_9 \\ \mathsf{F}_1\mathsf{F}_7 + \mathsf{F}_2\mathsf{F}_8 + \mathsf{F}_3\mathsf{F}_9 \end{bmatrix}, & \text{in 3D, or} \\ \begin{bmatrix} \mathsf{F}_1^2 + \mathsf{F}_2^2 \\ \mathsf{F}_4^2 + \mathsf{F}_5^2 \\ \mathsf{F}_9^2 \\ \mathsf{F}_1\mathsf{F}_4 + \mathsf{F}_2\mathsf{F}_5 \\ 0 \\ 0 \end{bmatrix}, & \text{in 2D,} \end{cases} \tag{6.48}$$

[12]For clarification, we first compute $\boldsymbol{C}_j = \boldsymbol{F}_j^T \boldsymbol{F}_j$, and then we reassemble the outcome as a vector.

where

$$\mathsf{F}_9 = \begin{cases} 1, & \text{in PE, or} \\ \text{unknown}, & \text{in PS.} \end{cases}$$

Its derivative is given by

$$\frac{\partial \mathbf{C}_j}{\partial(\gamma_j \boldsymbol{u}_j)} = \begin{bmatrix} \sum_i 2\mathsf{F}_i \dfrac{\partial \mathsf{F}_i}{(\gamma_j \boldsymbol{u}_j)}, & \text{for } i = 1,2,3 \\ \sum_i 2\mathsf{F}_i \dfrac{\partial \mathsf{F}_i}{(\gamma_j \boldsymbol{u}_j)}, & \text{for } i = 4,5,6 \\ \sum_i 2\mathsf{F}_i \dfrac{\partial \mathsf{F}_i}{(\gamma_j \boldsymbol{u}_j)}, & \text{for } i = 7,8,9 \\ \sum_i 2\left(\mathsf{F}_i \dfrac{\partial \mathsf{F}_{i+3}}{(\gamma_j \boldsymbol{u}_j)} + \mathsf{F}_{i+3} \dfrac{\partial \mathsf{F}_i}{(\gamma_j \boldsymbol{u}_j)}\right), & \text{for } i = 1,2,3 \\ \sum_i 2\left(\mathsf{F}_i \dfrac{\partial \mathsf{F}_{i+3}}{(\gamma_j \boldsymbol{u}_j)} + \mathsf{F}_{i+3} \dfrac{\partial \mathsf{F}_i}{(\gamma_j \boldsymbol{u}_j)}\right), & \text{for } i = 4,5,6 \\ \sum_i 2\left(\mathsf{F}_i \dfrac{\partial \mathsf{F}_{i+6}}{(\gamma_j \boldsymbol{u}_j)} + \mathsf{F}_{i+6} \dfrac{\partial \mathsf{F}_i}{(\gamma_j \boldsymbol{u}_j)}\right), & \text{for } i = 1,2,3 \end{bmatrix}, \tag{6.49}$$

in which: (i) each $\partial \mathsf{F}_i/(\gamma_j \boldsymbol{u}_j)$ corresponds to the i-th row of $[B_{NL}]$, and (ii) the factor 2 in the last three rows is required for compatibility with engineering stresses.

In two-dimensional analysis, there are two possibilities: plane strain, where the third, fifth, and last rows of $\partial \mathbf{C}_j/(\gamma_j \boldsymbol{u}_j)$ are necessary null, and plane stress, where only the last two rows are zeros – requiring a separate computation of $\partial C_{33}/\partial(\gamma_j \boldsymbol{u}_j)$. In these situations, we wish to find the value of C_{33} such that

$$\sigma_{33}(\mathbf{C}j(C_{33}), C_{33}) = 0.$$

Nevertheless, for the material models of this dissertation, we observe that $\sigma_{33} = 0 \iff S_{33} = 0$. Then, it is enough to ensure that

$$S_{33}(\mathbf{C}_j(C_{33}), C_{33}) = 0,$$

whose derivative w.r.t. $\gamma_j \boldsymbol{u}_j$ is

$$\underbrace{\frac{\partial S_{33}}{\partial \mathbf{C}_j}}_{\mathsf{D}_{3*}} \frac{\partial \mathbf{C}_j}{\partial(\gamma_j \boldsymbol{u}_j)} + \underbrace{\frac{\partial S_{33}}{\partial C_{33}}}_{\mathsf{D}_{33}} \frac{\partial C_{33}}{\partial(\gamma_j \boldsymbol{u}_j)} = 0.$$

Thus, after reassembling, we found that

$$\frac{\partial C_{33}}{\partial(\gamma_j \boldsymbol{u}_j)} = -\frac{1}{\mathsf{D}_{33}} \mathsf{D}_{3*} \frac{\partial \mathbf{C}_j}{\partial(\gamma_j \boldsymbol{u}_j)}, \tag{6.50}$$

where $\partial \mathbf{C}_j / \partial(\gamma_j \boldsymbol{u}_j)$ is calculated from Equation (6.49) with $\mathsf{F}_9 = 1$. Alternatively, D_{33} and D_{3*} are derived from the real value of C_{33}, as in the case of Section 2.5, using Newton's approach.

6.2.4.6
Computation of $\partial J^{-1} / \partial(\gamma_j \boldsymbol{u}_j)$

The derivative of the Jacobian, J, w.r.t. $\gamma_j \boldsymbol{u}_j$ is

$$\frac{\partial J}{\partial(\gamma_j \boldsymbol{u}_j)} = \frac{\partial J}{\partial \boldsymbol{F}_j} \frac{\partial \mathbf{F}_j}{\partial(\gamma_j \boldsymbol{u}_j)} = J \mathbf{F}_j^{-T} \frac{\partial \mathbf{F}_j}{\partial(\gamma_j \boldsymbol{u}_j)}, \tag{6.51}$$

where $\partial \mathbf{F}_j / \partial(\gamma_j \boldsymbol{u}_j)$ was previously discussed in Sections 6.2.4.4 and 6.2.4.5. For clarification, we first compute $\partial J / \partial \boldsymbol{F}_j$ – easily found in continuum mechanics references (e.g. Hackett, 2016) – then we convert its result to matrix notation, following the same approach of Section 6.2.4.4.

Therefore, we obtain

$$\frac{\partial J^{-1}}{\partial(\gamma_j \boldsymbol{u}_j)} = \underbrace{\frac{\partial J^{-1}}{\partial J}}_{-1/J^2} \frac{\partial J}{\partial(\gamma_j \boldsymbol{u}_j)} = -\frac{1}{J} \mathbf{F}_j^{-T} \frac{\partial \boldsymbol{F}_j}{\partial(\gamma_j \boldsymbol{u}_j)}. \tag{6.52}$$

6.2.4.7
Computation of $\partial \mathbf{S}_j / \partial(\gamma_j \boldsymbol{u}_j)$

This term is computed as

$$\frac{\partial \mathbf{S}_j}{\partial(\gamma_j \boldsymbol{u}_j)} = \underbrace{\frac{\partial \mathbf{S}_j}{\partial \mathbf{E}_j}}_{\mathbf{D}_j} \underbrace{\frac{\partial \mathbf{E}_j}{\partial \mathbf{C}_j}}_{2} \frac{\partial \mathbf{C}_j}{\partial(\gamma_j \boldsymbol{u}_j)} = 2 \mathbf{D}_j \frac{\partial \mathbf{C}_j}{\partial(\gamma_j \boldsymbol{u}_j)}. \tag{6.53}$$

See Section 6.2.4.5 for further information on $\partial \mathbf{C}_j / \partial(\gamma_j \boldsymbol{u}_j)$.

6.2.4.8
Computation of $\partial \boldsymbol{\sigma}_j^{NL} / \partial(\gamma_j \boldsymbol{u}_j)$

Instead of dealing with Equation (6.41), it is easier to compute

$$\frac{\partial \boldsymbol{\sigma}_j^{NL}}{\partial(\gamma_j \boldsymbol{u}_j)} = \frac{\partial J^{-1}}{\partial(\gamma_j \boldsymbol{u}_j)} \mathbf{F}_j \mathbf{S}_j \mathbf{F}_j^T + J^{-1} \frac{\partial(\mathbf{F}_j \mathbf{S}_j \mathbf{F}_j^T)}{\partial(\gamma_j \boldsymbol{u}_j)}, \tag{6.54}$$

with

$$\frac{\partial(\mathbf{F}_j \mathbf{S}_j \mathbf{F}_j^T)}{\partial(\gamma_j \boldsymbol{u}_j)} = \frac{\partial(\mathbf{F}_j \mathbf{S}_j \mathbf{F}_j^T)}{\partial \mathbf{F}_j} \frac{\partial \mathbf{F}_j}{\partial(\gamma_j \boldsymbol{u}_j)} + \frac{\partial(\mathbf{F}_j \mathbf{S}_j \mathbf{F}_j^T)}{\partial \mathbf{S}_j} \frac{\partial \mathbf{S}_j}{\partial(\gamma_j \boldsymbol{u}_j)}. \tag{6.55}$$

This approach provides a significant advantage: we can compute $\boldsymbol{F}_j \boldsymbol{S}_j \boldsymbol{F}_j^T$ separately, convert the result into a vector, and differentiate it w.r.t. both $\mathbf{F}_j$

and $\mathbf{S}_j$. Since all the terms differentiated w.r.t. $\gamma_j \boldsymbol{u}_j$ are known, we finally reach $\partial \boldsymbol{\sigma}_j^{NL} / \partial(\gamma_j \boldsymbol{u}_j)$.

6.2.4.9 Computation of $\partial g_j^+ / \partial \check{\rho}_e$

The derivative of $\partial g_j^+ / \partial \check{\rho}_e$ is unraveled as

$$\frac{\partial g_j^+}{\partial \check{\rho}_e} = \frac{\partial g_j^+}{\partial \check{\rho}_e}\Big|_{\gamma_j \boldsymbol{u}_j \text{ fix}} + \frac{\partial g_j^+}{\partial \sigma_j^{vM}} \frac{\partial \sigma_j^{vM}}{\partial \boldsymbol{\sigma}_j} \frac{\partial \boldsymbol{\sigma}_j}{\partial(\gamma_j \boldsymbol{u}_j)} \frac{\partial(\gamma_j \boldsymbol{u}_j)}{\partial \gamma_j} \frac{\partial \gamma_j}{\partial \check{\rho}_e}, \tag{6.56}$$

which takes into account the implicit dependency on γ_j and $\boldsymbol{u}_j$, as detached in Section 6.2.2.

Then,

$$\frac{\partial g_j^+}{\partial \check{\rho}_e}\Big|_{\gamma_j \boldsymbol{u}_j \text{ fix}} = \begin{cases} g_j^+, & \text{in TVC, or} \\ (g_j^+)^3 + \hat{c}_j^+, & \text{in PVC.} \end{cases} \tag{6.57}$$

According to Equation (6.38),

$$\frac{\partial \boldsymbol{\sigma}_j}{\partial(\gamma_j \boldsymbol{u}_j)} = \begin{cases} 0, & \text{if } g_j^+ < -\mu_j/\varphi, \text{ or} \\ \dfrac{\partial \boldsymbol{\sigma}_j^{NL}}{\partial(\gamma_j \boldsymbol{u}_j)} - \dfrac{\partial \boldsymbol{\sigma}_j^{L}}{\partial(\gamma_j \boldsymbol{u}_j)}, & \text{otherwise.} \end{cases} \tag{6.58}$$

Note we employ the Voigt notation again for the Cauchy stress.

Finally, the last two terms in Equation (6.56) are

$$\frac{\partial(\gamma_j \boldsymbol{u}_j)}{\partial \gamma_j} = \boldsymbol{u}_j, \tag{6.59}$$

and

$$\frac{\partial \gamma_j}{\partial \check{\rho}_e} = \frac{-\beta_1(\tanh^2(\beta_1(\eta_1 - \check{\rho}_e)) - 1)}{\tanh(\beta_1 \eta_1) - \tanh(\beta_1(\eta_1 - 1))}. \tag{6.60}$$

6.2.4.10 Computation of $\partial \boldsymbol{f}_{intj} / \partial \check{\rho}_e$

The internal force derivative in Equation (6.11) is simply

$$\frac{\partial \boldsymbol{f}_{intj}}{\partial \check{\rho}_e} = \gamma_j \boldsymbol{f}_{intj}^{NL} + (1 - \gamma_j^2) \boldsymbol{f}_{intj}^{L}. \tag{6.61}$$

6.2.4.11 Sensitivity Verification

To check our sensitivity analysis, we investigate the beam of Figure 6.7. In this example, we use the SVK model, plane stress state, and assume a linear material distribution in the range of $0.01 \leqslant z_e \leqslant 1$. The design domain then is divided in 10 elements: 5 along the width and 2 along the height.

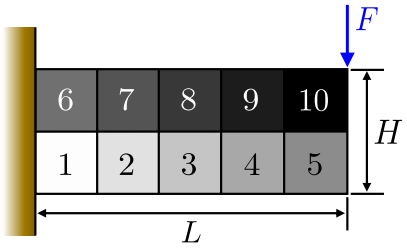

Load & Geometry:	Optimization Data:
$F = 10$	PVC with SIMP for $p = 3$
$L = 50$	Filter: $R = 0, s = 1$
$H = 20$	ALM: $\mu_j^{(0)} = 0, \varphi^{(0)} = 10, \phi = 1.1$
$t = 1$	
Material Properties:	Data for LCM:
$E_0 = 3,000$	Step factor: $\overline{\Delta\lambda}_s = 1$
$\nu_0 = 0.4$	Max. iter. per step = 50
$\sigma_{lim} = 50$	

Figure 6.7: Cantilever beam to validate the sensitivity analysis (consistent units applied).

We found that employing the convergence criterion

$$||d\boldsymbol{u}|| \leqslant 10^{-6} \tag{6.62}$$

leads to fewer iterations in the LCM – so, we adopted it in this validation. For the energy interpolation scheme we assumed $\beta_1 = 10$ and $\rho_1 = 0.009$, which we found preferable to validate intermediate design variable values.

Assume the function $f(x)$. Its derivative can be approximated by the central finite difference method as

$$\frac{\mathrm{d}f}{\mathrm{d}x} \approx \frac{f(x + \Delta x) - f(x - \Delta x)}{2\Delta x}, \tag{6.63}$$

where Δx is a small perturbation on x.

We observed that the smallest relative error associated with each design variable does not necessarily occur for the same perturbation value adopted in the finite differentiation. Nevertheless, we found that a perturbation of 10^{-4} provides satisfactory results, as shown in Table 6.1.

El. #	Analytical Procedure	Central Finite Difference	Relative Error
1	0.18721...	0.18721...	4.4917×10^{-8}
2	0.0010559...	0.0010559...	4.7797×10^{-9}

Continued on next page

El. #	Analytical Procedure	Central Finite Difference	Relative Error
3	$2.2102\ldots\times10^{-4}$	$2.2102\ldots\times10^{-4}$	8.1986×10^{-9}
4	$-5.7076\ldots\times10^{-7}$	$-5.7075\ldots\times10^{-7}$	1.2461×10^{-6}
5	$-2.2278\ldots\times10^{-5}$	$-2.2278\ldots\times10^{-5}$	9.7886×10^{-9}
6	$-3.9915\ldots\times10^{-5}$	$-3.9915\ldots\times10^{-5}$	5.9555×10^{-9}
7	$-6.5542\ldots\times10^{-5}$	$-6.5542\ldots\times10^{-5}$	1.1668×10^{-9}
8	$-2.0768\ldots\times10^{-5}$	$-2.0768\ldots\times10^{-5}$	9.1603×10^{-10}
9	$-2.4049\ldots\times10^{-6}$	$-2.4049\ldots\times10^{-6}$	1.1638×10^{-8}
10	$-5.7309\ldots\times10^{-8}$	$-5.7309\ldots\times10^{-8}$	2.2839×10^{-7}

Table 6.1: Sensitivity validation.

7
Results

"Nothing is impossible, the word itself says 'I'm possible'."

Hepburn-Ruston, A.K. (1929–1993)

This chapter will showcase the outcomes of minimizing the weight subjected to stress constraints in situations involving geometrical and/or material non-linearities, as established in Problem (6.1).

The augmented Lagrangian function of Section 5.2.3 is applied to handle the high number of constraints with $\mu_j^{(0)} = 0, \varphi^{(0)} = 10, \phi = 1.1$ and $\varphi_{max} = 10^7$; the PVC (Giraldo-Londoño & Paulino, 2021) is evoked to treat the stress singularity; and the linear density filtering scheme of Section 4.1.1.1 is used to smooth the stress field. We choose the EIS of Section 6.2.2 to tackle possible numerical instabilities in low-stiffness components within the design domain.

The studies herein employed the unconstrained version of MMA (Giraldo-Londoño & Paulino, 2021), whose parameters are identified in Table 7.1. The adjusted optimization data are detached in Table 7.2.

Variable	Description	Value
a_0	Initial asymptotes	0.2
a_{inc}	Asymptotes increment	1.2
a_{dec}	Asymptotes decrement	0.7
$Move$	Allowable move step	0.1

Table 7.1: MMA parameters.

Here, we let the sharpness variable of the tanh function – Equation (4.3) – constant in the first 20 iterations to stabilize the material distribution. From this point forward, β is incremented in the form of $\beta^{(i+1)} = \beta^{(i)} + \Delta\beta$ every 10 iterations.

Variable	Description	Value
$z_e^{(0)}$	Initial material distribution	1
s	Filter exponent	1
p	SIMP exponent	3.5
n_{MMA}	Number of MMA iterations	5
n_{it}	Number of total iterations	750
τ_ρ	Design variable tolerance	0.001
τ_σ	Stress tolerance	0.001
$\beta^{(0)}$	Projection parameter initial value	2
β_f	Projection parameter update frequency iterations	10
β_{max}	Projection parameter maximum value	12
$\Delta\beta$	Projection parameter increment	2

Table 7.2: Optimization parameters.

The optimization procedure converges when both

$$\frac{1}{N_e}\sum_{e=1}^{N_e}(z_e^{(i+1)} - z_e^{(i)}) \leqslant \tau_\rho, \quad \text{and} \tag{7.1}$$

$$\frac{\max\{\sigma^{vM,(i)}\}}{\sigma_{lim}} - 1 \leqslant \tau_\sigma, \tag{7.2}$$

whatever β reaches its maximum value, β_{max}, or not.

Regarding the LCM, we considered a prescribed load factor $\overline{\Delta\lambda}_s = 0.1$ – unless indicated otherwise –, with a maximum of 50 iterations per step, and the incremental-iterative procedure converges when Equation (6.62) is satisfied.

Figure 7.1 detaches a representative fluxogram that summarizes the key points of our implementation. Here, we consider a bisection approach in situations where the LCM failed to converge. Then, this method divides the load factor up to a maximum of five bisections. In case of convergence, the optimization process proceeds; otherwise, the analysis is stopped altogether and an error message appears at the end of the optimization.

This chapter's simulations were all performed in Matlab R2022a on a desktop computer equipped with 64 GB RAM and an Intel(R) Core(TM) i9-7920X CPU @ 2.90 GHz with NVIDIA GeForce GT 710 and 1.00 GB of RAM. We developed our codes based on the `PolyMesher` (Talischi *et al.*, 2012) and `PolyStress` (Giraldo-Londoño & Paulino, 2020). This allowed us greater freedom and control over the methods employed and was also crucial to implementing the EIS in the way we did.

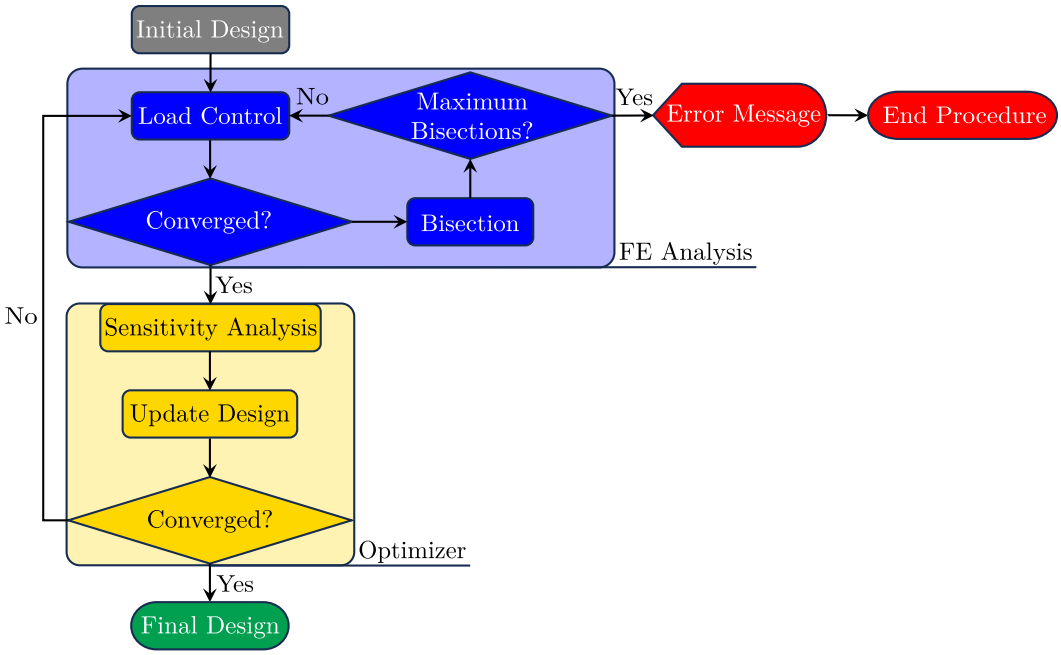

Figure 7.1: Optimization fluxogram.

The examples are based on real material properties for different geometries and loading conditions under plane strain (PE) or plane stress (PS) hypotheses. Key results will include comparing the optimized designs under small vs. large deformations and the impact of nonlinearities on the final topology.

7.1 U-Shape

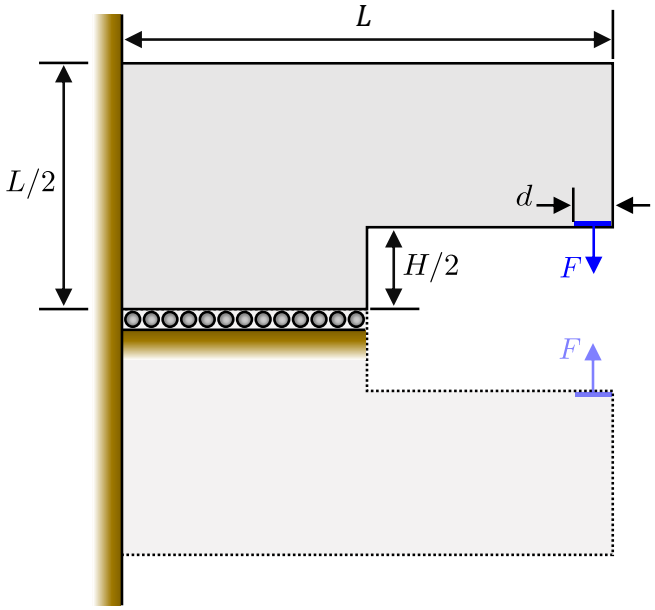

Load & Geometry:
$F = 400$ kN
$L = 1,500$ mm
$H = 500$ mm
$t = 100$ mm
$d = 75$ mm

Material Properties:
$E_0 = 5$ GPa
$\nu_0 = 0.38$
$\sigma_{lim} = 100$ MPa

Optimization Data:
$R = 40$ mmn

Figure 7.2: U-shape.

Consider the U-shape in Figure 7.2. It is made of a PEEK

(PolyEtherEtherKetone) plastic (MatWeb, 2024c), and modeled by 9,375 quadrilateral elements with linear behavior (Q4). The force is evenly distributed in the nodes of the region d, and due to the symmetry conditions (on the horizontal plane), we only model the upper part of the design domain.

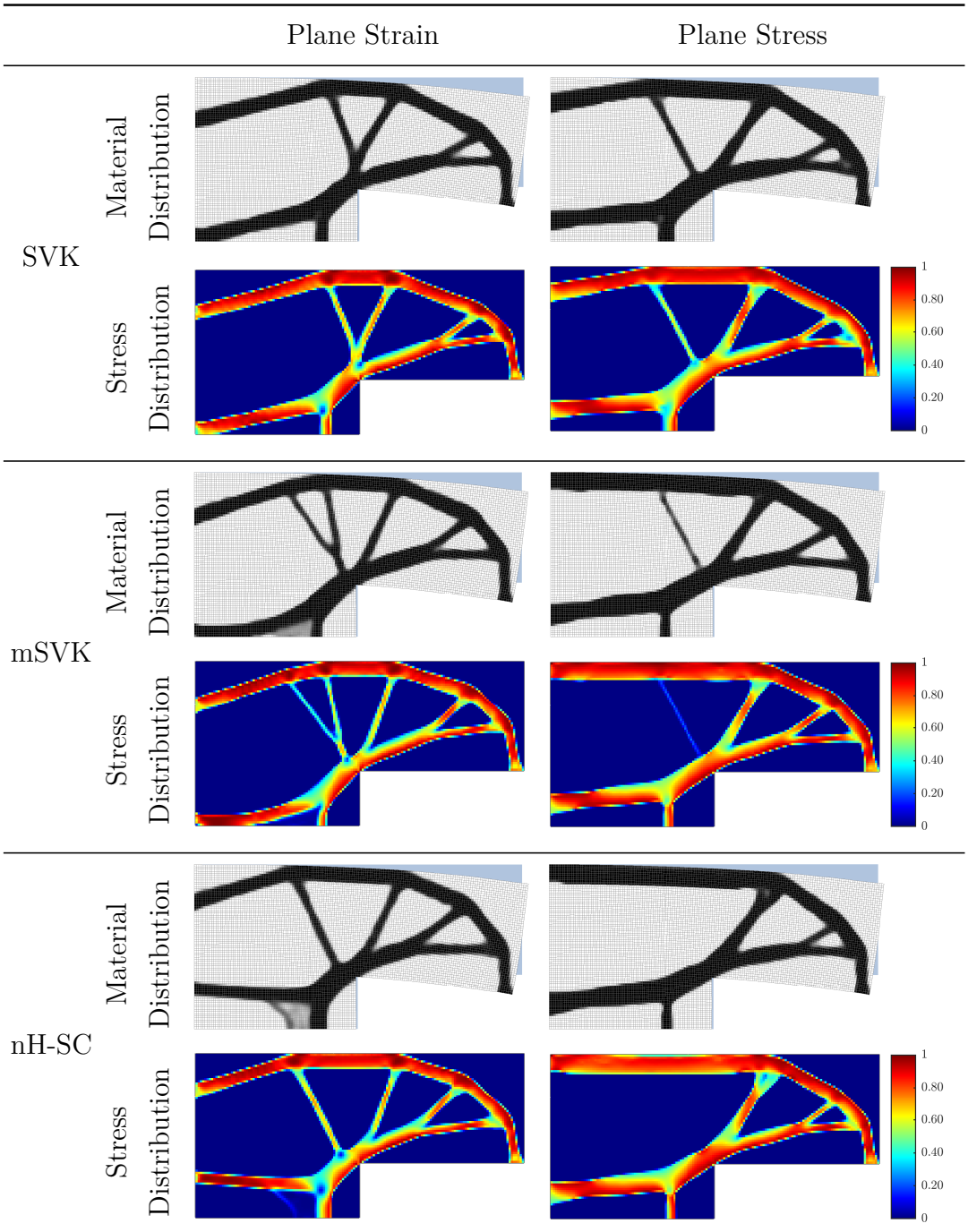

Figure 7.3: U-shape material and stress distributions considering different material models in plane strain or plane stress.

For academic reasons, we compare the outcomes of different material models in PE and PS states. This is carried out in Figure 7.3 for SVK, mSVK, and nH-SC models defined in Section 2.4.3. The PE responses for mSVK and

nH models struggled to find proper material distribution near the right inner corner. This is because, in the PE state, the initial stress levels are lower than those in PS – *vid.* Figure 7.4 – and the solver converges faster for a rough layout. We can likely improve the quality of these results by altering the continuation scheme for β in Equation (4.3). Yet, we would not be able to establish an effective set of parameters capable of solving the following examples.

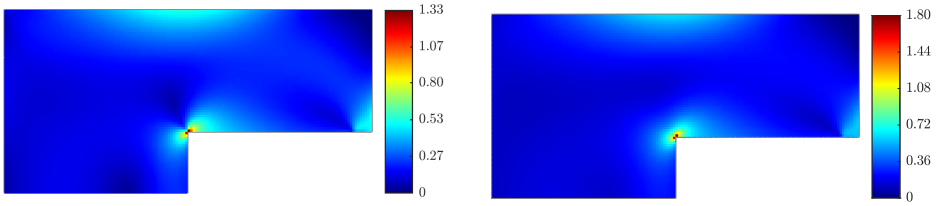

(a) (b)

Figure 7.4: Initial stress distribution in the SVK model in (a) plane strain and (b) plane stress.

Table 7.3 displays indicators for the above optimizations. PE-driven solutions are generally stiffer than their PS counterparts due to the out-of-plane restriction. The increased stiffness of PE can lead to large in-plane stress concentrations, hence, conducting a large number of active elements in comparison to the PS state. In the same way, we find lesser masses in PE due to the material's inversely proportional relationship to stress. Moreover, the higher computing time required by the mSVK model in PS is owing to: (i) the effort applied to solve a nonlinear equation to get C_{33} (*vid.* Section 2.5), and (ii) the large number of iterations computed in the LCM. For the last, we observed it was caused by sudden density reductions in the vicinity of the less stressed inclined bar, culminating in large distortions.

Determining which option is superior to another is subjective. For instance, the SVK-like solutions satisfied the constraints. But, solving topology optimization with nonlinearities using the SVK material model may be difficult due to its well-known limitation in large compressions. Conversely, the nH-SC model in PS was, by far, the one with the most well-defined geometry, and both mSVK-like optimizations required a longer time to finish.

The literature, especially for nonlinear problems, often presents beam-type solutions in PE scenarios. Thus, to understand the feasibility of this procedure, we examine in Figure 7.5 how the U-shape-optimized topologies behave when subjected to a nonlinear FE routine in the opposite state. We found that in both cases, the solutions overestimate the peak stress by about 20%. This highlights how crucial it is to assume the proper state while optimizing for stress constraints.

Material Model	Plane Strain			Plane Stress		
	SVK	mSVK	nH-SC	SVK	mSVK	nH-SC
M_{nd} (%)	7.64	9.26	10.41	7.56	7.07	6.32
Mass (%)	28.60	28.98	29.22	32.00	30.84	30.99
$\max\{\sigma_e^{vM}(\boldsymbol{z})\}/\sigma_{lim}$ - 1	-0.0013	-0.0006	0.0007	-0.006	0.0003	-0.009
Active Elements (%)	22.40	24.02	27.03	21.22	22.34	20.56
Number of Iterations	330	335	299	337	322	323
Time	4.7 h	4.8 h	4.2 h	4.6 h	21.5 h†	4.6 h

† The higher computation time is a result of the numerical evaluation of C_{33} and a large number of iterations in the LCM.

Table 7.3: Solution parameters for U-shape.

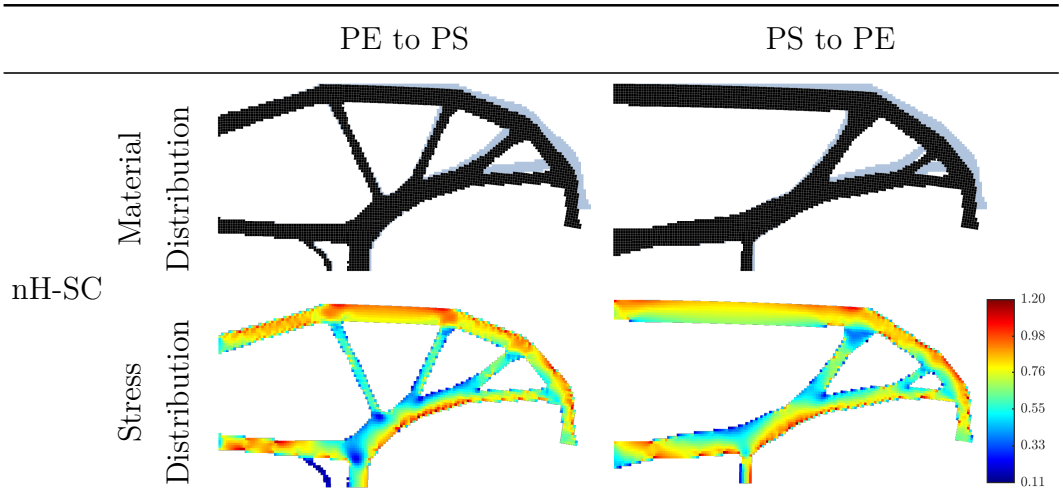

Figure 7.5: U-shape submitted to nonlinear FE routine with opposite states.

7.2 Cantilever Beam

The cantilever beam is a well-known standard example in the topology optimization of nonlinear structures (e.g. Bruns & Tortorelli, 1998; Buhl *et al.*, 2000; Lahuerta *et al.*, 2013). Here, though, we uniformly distributed the load at region d, as defined in Figure 7.6, to avoid stress concentrations. The material properties referred to a Nylon 610 (MatWeb, 2024b).

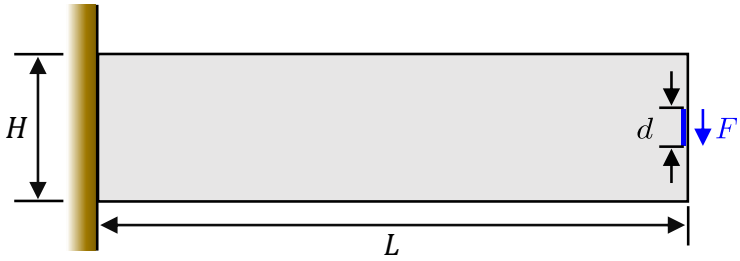

Load & Geometry:	Material Properties:	Optimization Data:
$F = 100$ kN	$E_0 = 3$ GPa	$R = 20$ mm
$L = 1,000$ mm	$\nu_0 = 0.4$	
$H = 250$ mm	$\sigma_{lim} = 100$ MPa	
$t = 100$ mm		
$d = 12.5$ mm		

Figure 7.6: Cantilever beam.

We tested several sets of parameters for the MMA and the optimization itself, but we could not achieve convergence in the nonlinear case using the SVK model. So, we assume an nH-SC material and compare solutions in PE, which is often solved in compliance-centric formulations.

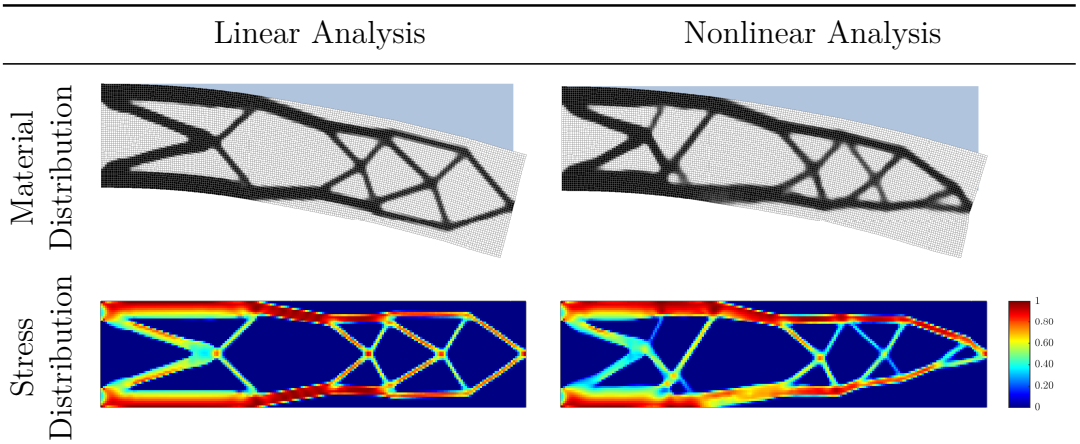

Figure 7.7: Cantilever beam material and stress distributions for linear and nonlinear analyses.

Figure 7.7 shows the results produced by linear and nonlinear FE routines for a mesh discretized by 200 x 50 quadrilaterals. As predicted, the layout from the linear analysis is symmetric along the longitudinal axis, whereas the design attained using nonlinear FE is not.

Surprisingly, in both scenarios, the material distribution was forced towards the domain's interior as we moved away from the clamped locality. Given that we are dealing with stress constraints, this tendency seems coherent as it raises the stress in the top and bottom of the design domain.

According to Table 7.4, both analyses provide similar parameters. The most outstanding distinction is the quantity of active elements. In comparison to the nonlinear solution, the linear analysis response provided more than 1.4 times as many active components. Regarding the optimized mass, it makes sense the linear solution has a lower value. In general, the linear solution's layout shifts a bit more than that of the nonlinear equivalent. This slight modification increased the deformations and, in turn, the stresses, suggesting additional material removal and contributing to the impression that the linear approach is accurate.

	Linear Analysis	Nonlinear Analysis
M_{nd} (%)	12.20	14.88
Mass (%)	34.66	39.95
$\max\{\sigma_e^{vM}(\boldsymbol{z})\}/\sigma_{lim}$ - 1	0.0009	0.0009
Active Elements (%)	29.97	21.26
Number of Iterations	350	296
Time	1.6 min	8.0 h

Table 7.4: Solution parameters for cantilever beam.

It is reasonable to check the linear analysis solution. Then, we submitted the optimized topology to a nonlinear FE routine; for convenience, we assumed the nH-SC model. This resulted in the response illustrated in Figure 7.8, where the high level of deformation is visible in Figure 7.8(a), especially at the bottom half of the design domain due to a bar under buckling. As a consequence, several points of Figure 7.8(b) exhibited significant violations in the stress value. This outcome provides irrefutable evidence that addressing topology optimization problems of large deformations through linear analysis is definitely not the best course of action – in reality, it is an extremely discouraging approach.

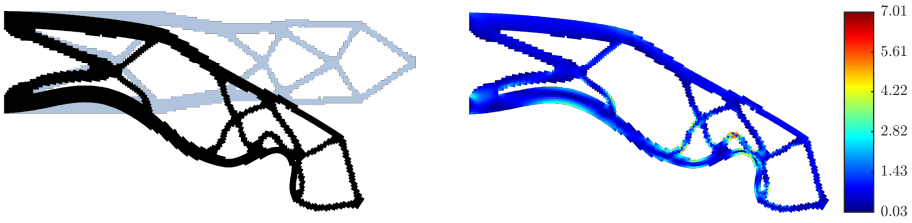

(a) (b)

Figure 7.8: Cantilever linear-optimized layout submitted to nonlinear analysis: (a) material distribution, and (b) stress distribution at deformed configuration.

Even though the responses of Figure 7.8 are crude – as the true behavior would only become apparent after interpreting the optimized layout – they provide us with a good insight into the extent to which linear analysis may overstate the stress levels.

7.3 Crack Notch Beam

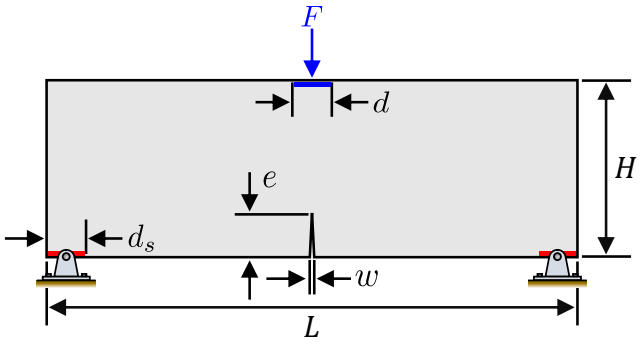

Load & Geometry:	Material Properties:
$F = 12$ kN	$E_0 = 3$ GPa
$L = 360$ mm	$\nu_0 = 0.3$
$H = 120$ mm	$\sigma_{lim} = 90$ MPa
$t = 10$ mm	
$d = d_s = 12$ mm	
$e = 30$ mm	Optimization Data:
$w = 3$ mm	$R = 8$ mm

Figure 7.9: Crack notch beam.

The crack notch beam shown in Figure 7.9, possesses material properties of a Nylon 6-3 (MatWeb, 2024a) and is divided into 20,000 polygons. Once more, the load was split evenly across the nodes of the region d, whereas the supports – which the movement is restricted in both directions – were uniformly dispersed among the nodes of line segment d_s. Particularly here, we

used a prescribed load factor $\overline{\Delta\lambda}_s = 0.2$ to speed up the optimization procedure without jeopardizing the convergence.

We study the responses for both linear and nonlinear analyses, where, in the nonlinear case, we assumed the nH-SC model. Figure 7.10 illustrates the noticeable difference between them: for the large deformation theory layout, the notch vicinity featured stress concentrations, whereas the formed bars were thicker and showed lower stress levels. Conversely, the linear-like variant formed thinner bars with greater stress; nevertheless, the stresses were evenly distributed in the notch vicinity, reducing their level in the horizontal bar.

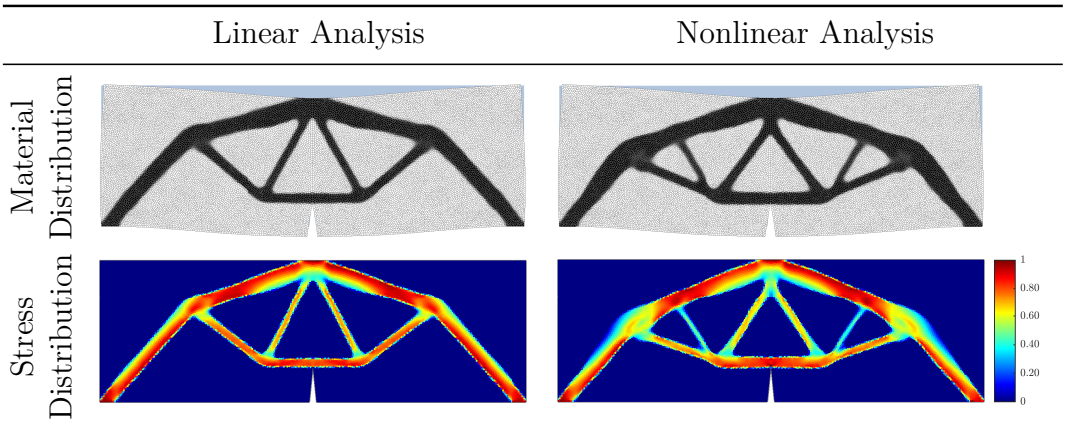

Figure 7.10: Crack notch beam material and stress distributions for linear and nonlinear analyses.

Although the main parameters listed in Table 7.5 seemed better for the small deformation theory, caution is still essential. The nonlinear analysis design is heavier due to the large induced displacements that prompted the addition of material to withstand them. On the other hand, its percentage of active elements is smaller because the stresses are dispersed across the thicker bars.

	Linear Analysis	Nonlinear Analysis
M_{nd} (%)	6.03	6.70
Mass (%)	21.21	25.21
$\max\{\sigma_e^{vM}(\boldsymbol{z})\}/\sigma_{lim}$ - 1	-0.0028	0.0009
Active Elements (%)	13.78	10.58
Number of Iterations	355	392
Time	14.1 min	1.9 days

Table 7.5: Solution parameters for crack notch beam.

To investigate the feasibility of the linear analysis solution, we submitted it into the nonlinear FE routine. To improve resistance in compression, we considered the nH-SC model, which resulted in the layout of Figure 7.11(a). So, from Figure 7.11(b) we observe that this layout will fail. If we consider σ_{lim} as the yield limit, then, the linear-like solution will yield under large deformations.

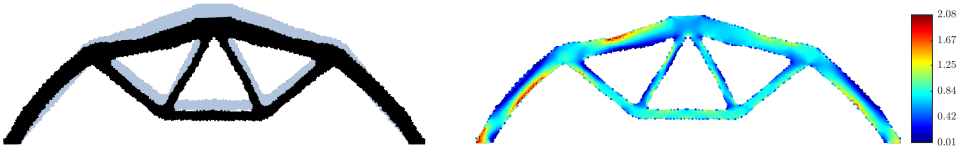

(a) (b)

Figure 7.11: Crack notch beam linear-optimized layout submitted to nonlinear analysis: (a) material distribution, and (b) stress distribution at deformed configuration.

8
Conclusions

"The possession of knowledge does not kill the sense of wonder and mystery. There is always more mystery."

Nin, A. (1903–1977)

In this dissertation, we tackled the topology optimization problem of minimizing mass with stress constraints under geometrical and material nonlinearities. The material nonlinearity was modeled via hyperelastic theory. To complete this task, we rely on our `HyperSym` tool, which is of great help since it simplifies the computation of PK2 stress and constitutive tensors.

We focused on three material models: SVK, mSVK, and nH-SC. Additionally, we solved problems in plane strain and plane stress. For the first, we can easily ascertain the quantities required by the FE implementation. For the latter, we must find the out-of-plane strain component, C_{33}, that nullifies the Cauchy stress in that direction. We developed analytical expressions to evaluate C_{33} for the SVK and nH-SC models; on the other hand, we had to iteratively solve a nonlinear equation for the mSVK model, where we resorted to Newton's method.

Stress constraints impose several difficulties on density-driven topology optimization. The two most commonly recognized are the 'singularity' phenomenon and the many stress constraints. Concerning the first issue, we evoked the polynomial vanishing constraints. About the second one, we conducted a comprehensive review and investigated a study on the L-bracket. Afterward, we conclude that the augmented Lagrangian method is more efficient and robust than aggregation or regionalization approaches since ALM was prone to mass reduction and increased active elements.

As we consider constant meshes, significant displacements might introduce numerical instabilities in quasi-voids, potentially leading to severely deformed elements with non-positive Jacobian. Thereby, we managed a simple comparison for the C-shape and concluded that the energy interpolation approach is the most suitable option for alleviating these distortions – yet, there is no guarantee that it will work always!

MMA requires derivatives of the augmented Lagrangian function. Then, we carried out a step-by-step sensitivity study that took into account both two- and three-dimensional possibilities. In the end, we validated the derivatives in a cantilever beam and found that our analytical implementation and the solution approximated by central finite differences agreed quite well.

It is well-known that minimizing compliance with material constraints for the aforementioned sources of nonlinearities has a significant effect on the achieved layouts. In our case, there is no distinction. The significance of these nonlinearities is far more important: through the cantilever and the crack notch beam examples, we have shown that the linear analysis-based solutions overestimated the allowable stress when subjected to large deformations.

The U-shape example, in turn, demonstrated the impact of considering various material models in plane strain and plane stress scenarios. The plane strain responses showed a concentration of grays in the bottom right corner, which further illustrates how difficult it may be to find a set of parameters to result in well-defined designs.

Finally, we point out the duality between stress and large strains. Upon increasing a given force F to $F + \Delta F$, we shall naturally induce greater initial stress distribution. As a consequence, the solver will add more material within the design domain, lowering the quantity of low-stiffness elements and, thus, reducing the likelihood of numerical instabilities arising.

8.1 Suggestions for Future Works

As is customary, we used the Total Lagrangian formulation for the FE implementation; however, the Updated Lagrangian formulation might also be investigated.

Throughout our optimization analyses, we did experience issues working with a fixed value of the cutoff parameter, η_1, when submitting the linear analysis-based solution to large deformations. Zhang *et al.* (2018) faced comparable difficulties and suggested an adaptive approach based on the value of the Jacobian at each point of Gauss. We can explore a similar approach to automatically adjust η_1 during the optimization procedure and avoid the famous issues in quasi-voids.

da Senhora *et al.* (2020) proposed restarting the Lagrange multipliers, $\boldsymbol{\mu}$, and the penalty coefficient, φ, every time the optimization stagnates. Despite this procedure seeming to be prosperous – especially given its reported propensity toward mass reduction – our simulations only stagnated in instances when the imposed load was very high and culminated in stress concentrations.

In this sense, it is not obvious whether this reboot will be effective, and one may look into its viability.

We can extend our research to solve self-contact problems (Frederiksen *et al.*, 2024) or reformulate it to deal with some energy criterion (Deng *et al.*, 2019, 2020). Concerning the last alternative, we might use distortion energy constraints in place of the stress. This would allow us to somehow incorporate uncertainties – such as in specimen dimensions, manufacturing processes, and operational conditions – in the numerical integration of energy. By doing so, we will be able to define realistic energy limits that may be coupled into the optimization framework. Then, it will be possible to constrain the distortion energy to the estimated limit.

Bibliography

Achtziger, W., & Kanzow, C. 2008. **Mathematical programs with vanishing constraints: optimality conditions and constraint qualifications**. *Mathematical Programming*, $\mathbf{114}(1)$, 69–99.

Albertyne, R. 2014. *Lecture Notes in* ***Continuum Mechanics: Volume II***. `http://web.mit.edu/abeyaratne/lecturenotes.html`. Acessed in: March, 2016.

Bathe, K.J. 2014. ***Finite Element Procedures***. 2nd edn. Upper Saddle River, New Jersey: Prentice Hall.

Bendsøe, M.P. 1989. **Optimal shape design as a material distribution problem**. *Structural and Multidisciplinary Optimization*, $\mathbf{1}(4)$, 193–202.

Bendsøe, M.P., & Kikuchi, N. 1988. **Generating optimal topologies in structural design using a homogenization method**. *Computer Methods in Applied Mechanics and Engineering*, $\mathbf{71}(2)$, 197–224.

Bendsøe, M.P., & Sigmund, O. 2003. ***Topology Optimization: Theory, Methods and Applications***. 2nd edn. Berlin, Germany: Springer-Verlag Berlin Heidelberg.

Bertsekas, D.P. 1999. ***Nonlinear Programming***. 2nd edn. Belmont, Massachusetts: Athena Scientific.

Birgin, E.G., & Martínez, J.M. 2014. ***Practical augmented Lagrangian methods for constrained optimization***. Philadelphia, Pennsylvania: SIAM.

Bonet, J., & Wood, R.D. 2008. ***Nonlinear Continuum Mechanics for Finite Element Analysis***. 2nd edn. New York, New York: Cambridge University Press.

Bourdin, B. 2001. **Filters in topology optimization**. *International Journal for Numerical Methods in Engineering*, $\mathbf{50}(9)$, 2143–2158.

Bower, A.F. 2009. ***Applied Mechanics of Solids***. Boca Raton, Florida: CRC Press.

Boyd, S.P., & Vandenberghe, L. 2004. ***Convex Optimization***. New York, New York: Cambridge University Press.

Bruggi, M. 2008. **On an alternative approach to stress constraints relaxation in topology optimization**. *Structural and Multidisciplinary Optimization*, **36**(2), 125–141.

Bruggi, M., & Venini, P. 2007. **A mixed FEM approach to stress-constrained topology optimization**. *International Journal for Numerical Methods in Engineering*, **73**(12), 1693–1714.

Bruns, T., & Tortorelli, D. 1998. **Topology optimization of geometrically nonlinear structures and compliant mechanisms**. *Page 4950 of: 7th aiaa/usaf/nasa/issmo symposium on multidisciplinary analysis and optimization*. American Institute of Aeronautics and Astronautics.

Bruns, T.E., & Tortorelli, D.A. 2001. **Topology optimization of non-linear elastic structures and compliant mechanisms**. *Computer Methods in Applied Mechanics and Wngineering*, **190**(26-27), 3443–3459.

Bruns, T.E., & Tortorelli, D.A. 2003. **An element removal and reintroduction strategy for the topology optimization of structures and compliant mechanisms**. *International Journal for Numerical Mmethods in Engineering*, **57**(10), 1413–1430.

Buhl, T., Pedersen, C.B.W., & Sigmund, O. 2000. **Stiffness design of geometrically nonlinear structures using topology optimization**. *Structural and Multidisciplinary Optimization*, **19**, 93–104.

Capasso, G., Morlier, J., Charlotte, M., & Coniglio, S. 2020. **Stress-based topology optimization of compliant mechanisms using nonlinear mechanics**. *Mechanics & Industry*, **21**(3), 304.

Chen, F., Wang, Y., Wang, M.Y., & Zhang, Y.F. 2017. **Topology optimization of hyperelastic structures using a level set method**. *Journal of Computational Physics*, **351**, 437–454.

Chen, Q., Zhang, X., & Zhu, B. 2019. **A 213-line topology optimization code for geometrically nonlinear structures.** *Structural and Multidisciplinary Optimization*, **59**, 1863–1879.

Chen, Y., Monteiro, E., Koutiri, I., & Favier, V. 2024. **Stress-constrained topology optimization using the constrained natural element method**. *Structural and Multidisciplinary Optimization*, **67**(4), 65.

Cheng, G., & Jiang, Z. 1992. **Study on topology optimization with stress constraints**. *Engineering Optimization*, **20**(2), 129–148.

Cheng, G.D., & Guo, X. 1997. **ε-relaxed approach in structural topology optimization**. *Structural Optimization*, **13**(4), 258–266.

Ciarlet, P.G. 1988. ***Mathematical Elasticity: Three-dimensional Elasticity***. New York, New York: Elsevier.

Curnier, A. 1994. ***Computational Methods in Solid Mechanics***. Vol. 29. Springer Science & Business Media.

da Senhora, F.V. 2017. ***Topology Optimization with Stress Constraints: an Aggregation-Free Approach***. Master Thesis (in Portuguese), Department of Mechanical Engineering, Pontifical Catholic University of Rio de Janeiro, Rio de Janeiro, Brazil.

da Senhora, F.V., Giraldo-Londoño, O., Menezes, I.F.M., & Paulino, G.H. 2020. **Topology optimization with local stress constraints: a stress aggregation-free approach**. *Structural and Multidisciplinary Optimization*, **62**(4), 1639–1668.

da Silva, G.A., Beck, A.T., & Sigmund, O. 2019. **Stress-constrained topology optimization considering uniform manufacturing uncertainties**. *Computer Methods in Applied Mechanics and Engineering*, **344**, 512–537.

da Silva, G.A., Cardoso, E.L., & Beck, A.T. 2020a. **Comparison of robust, reliability-based and non-probabilistic topology optimization under uncertain loads and stress constraints**. *Probabilistic Engineering Mechanics*, **59**, 103039.

da Silva, G.A., Beck, A.T., & Sigmund, O. 2020b. **Topology optimization of compliant mechanisms considering stress constraints, manufacturing uncertainty and geometric nonlinearity**. *Computer Methods in Applied Mechanics and Engineering*, **365**, 112972.

da Silva, G.A., Aage, N., Beck, A.T., & Sigmund, O. 2021a. **Local versus global stress constraint strategies in topology optimization: a comparative study**. *International Journal for Numerical Methods in Engineering*, **122**(21), 6003–6036.

da Silva, G.A., Aage, N., Beck, A.T., & Sigmund, O. 2021b. **Three-dimensional manufacturing tolerant topology optimization with hundreds of millions**

of local stress constraints. *International Journal for Numerical Methods in Engineering*, **122**(2), 548–578.

de Leon, D.M., Alexandersen, J., O. Fonseca, J.S., & Sigmund, O. 2015. **Stress-constrained topology optimization for compliant mechanism design**. *Structural and Multidisciplinary Optimization*, **52**, 929–943.

de Leon, D.M., Gonçalves, J.F., & de Souza, C.E. 2020. **Stress-based topology optimization of compliant mechanisms design using geometrical and material nonlinearities**. *Structural and Multidisciplinary Optimization*, **62**, 231–248.

Deaton, J.D., & Grandhi, R.V. 2014. **A survey of structural and multidisciplinary continuum topology optimization: post 2000**. *Structural and Multidisciplinary Optimization*, **49**, 1–38.

Deaton, J.D., & Grandhi, R.V. 2016. **Stress-based design of thermal structures via topology optimization**. *Structural and Multidisciplinary Optimization*, **53**(2), 253–270.

Deng, H., Cheng, L., & C. To, A.C. 2019. **Distortion energy-based topology optimization design of hyperelastic materials**. *Structural and Multidisciplinary Optimization*, **59**, 1895–1913.

Deng, H., Cheng, L., Liang, X., Hayduke, D., & To, A.C. 2020. **Topology optimization for energy dissipation design of lattice structures through snap-through behavior**. *Computer Methods in Applied Mechanics and Engineering*, **358**, 112641.

Dev, C., Stankiewicz, G., & Steinmann, P. 2022. **Sequential topology and shape optimization framework to design compliant mechanisms with boundary stress constraints**. *Structural and Multidisciplinary Optimization*, **65**(6), 180.

Diaz, A., & Sigmund, O. 1995. **Checkerboard patterns in layout optimization**. *Structural Optimization*, **10**(1), 40–45.

Duysinx, P., & Bendsøe, M.P. 1998. **Topology optimization of continuum structures with local stress constraints**. *International Journal for Numerical Methods in Engineering*, **43**(8), 1453–1478.

Duysinx, P., & Sigmund, O. 1998. **New developments in handling stress constraints in optimal material distribution**. *Page 4906 of: 7th AIAA/USAF/-NASA/ISSMO Symposium on Multidisciplinary Analysis and Optimization*.

Eschenauer, H.A., & Olhoff, N. 2001. **Topology optimization of continuum structures: a review**. *Applied Mechanics Review*, $\mathbf{54}(4)$, 331–390.

Fernández, E., Collet, M., Alarcón, P., Bauduin, S., & Duysinx, P. 2019. **An aggregation strategy of maximum size constraints in density-based topology optimization**. *Structural and Multidisciplinary Optimization*, $\mathbf{60}(5)$, 2113–2130.

Fontes, V.O., Leitão, A.X., & Pereira, A. to appear. **`HyperSym`: an educational MATLAB code for hyperelasticity**. *Computer Applications in Engineering Education*.

Frederiksen, A.H., Sigmund, O., & Poulios, K. 2024. **Topology optimization of self-contacting structures**. *Computational Mechanics*, $\mathbf{73}(4)$, 967–981.

Giraldo-Londoño, O., & Paulino, G.H. 2020. **A unified approach for topology optimization with local stress constraints considering various failure criteria: von Mises, Drucker–Prager, Tresca, Mohr–Coulomb, Bresler–Pister and Willam–Warnke**. *Proceedings of the Royal Society A. Mathematical and Physical Sciences*, $\mathbf{476}(2238)$, 20190861.

Giraldo-Londoño, O., & Paulino, G.H. 2021. **`PolyStress`: a Matlab implementation for local stress-constrained topology optimization using the augmented Lagrangian method**. *Structural and Multidisciplinary Optimization*, $\mathbf{63}(4)$, 2065–2097.

Gomes, F.A.M., & Senne, T.A. 2014. **An algorithm for the topology optimization of geometrically nonlinear structures**. *International Journal for Numerical Methods in Engineering*, $\mathbf{99}(6)$, 391–409.

Große, N. 2019. ***Nonlinear Topology Optimization with Compressible Hyperelastic Material Models***. Master Thesis, Institute of Aircraft Design, Technical University of Munich, Munich, Germany.

Guest, J.K., Prévost, J.H., & Belytschko, T. 2004. **Achieving minimum length scale in topology optimization using nodal design variables and projection functions**. *International Journal for Numerical Methods in Engineering*, $\mathbf{61}(2)$, 238–254.

Guo, X., Zhang, W., & Zhong, W. 2014. **Doing topology optimization explicitly and geometrically – a new moving morphable components based framework**. *Journal of Applied Mechanics*, $\mathbf{81}(8)$.

Haber, R.B., Jog, C. S, & Bendsøe, M.P. 1996. **A new approach to variable-topology shape design using a constraint on perimeter**. *Structural Optimization*, **11**(1-2), 1–12.

Hackett, R.M. 2016. ***Hyperelasticity Primer***. Springer.

Han, Y., & Wang, Q. 2022. **Numerical simulation of stress-based topological optimization of continuum structures under casting constraints**. *Engineering with Computers*, **38**(6), 4919–4945.

Han, Y., Xu, B., Duan, Z., & Huang, X. 2021. **Controlling the maximum stress in structural stiffness topology optimization of geometrical and material nonlinear structures**. *Structural and Multidisciplinary Optimization*, **64**(6), 3971–3998.

Hashiguchi, K. 2020. ***Nonlinear continuum mechanics for finite elasticity-plasticity: multiplicative decomposition with subloading surface model***. Elsevier.

Hecht, F. 2012. **New development in FreeFem++**. *Journal of Numerical Mathematics*, **20**(3-4), 251–265.

Hestenes, M.R. 1969. **Multiplier and gradient methods**. *Journal of Optimization Theory and Applications*, **4**(5), 303–320.

Holmberg, E., Torstenfelt, B., & Klarbring, A. 2013. **Stress constrained topology optimization**. *Structural and Multidisciplinary Optimization*, **48**(1), 33–47.

Holzapfel, A.G. 2000. ***Nonlinear Solid Mechanics: A Continuum Approach for Engineering***. Chichester, West Sussex: Wiley.

Huang, X., & Xie, Y.M. 2007. **Convergent and mesh-independent solutions for the bi-directional evolutionary structural optimization method**. *Finite Elements in Analysis and Design*, **43**(14), 1039–1049.

Jeong, S.H., Choi, D.H., & Yoon, G.H. 2014. **Separable stress interpolation scheme for stress-based topology optimization with multiple homogenous materials**. *Finite Elements in Analysis and Design*, **82**, 16–31.

Kawamoto, A. 2009. **Stabilization of geometrically nonlinear topology optimization by the Levenberg–Marquardt method**. *Structural and Multidisciplinary Optimization*, **37**, 429–433.

Kim, N.H. 2015. ***Introduction to Nonlinear Finite Element Analysis***. New York, New York: Springer.

Kirsch, U. 1989. **Optimal topologies of truss structures**. *Computer Methods in Applied Mechanics and Engineering*, **72**(1), 15–28.

Kirsch, U. 1990. **On singular topologies in optimum structural design**. *Structural Optimization*, **2**(3), 133–142.

Kiyono, C.Y., Vatanabe, S.L., Silva, E.C.N., & Reddy, J.N. 2016. **A new multi-p-norm formulation approach for stress-based topology optimization design**. *Composite Structures*, **156**, 10–19.

Klarbring, A., & Strömberg, N. 2013. **Topology optimization of hyperelastic bodies including non-zero prescribed displacements**. *Structural and Multidisciplinary Optimization*, **47**, 37–48.

Kreisselmeier, G., & Steinhauser, R. 1980. **Systematic control design by optimizing a vector performance index**. *Computer Aided Design of Control Systems*, 113–117.

Lahuerta, R.D., Simões, E.T., Campello, E.M.B., Pimenta, P.M., & Silva, E.C.N. 2013. **Towards the stabilization of the low density elements in topology optimization with large deformation**. *Computational Mechanics*, **52**, 779–797.

Lawrence, E.M. 1969. ***Introduction to the Mechanics of a Continuous Medium***. Englewoods Cliffs, New Jersey: Prentice-Hill.

Lazarov, B.S., & Sigmund, O. 2011. **Filters in topology optimization based on Helmholtz-type differential equations**. *International Journal for Numerical Methods in Engineering*, **86**(6), 765–781.

Lazarov, B.S., Wang, F., & Sigmund, O. 2016. **Length scale and manufacturability in density-based topology optimization**. *Archive of Applied Mechanics*, **86**, 189–218.

Le, C., Norato, J.A., Bruns, T.E., Ha, C., & Tortorelli, D. 2010. **Stress-based topology optimization for continua**. *Structural and Multidisciplinary Optimization*, **41**(4), 605–620.

Lee, E., James, K.A., & Martins, J.R.R.A. 2012. **Stress-constrained topology optimization with design-dependent loading**. *Structural and Multidisciplinary Optimization*, **46**, 647–661.

Lee, H.A., & Park, G.J. 2012. **Topology optimization for structures with nonlinear behavior using the equivalent static loads method**. *Journal of Mechanical Design*, **134**(3), 031004.

Leon, S.E., Paulino, G.H., Pereira, A., Menezes, I.F.M., & Lages, E.N. 2011. **A unified library of nonlinear solution schemes**. *Applied Mechanics Reviews*, **64**(4), 040803.

Luo, Y., Wang, M.Y., & Kang, Z. 2015. **Topology optimization of geometrically nonlinear structures based on an additive hyperelasticity technique**. *Computer Methods in Applied Mechanics and Engineering*, **286**, 422–441.

Mase, G.T., & Mase, G.E. 1999. ***Continuum Mechanics for Engineers***. 2nd edn. Boca Raton, Florida: CRC Press.

MatWeb. 2024a. ***Overview of materials for Nylon 6-3***. `https://matweb.com/search/DataSheet.aspx?MatGUID=46e36700587f4c128d65618465f0cc6e`. Acessed in: July, 2024.

MatWeb. 2024b. ***Overview of materials for Nylon 610***. `https://matweb.com/search/DataSheet.aspx?MatGUID=e7193242a22843fc9d7076bf5dbe18e4`. Acessed in: July, 2024.

MatWeb. 2024c. ***Overview of materials for Polyetheretherketone, Unreinforced***. `https://matweb.com/search/DataSheet.aspx?MatGUID=2164cacabcde4391a596640d553b2ebe&ckck=1`. Acessed in: July, 2024.

Meng, Q., Xu, B., Huang, C., & Wang, G. 2021. **Lightweight topology optimization of thermal structures under compliance, stress and temperature constraints**. *Journal of Thermal Stresses*, **44**(9), 1121–1149.

Mooney, M. 1940. **A theory of large elastic deformation**. *Journal of applied physics*, **11**(9), 582–592.

Nguyen, S.H., & Kim, H.-G. 2020. **Stress-constrained shape and topology optimization with the level set method using trimmed hexahedral meshes**. *Computer Methods in Applied Mechanics and Engineering*, **366**, 113061.

Nguyen, T.H., Paulino, G.H., Song, J., & Le, C.H. 2010. **A computational paradigm for multiresolution topology optimization (MTOP)**. *Structural and Multidisciplinary Optimization*, **41**, 525–539.

Nocedal, J., & Wright, S.J. 2006. ***Numerical Optimization***. 2nd edn. New York, New York: Springer.

Ogden, R.W. 1972. **Large deformation isotropic elasticity — on the correlation of theory and experiment for compressible rubberlike solids**. *Proceedings of the Royal Society A. Mathematical and Physical Sciences*, **328**(1575), 567–583.

París, J., Navarrina, F., Colominas, I., & Casteleiro, M. 2010. **Block aggregation of stress constraints in topology optimization of structures**. *Advances in Engineering Software*, **41**(3), 433–441.

Petersson, J., & Sigmund, O. 1998. **Slope constrained topology optimization**. *International Journal for Numerical Methods in Engineering*, **41**(8), 1417–1434.

Poon, N.M.K., & Martins, J.R.R.A. 2007. **An adaptive approach to constraint aggregation using adjoint sensitivity analysis**. *Structural and Multidisciplinary Optimization*, **34**(1), 61–73.

Reddy, J.N. 2008. ***An Introduction to Continuum Mechanics***. Cambridge University Press.

Reinisch, Joseph, Wehrle, Erich, & Achleitner, Johannes. 2021. **Multiresolution topology optimization of large-deformation path-generation compliant mechanisms with stress constraints**. *Applied Sciences*, **11**(6), 2479.

Rivlin, R.S. 1948. **Large elastic deformations of isotropic materials IV. Further developments of the general theory**. *Philosophical Transactions of the Royal Society of London. Series A, Mathematical and Physical Sciences*, **241**(835), 379–397.

Rozvany, G.I.N. 2001. **On design-dependent constraints and singular topologies**. *Structural and Multidisciplinary Optimization*, **21**(2), 164–172.

Rus, D., & Tolley, M.T. 2015. **Design, fabrication and control of soft robots**. *Nature*, **521**(7553), 467–475.

Russ, J.B., & Waisman, H. 2021. **A novel elastoplastic topology optimization formulation for enhanced failure resistance via local ductile failure constraints and linear buckling analysis**. *Computer Methods in Applied Mechanics and Engineering*, **373**, 113478.

Senne, T.A., Gomes, F.A.M., & Santos, S.A. 2023. **Inexact Newton method with iterative combined approximations in the topology optimization of geometrically nonlinear elastic structures and compliant mechanisms**. *Optimization and Engineering*, **24**(3), 2145–2180.

Sethian, J.A., & Wiegmann, A. 2000. **Structural Boundary Design via Level Set and Immersed Interface Methods**. *Journal of Computational Physics*, **163**(2), 489–528.

Sigmund, O. 1994. ***Design of material structures using topology optimization***. Doctoral Dissertation, Department of Mechanical Engineering/Solid Mechanics, Technical University of Denmark, Lyngby, Denmark.

Sigmund, O. 2011. **On the usefulness of non-gradient approaches in topology optimization**. *Structural and Multidisciplinary Optimization*, **43**, 589–596.

Sigmund, O. 2022. **On benchmarking and good scientific practise in topology optimization**. *Structural and Multidisciplinary Optimization*, **65**(11), 315.

Sigmund, O., & Maute, K. 2013. **Topology optimization approaches: A comparative review**. *Structural and Multidisciplinary Optimization*, **48**(6), 1031–1055.

Sigmund, O., & Petersson, J. 1998. **Numerical instabilities in topology optimization: a survey on procedures dealing with checkerboards, mesh-dependencies and local minima**. *Structural Optimization*, **16**(1), 68–75.

Simo, J.C., & Pister, K.S. 1984. **Remarks on rate constitutive equations for finite deformation problems: computational implications**. *Computer Methods in Applied Mechanics and Engineering*, **46**(2), 201–215.

Stankiewicz, G., Dev, C., & Steinmann, P. 2022. **Geometrically nonlinear design of compliant mechanisms: Topology and shape optimization with stress and curvature constraints**. *Computer Methods in Applied Mechanics and Engineering*, **397**, 115161.

Stolpe, M., & Svanberg, K. 2001. **On the trajectories of the epsilon-relaxation approach for stress-constrained truss topology optimization**. *Structural and Multidisciplinary Optimization*, **21**(2), 140–151.

Svanberg, K. 1984. **On Local and Global Minima in Strutural Optimization**. *Chap. 15, pages 327–341 of:* Atrek, E., Gallagher, R.H., Ragsdell, K.M., & Zienkiewicz, O.C. (eds), *New Directions in Optimum Structural Design*. Wiley.

Svanberg, K. 1987. **The method of moving asymptotes—a new method for structural optimization**. *International Journal for Numerical Methods in Engineering*, **24**(2), 359–373.

Svanberg, K. 2002. **A class of globally convergent optimization methods based on conservative convex separable approximations**. *SIAM Journal on Optimization*, $\mathbf{12}$(2), 555–573.

Svanberg, K. 2007. ***Svanberg matematisk optimering och IT AB***. `http://www.smoptit.se/`. Acessed in: October, 2022.

Svärd, H. 2015. **Interior value extrapolation: a new method for stress evaluation during topology optimization**. *Structural and Multidisciplinary Optimization*, $\mathbf{51}$, 613–629.

Sved, G., & Ginos, Z. 1968. **Structural optimization under multiple loading**. *International Journal of Mechanical Sciences*, $\mathbf{10}$(10), 803–805.

Talischi, C., Paulino, G.H., Pereira, A., & Menezes, I.F.M. 2012. **`PolyMesher`: a general-purpose mesh generator for polygonal elements written in Matlab**. *Structural and Multidisciplinary Optimization*, $\mathbf{45}$(3), 309–328.

Tamijani, A.Y. 2021. **Stress and stiffness-based topology optimization of two-material thermal structures**. *Computers & Structures*, $\mathbf{256}$, 106641.

Truesdell, C., & Noll, W. 1992. ***The Non-Linear Field Theories of Mechanics***. New York, New York: Springer-Verlag.

Verbart, A. 2015. ***Topology Optimization with Stress Constraints***. Doctoral Dissertation, Department of Mechanical Engineering, Delft University of Technology, Delft, Netherlands.

Verbart, A., Langelaar, M., & Van Keulen, F. 2016. **Damage approach: A new method for topology optimization with local stress constraints**. *Structural and Multidisciplinary Optimization*, $\mathbf{53}$(5), 1081–1098.

Verbart, A., Langelaar, M., & Van Keulen, F. 2017. **A unified aggregation and relaxation approach for stress-constrained topology optimization**. *Structural and Multidisciplinary Optimization*, $\mathbf{55}$(2), 663–679.

Wang, B., Bai, J., Lu, S., & Zuo, W. 2023. **Structural topology optimization considering geometrical and load nonlinearities**. *Computers & Structures*, $\mathbf{289}$, 107190.

Wang, C., & Qian, X. 2018. **Heaviside projection-based aggregation in stress-constrained topology optimization**. *International Journal for Numerical Methods in Engineering*, $\mathbf{115}$(7), 849–871.

Wang, C., Zhao, Z., Zhou, M., Sigmund, O., & Zhang, X.S. 2021. **A comprehensive review of educational articles on structural and multidisciplinary optimization**. *Structural and Multidisciplinary Optimization*, 1–54.

Wang, F., Lazarov, B.S., & Sigmund, O. 2011. **On projection methods, convergence and robust formulations in topology optimization**. *Structural and Multidisciplinary Optimization*, **43**(6), 767–784.

Wang, F., Lazarov, B.S., Sigmund, O., & Jensen, J.S. 2014. **Interpolation scheme for fictitious domain techniques and topology optimization of finite strain elastic problems**. *Computer Methods in Applied Mechanics and Engineering*, **276**, 453–472.

Wang, M.Y., Wang, X., & Guo, D. 2003. **A level set method for structural topology optimization**. *Computer Methods in Applied Mechanics and Engineering*, **192**(1-2), 227–246.

Wang, R., Zhang, X., Zhu, B., Zhang, H., Chen, B., & Wang, H. 2020. **Topology optimization of a cable-driven soft robotic gripper**. *Structural and Multidisciplinary Optimization*, **62**, 2749–2763.

Wu, Y., Qiu, W., Xia, L., Li, W., & Feng, K. 2021. **Design of an aircraft engine bracket using stress-constrained bi-directional evolutionary structural optimization method**. *Structural and Multidisciplinary Optimization*, **64**, 4147–4159.

Xie, Y.M., & Steven, G.P. 1993. **A simple evolutionary procedure for structural optimization**. *Computers & Structures*, **49**(5), 885–896.

Yang, D., Liu, H., Zhang, W., & Li, S. 2018. **Stress-constrained topology optimization based on maximum stress measures**. *Computers & Structures*, **198**, 23–39.

Ye, H.-L., Yuan, B.-S., Li, J.-C., Zhang, X., & Sui, Y.-k. 2021. **Geometrically nonlinear topology optimization of continuum structures based on an independent continuous mapping method**. *Acta Mechanica Solida Sinica*, 1–15.

Yoon, G.H., & Kim, Y.Y. 2005. **Element connectivity parameterization for topology optimization of geometrically nonlinear structures**. *International Journal of Solids and Structures*, **42**(7), 1983–2009.

Yoon, G.H., Noh, J.Y., & Kim, Y. 2011. **Topology optimization of geometrically nonlinear structures tracing given load-displacement curves**. *Journal of Mechanics of Materials and Structures*, **6**(1), 605–625.

Zhang, G., Alberdi, R., & Khandelwal, K. 2018. **Topology optimization with incompressible materials under small and finite deformations using mixed u/p elements**. *International Journal for Numerical Methods in Engineering*, **115**(8), 1015–1052.

Zhou, M., & Rozvany, G.I.N. 1991. **The COC algorithm, Part II: Topological, geometrical and generalized shape optimization**. *Computer Methods in Applied Mechanics and Engineering*, **89**(1-3), 309–336.

Zhu, B., Zhang, X., Li, H., Liang, J., Wang, R., Li, H., & Nishiwaki, S. 2021. **An 89-line code for geometrically nonlinear topology optimization written in FreeFEM**. *Structural and Multidisciplinary Optimization*, **63**, 1015–1027.

A
Stress Constraints in Linear-Elastic Problems

We intend to discuss the metrics employed to address stresses in the topology optimization problems. We start by assessing techniques aimed at dealing with the singular optimum phenomenon. Next, we address the large-scale problem by first examining aggregation metrics before turning our attention to regionalization strategies. Lastly, we examine how some of these tactics affect the response of an L-bracket and compare them with the ALM of Section 5.2.

A.1
Linear-Elastic Stress-Constrained Topology Optimization Problem

The stress-constrained topology optimization problem under small deformation theory is

$$\min_{\boldsymbol{z}} \quad m(\boldsymbol{z}) = \frac{1}{V_0}\sum_{e=1}^{N_e} \tilde{\rho}_e(\boldsymbol{z}) V_e \tag{A.1a}$$

$$\text{s.t.:} \quad g_j(\boldsymbol{z}) = \frac{\sigma_j^{vM}(\boldsymbol{z})}{\sigma_{lim}} - 1 \leqslant 0, \quad \text{for } j = 1, 2, \ldots, N_c \tag{A.1b}$$

$$0 \leqslant z_k \leqslant 1, \quad \text{for } k = 1, 2, \ldots, N_d \tag{A.1c}$$

$$\text{with} \quad \boldsymbol{K}(\boldsymbol{z})\boldsymbol{u} = \boldsymbol{f}, \tag{A.1d}$$

where Equation (A.1a) represents the volume fraction[13], which is a function of the initial volume distribution, V_0, the volume of the e-th element, V_e, and the regularized design variable, $\tilde{\rho}_e$, discussed in Chapter 4.

In Equation (A.1b) σ_{lim} is the limit or allowable stress (set as the yield value), and N_c is the number of constraints. This expression restricts the von Mises stress at each evaluation point, j – in this dissertation, j is the centroid of each element.

Equation (A.1c) imposes box constraints on the N_d design variables. The optimization must respect the equilibrium of Equation (A.1d), where the stiffness matrix, $\boldsymbol{K}(\boldsymbol{z})$, depends on the design variable due to the SIMP

[13]Because we assume isotropic material properties, the mass density remains uniform and constant through optimization. Therefore, it is unnecessary to explicitly include it in Equation (A.1a).

material interpolation function (see Chapter 4), while the vector of applied loads, $\boldsymbol{f}$, is assumed constant.

A.2 Stress Model

When using penalization methods, such as SIMP, stresses at intermediate design variables might carry a physical definition. In this case, assuming the design variable represents the effective stiffness of a porous microstructure (Duysinx & Bendsøe, 1998), one may establish different stress measures based on microscopic and macroscopic levels.

The macroscopic stress theory is not suitable for topology optimization problems since the stresses are invariant to modifications on the design variable (see da Senhora, 2017, Section 3.3 for further details). An alternative is to employ the stress experienced at the microscopic level.

Duysinx & Bendsøe (1998) proposed a stress model that mimics the behavior of the microscopic (or local) stresses in a rank-2 layered composite. As a result, the stress (vector) in a point j takes the form of

$$\boldsymbol{\sigma}_j = \mathbf{D}_j^0 \boldsymbol{B}_j \boldsymbol{u}_j(\tilde{\boldsymbol{\rho}}) \tag{A.2}$$

in linear-elastic problems, where $\boldsymbol{B}_j$ is a matrix relating strain and displacements in the FE theory.

Anyway, when material is removed $\lim_{\tilde{\rho}_j \to 0} \boldsymbol{\sigma}_j \neq \mathbf{0}$. That is, when the design variable is null, the stress assumes a nonzero value, leading to a stress measure that does not properly represent the physics at quasi-voids, and we must correct it.

A.3 Singular Optimum Techniques

There are numerous approaches to couple with the singular phenomenon: the ε-relaxation (Cheng & Guo, 1997), the *qp*-approach (Bruggi & Venini, 2007; Bruggi, 2008), the use of relaxed stress measures (Le *et al.*, 2010), and the TVC and PVC detached on Sections 5.1.1.1 and 5.1.1.2 are some of them. In the following, we introduce some of these approaches.

A.3.1 ε-relaxation

The ε-relaxation was first introduced in truss optimization problems and has also proved effective for continuum topology optimization. The set of

constraints in the form of

$$g_j(\boldsymbol{z}) = \tilde{\rho}_j(\boldsymbol{z}) \left(\frac{\sigma_j^{vM}(\boldsymbol{z})}{\sigma_{lim}} - 1 \right) \leqslant 0, \quad \text{for } j = 1, 2, \ldots, N_c$$

is converted to

$$g_j^{\varepsilon}(\boldsymbol{z}, \varepsilon) = \tilde{\rho}_j(\boldsymbol{z}) \left(\frac{\sigma_j^{vM}(\boldsymbol{z})}{\sigma_{lim}} - 1 \right) \leqslant \varepsilon, \quad \text{for } j = 1, 2, \ldots, N_c, \tag{A.3}$$

where $0 < \varepsilon \ll 1$ dictates the amount of allowed perturbation.

In practice, Equation (A.3) opens or extends the space of admissible solutions, and degenerated subspaces no longer exist, as they are now within the extended feasible set. Nevertheless, this expression overestimates the stress limit in structural elements:

$$\sigma_j^{vM}(\boldsymbol{z}) \leqslant \sigma_{lim}(1 + \varepsilon), \quad \text{for } \tilde{\rho}_j(\boldsymbol{z}) = 1.$$

To eliminate this undesirable effect, Duysinx & Sigmund (1998) introduced the following version of the ε-relaxation:

$$g_j^{\varepsilon}(\boldsymbol{z}, \varepsilon) = \tilde{\rho}_j(\boldsymbol{z}) \left(\frac{\sigma_j^{vM}(\boldsymbol{z})}{\sigma_{lim}} - 1 \right) \leqslant \varepsilon(1 - \tilde{\rho}_j(\boldsymbol{z})), \quad \text{for } j = 1, 2, \ldots, N_c. \tag{A.4}$$

The optimization solution, though, becomes dependent on the selected ε, whose ideal value is unknown priori and may be problem-dependent. The difficulty of achieving the true optimal allows researchers to look for alternative methods.

We would like to emphasize that stress-constrained topology optimization is a non-convex problem (Svanberg, 1984; Bruggi & Venini, 2007), which implies the global (true) optimal is hard to be achieved. In other words, the optimization algorithm tends to converge to a local minimum point, and one is likely to find different designs or rates of convergence even for small changes in the methods or optimization parameters employed. Based on that, we can justify the use of ε-relaxation in recent works (e.g. da Silva *et al.*, 2019, 2021a,b).

A.3.2 *qp*-approach

Given the limitations of ε-relaxation, Bruggi & Venini (2007) discussed a new option: the *qp*-approach. The concept – inspired by Duysinx & Bendsøe (1998) – assumes the stress vector is in the form of

$$\boldsymbol{\sigma}_j(\boldsymbol{z}) = \tilde{\rho}_j^{p-q} \mathbf{D}_j^0 \boldsymbol{B}_j \boldsymbol{u}_j(\tilde{\boldsymbol{\rho}}), \quad \text{for } q < p, \tag{A.5}$$

in which we omit $\tilde{\rho}_j$-dependence in the displacement field for conciseness.

Since $\tilde{\rho}_j^p$ grows more rapidly to infinite than $\tilde{\rho}_j^q$, we have that

$$\lim_{\tilde{\rho}_j \to 0} \boldsymbol{\sigma}_j(\boldsymbol{z}) = \lim_{\tilde{\rho}_j \to 0} \tilde{\rho}_j^{p-q} \mathbf{D}_j^0 \boldsymbol{B}_j \boldsymbol{u}_j(\tilde{\boldsymbol{\rho}}) = \lim_{\tilde{\rho}_j \to 0} \frac{\tilde{\rho}_j^p}{\tilde{\rho}_j^q} \mathbf{D}_j^0 \boldsymbol{\epsilon}_j = \mathbf{0}. \tag{A.6}$$

So, the stress model of Equation (A.5) gains physical meaning when material is removed within the design domain.

Yet, the constraints are written in the form of

$$g_j^{qp}(\boldsymbol{z}, p, q) = \tilde{\rho}_j^{p-q} \frac{\sigma_j^{vM}(\boldsymbol{z})}{\sigma_{lim}} - 1 \leqslant 0, \quad \text{for } j = 1, 2, \ldots, N_c, \tag{A.7}$$

where typically $q \in [2, p)$, for p being the SIMP exponent.

Bruggi (2008) further investigated the properties of the *qp*-approach and realized it is "a sort of adaptive ε-relaxation". He concluded that both schemes produce the same perturbation of stress constraints; that is, both extend the feasible region containing the degenerated subspaces.

A.3.3 Relaxed Stress

Interested in black-and-white designs, Le *et al.* (2010) introduced the idea of relaxed stresses, which are obtained from penalizing the stresses as:

$$\hat{\boldsymbol{\sigma}}_j(\boldsymbol{z})\} = \eta_\sigma(\tilde{\rho}_j) \boldsymbol{\sigma}_j(\boldsymbol{z}). \tag{A.8}$$

The stress interpolation function, $\eta_\sigma(\tilde{\rho}_j)$, should obey the following conditions:

(i) $\eta_\sigma(\tilde{\rho}_j)$ is a monotonically increasing function,

(ii) $\eta_E(\tilde{\rho}_j) < \eta_\sigma(\tilde{\rho}_j) < 1$, for $0 < \tilde{\rho}_j < 1$,

(iii) $\eta_\sigma(0) = 0$, to correctly represent the void elements, and

(iv) $\eta_\sigma(1) = 1$, so the relaxed stresses are consistent with those in solid zones.

Some remarks of the relaxed stress are: (i) it can also be applied directly to the equivalent stress, such as the von Mises defined in Equation (2.22), (ii) it is easy to be implemented since one simply needs to compute the stress and multiply it by the stress interpolation function, and (iii) the choice of $\eta_\sigma(\tilde{\rho}_e)$ is versatile, as long as it respects the above criteria.

The use of relaxed stress is also a common practice. The literature provides several works exploiting it: Holmberg *et al.* (2013), Deaton & Grandhi (2016), Verbart *et al.* (2016), Wang & Qian (2018), Meng *et al.* (2021), among others.

The above-mentioned versatility of the stress interpolation function can be explained by the number of expressions to represent it. For example[14],

$$\varepsilon\text{-relaxation: } \eta_\sigma(\tilde{\rho}_j) = \frac{\tilde{\rho}_j}{\varepsilon + \tilde{\rho}_j} \qquad \text{(Lee } et\ al.\text{, 2012)},$$

$$\text{modified } \varepsilon\text{-relaxation: } \eta_\sigma(\tilde{\rho}_j) = \frac{\tilde{\rho}_j}{\varepsilon(1-\tilde{\rho}_j) + \tilde{\rho}_j} \qquad \text{(da Silva } et\ al.\text{, 2020b)},$$

$$qp\text{-approach: } \eta_\sigma(\tilde{\rho}_j) = \tilde{\rho}_j^{p-q}; \qquad \text{(Le } et\ al.\text{, 2010)},$$

$$\text{sinh: } \eta_\sigma(\tilde{\rho}_j) = 1 - \frac{\sinh(3(1-\tilde{\rho}_j))}{\sinh(3)} \qquad \text{(Le } et\ al.\text{, 2010)},$$

$$\text{Heaviside exponential: } \eta_\sigma(\tilde{\rho}_j) = 1 - \mathrm{e}^{-\delta_\sigma \tilde{\rho}_j} + \tilde{\rho}_j \mathrm{e}^{-\delta_\sigma} \qquad \text{(da Silva } et\ al.\text{, 2020a)},$$

where $\delta_\sigma > 0$ is the stress interpolation parameter.

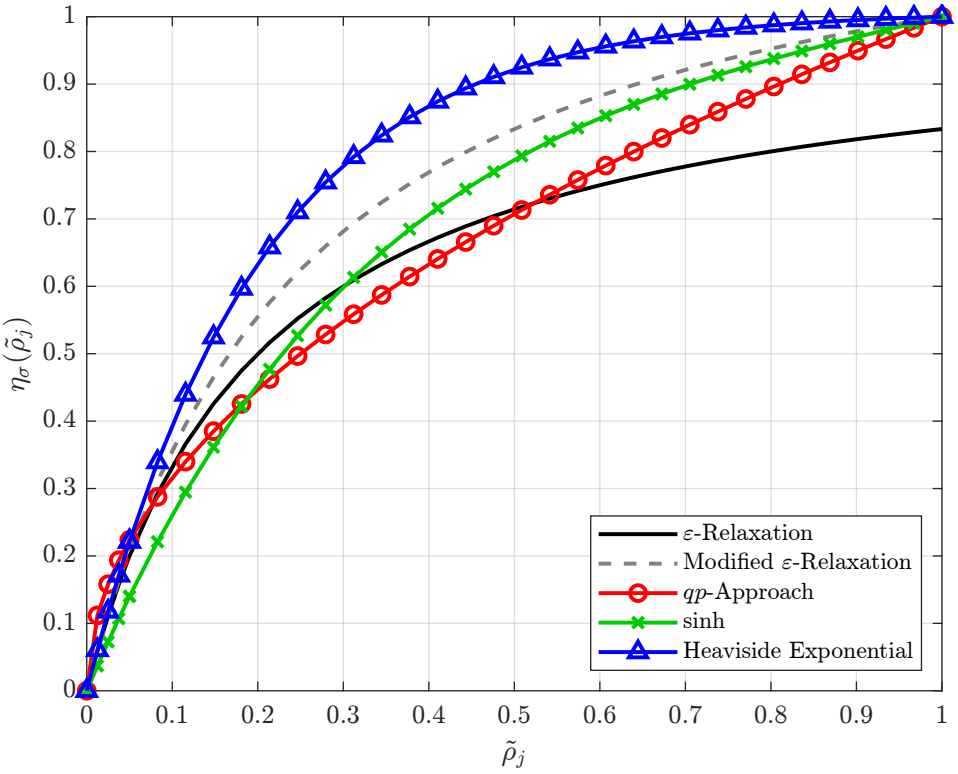

Figure A.1: Stress interpolation functions ($\varepsilon = 0.2$, $p = 3$, $q = 2.5$ and $\delta_\sigma = 5$).

Figure A.1 illustrates different stress interpolation functions. In general, those are in agreement with the imposed conditions, except for the ε-relaxation, which does not satisfy condition 4, and the stress is underestimated in $\tilde{\rho}_j = 1$ by approximately 17%:

$$\hat{\boldsymbol{\sigma}}_j(1) = \frac{1}{1.2}\boldsymbol{\sigma}_j(1) = 0.8\bar{3}\boldsymbol{\sigma}_j(1).$$

[14]The indicated references correspond to articles that used the corresponding stress interpolation and not necessarily to the works where the mentioned relaxations were proposed.

A.3.4
Comparison of Different Strategies

Verbart (2015) compared different formulations of stress constraints, and we recommend it for deeper understanding. As we could not find an explicit form for the PVC in his methodology, we investigated the stress constraints themselves in Figure A.2.

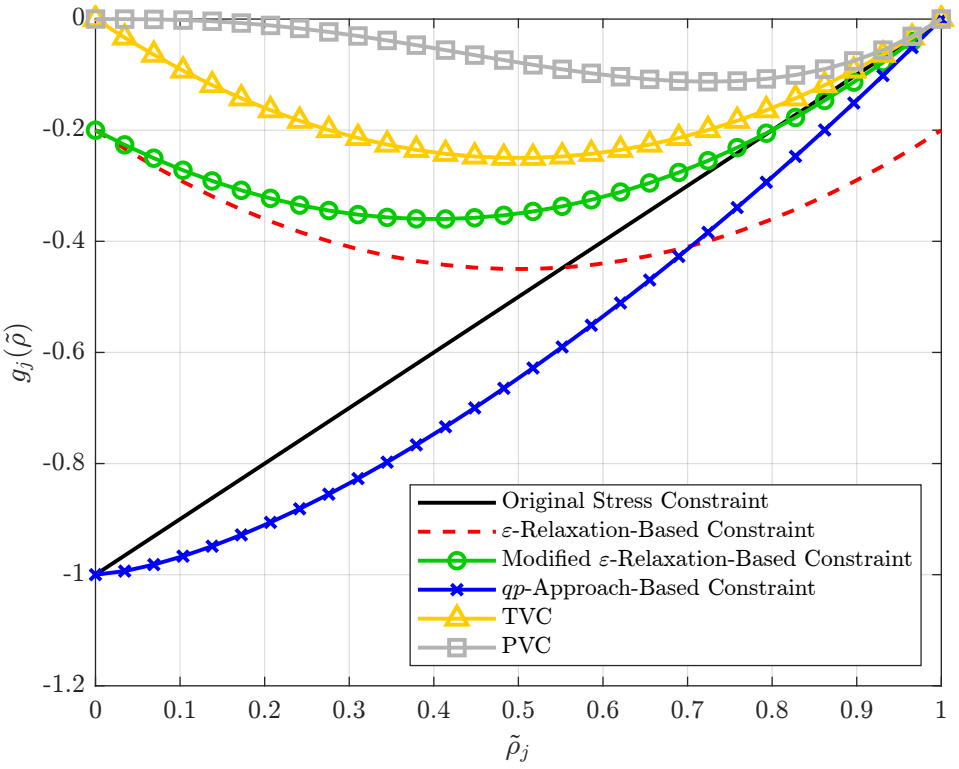

Figure A.2: Behavior of stress constraints ($\varepsilon = 0.2$ and $p - q = 0.5$).

The distinguished comportment observed in Figure A.2 raises the question: which constraint better represents void elements? In fact, all of them do. We can claim that the *qp*-approach is the only one (among those investigated) in agreement with the original stress constraint, that is, $g_j^{qp}(0) = -1$ and $g_j^{qp}(1) = 0$.

Yet, this does not mean that the other formulations are wrong. For example, the TVC and PVC return $g(0) = 0$ because they assume the constraint must remain active when the material is removed. In reality, this feature is preferable since the optimizer tends to stabilize the solution. Then, the PVC has an advantage, as its serpentine-like shape with modest amplitude pushes intermediate densities faster to zero, which hastens optimization convergence towards an optimal solution.

Recently, Chen *et al.* (2024) made an interesting comparison of employing some of these approaches in the scope of ALM. They concluded that the PVC

is more suitable as it not only keeps the original feasible set intact, but also punishes harsher regions that violate the constraints. However, they mentioned that *qp*-approach and ε-relaxation are also good options.

A.4 Stress Aggregation

Aggregation methods employ global functions to substantially reduce the computational effort associated with local stresses, especially for evaluating the derivatives.

These techniques depend on the aggregation parameter, $p_a > 0$. Consider $\Psi(g_j(x), p_a)$ a global function and $g_j(x)$, for $x \in \mathbb{R}^{\mathrm{N}}$, a local function. The aggregation techniques have the fundamental characteristic of

$$\lim_{p_a \to \infty} \Psi(g_1(x), g_2(x), \ldots, g_j(x), p_a) = \max\{g_1(x), g_2(x), \ldots, g_j(x)\}, \tag{A.9}$$

for $j = 1, 2, \ldots, N_c$.

Thus, the natural choice is choosing

$$\Psi(g_j(x)) = \max\{g_j(x)\}. \tag{A.10}$$

But Equation (A.10) is still non-differentiable, and there is no sense in coupling it with gradient-based methods.

The alternative is trying to mimic the behavior of Equation (A.9). This can be done by the P-norm (Duysinx & Sigmund, 1998; Holmberg *et al.*, 2013),

$$\Psi^{PN}(x, p_a) = \left[\sum_{j=1}^{N_c} \max\left\{0, g_j^{p_a}(x)\right\}\right]^{1/p_a}, \tag{A.11}$$

or by the P-mean (Duysinx & Sigmund, 1998; Le *et al.*, 2010; Kiyono *et al.*, 2016),

$$\Psi^{PM}(x, p_a) = \left[\frac{1}{N_c}\sum_{j=1}^{N_c} \max\left\{0, g_j^{p_a}(x)\right\}\right]^{1/p_a} \tag{A.12}$$

To better understand how these techniques work, we investigate two local functions, $g_j(x)$, for $x \in \mathbb{R}^1$:

$$g_1(x) = x^3 - \frac{1}{5}\ln(x), \quad \text{and} \tag{A.13a}$$

$$g_2(x) = -x^3 - x^2 + 2x - \frac{1}{10}. \tag{A.13b}$$

Figure A.3 shows the plot of $g_1(x)$, $g_2(x)$ and Ψ for different values of p_a. In Figure A.3(a), we observe: (i) the P-norm introduces an upper bound for the global function, Ψ^{PN}, as it approaches the peak value of local functions from above, (ii) as the higher is the value of p_a, the lower is the gap between $g_1(x)$ and $g_2(x)$, and the P-norm tends to the maximum value of the local

functions, as defined in Equation (A.9), and (iii) the larger difference between the P-norm and $g_j(x)$, for $j = 1, 2$, occurs in the intersection points, which will introduce discontinuities as the value of p_a increases, causing numerical instabilities in the optimization process.

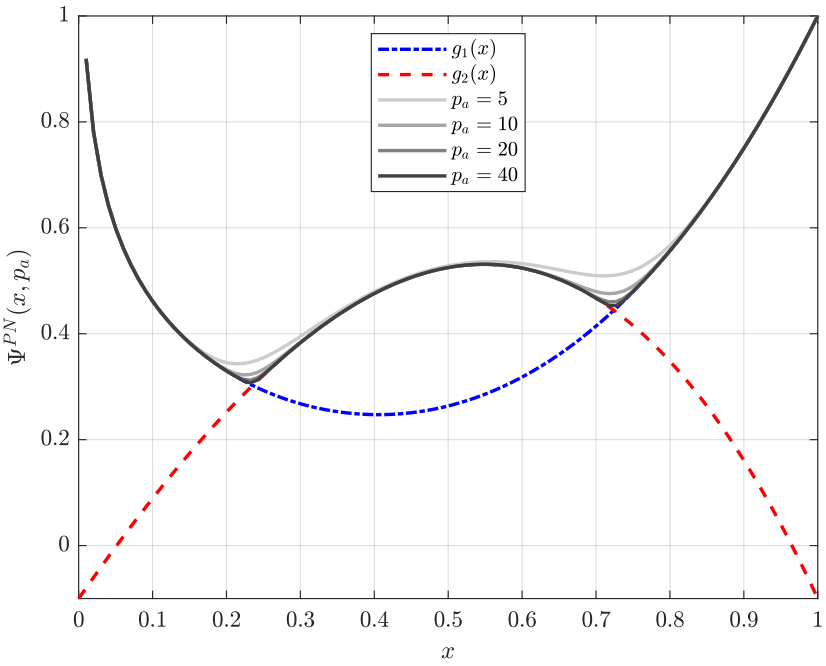

(a)

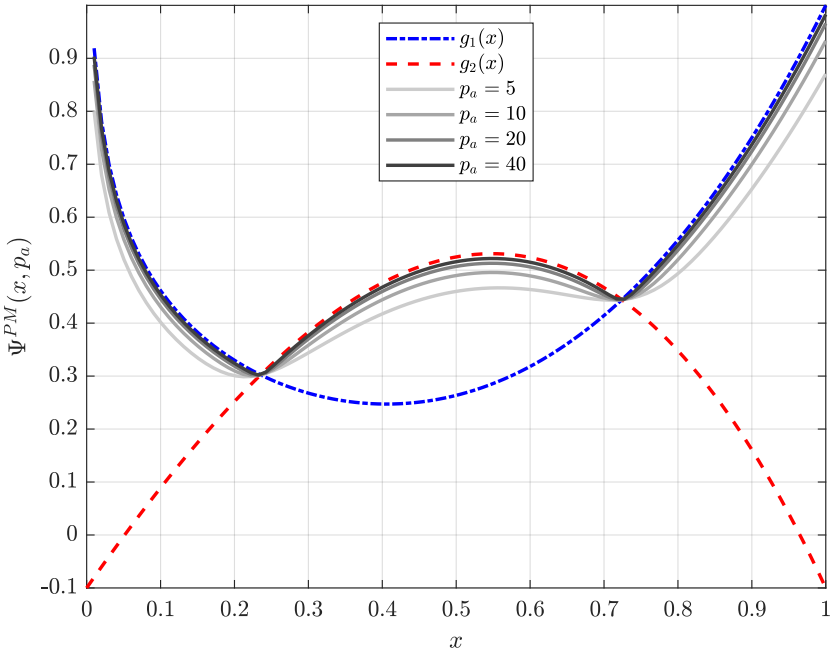

(b)

Figure A.3: P-norm-based aggregation functions: (a) P-norm, and (b) P-mean.

For the P-mean, *vid.* Figure A.3(b), we may affirm that: (i) it defines a lower bound for the aggregated functions (convergence from below), (ii) the higher the value of p_a, the closer the global function, Ψ^{PM}, is from the peak, and (iii) regardless the choice of p_a, Ψ^{PM} coincides with $g_j(x)$, for $j = 1, 2$, at the intersection points.

Bringing these insights to the realm of stress-constrained topology optimization, we may say that the P-norm overestimates the maximum stress, resulting in too-conservative designs. On the other hand, the P-mean underestimates the peak stress, culminating in unfeasible layouts.

Another aggregation technique is based on the KS function of Kreisselmeier & Steinhauser (1980). Poon & Martins (2007) defined it as

$$\Psi^{KS}(x, p_a) = \frac{1}{p_a} \ln \left(\sum_{j=1}^{N_c} \mathrm{e}^{p_a g_j(x)} \right), \tag{A.14}$$

which has the following properties:

(i) $\Psi^{KS}(x, p_a) \geqslant \max\{g_j(x)\}, \quad \forall\, p_a > 0,$

(ii) $\Psi^{KS}(x, p_{a,2}) \geqslant \Psi^{KS}(x, p_{a,1}), \quad \forall\, p_{a,2} > p_{a,1} > 0,$ and

(iii) $\Psi^{KS}(x, p_a)$ is convex $\iff \forall\, g_j(x)$ are convex.

Item (i) tells us the KS function defines an upper bound for Ψ^{KS} (similarly to Ψ^{PN}). Item (ii) is very intuitive, and Item (iii) informs that the KS function preserves convexity when all local functions, $g_j(x)$, for $j = 1, 2, \ldots, N_c$, are convex. Figure A.4(a) illustrates these properties for the local functions of Equation (A.13).

We may establish a lower bound KS function by noticing that the largest difference between the global function, Ψ^{KS}, and the maximum value of local functions ($g_{max}(x) = \max\{g_1(x), g_2(x), \ldots, g_j(x)\}$) occurs when all the values of $g_j(x)$ are equal (Poon & Martins, 2007). Using logarithmic characteristics, the largest error between the two functions is

$$\begin{gathered} \frac{1}{p_a} \ln \left(N_c \mathrm{e}^{p_a g_{max}(x)} \right) - g_{max}(x) = \\ \frac{1}{p_a} \ln(N_c) + \frac{1}{p_a} \left(\ln \left(\mathrm{e}^{p_a g_{max}(x)} \right) \right) - g_{max}(x) = \\ \frac{1}{p_a} \ln(N_c) + \frac{1}{p_a} (p_a g_{max}(x)) - g_{max}(x) = \frac{1}{p_a} \ln(N_c). \end{gathered}$$

Thus, the lower bound KS function is defined as

$$\Psi^{LKS}(x, p_a) = \Psi^{KS}(x, p_a) - \frac{1}{p_a} \ln(N_c) = \frac{1}{p_a} \ln \left(\frac{1}{N_c} \sum_{j=1}^{N_c} \mathrm{e}^{p_a g_j(x)} \right), \tag{A.15}$$

whose behavior is illustrated in Figure A.4(b) for the local functions displayed in Equation (A.13).

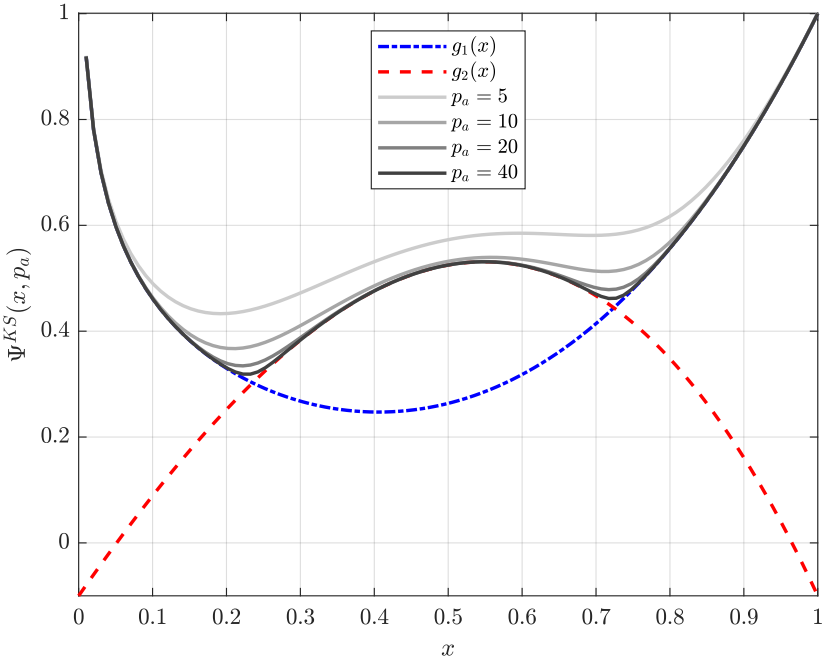

(a)

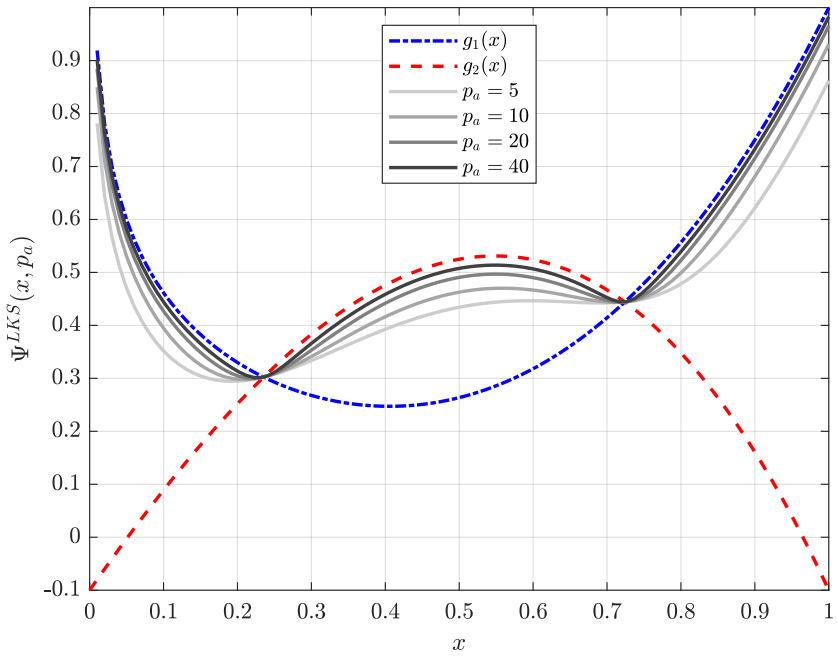

(b)

Figure A.4: KS function-based aggregation: (a) upper bound KS function, and (b) lower bound KS function.

The upper and lower bound KS functions follow the same pattern as the P-norm and P-mean, respectively. Both KS functions are important since

they are not restricted to non-negative numbers, which allows one to consider different metrics other than von Mises stress.

Aggregation in Topology Optimization Problems The aggregation methods discussed in Appendix A.4 are applied to the stress problems in many distinct forms. To mention a few: Duysinx & Sigmund (1998) combined the ε-relaxed constraints with the P-norm and the P-mean, Le *et al.* (2010) considered the von Mises stresses, $\sigma_j^{vM}(\boldsymbol{z})$, multiplied by the volume fraction to normalize the value of global function, and Kiyono *et al.* (2016) simply aggregated the von Mises stresses.

In our study case of Appendix A.6.1, we explore the notion of Holmberg *et al.* (2013), where the stress ratio, $\hat{\sigma}_j^{vM}(\boldsymbol{z})/\sigma_{lim}$, is aggregated. Aggregation like this enables us to work with normalized constraints without further complicating the sensitivity analysis with additional variables. The symbol $\hat{\bullet}$ indicates a relaxed stress measure, as addressed in Appendix A.3.3.

Thus, when using aggregation techniques the constraint

$$\hat{g}_j(\boldsymbol{z}) = \frac{\hat{\sigma}_j^{vM}(\boldsymbol{z})}{\sigma_{lim}} - 1 \leqslant 0, \quad \text{for } j = 1, 2, \ldots, N_c$$

is replaced by

$$\hat{g}^{Agg}(\boldsymbol{z}, p_a) = \hat{\Psi}(\boldsymbol{z}, p_a) - 1 \leqslant 0, \tag{A.16}$$

where $\hat{\Psi}$ is one of the following aggregations,

$$\hat{\Psi}^{PN}(\boldsymbol{z}, p_a) = \left[\sum_{j=1}^{N_c} \hat{\sigma}_r\right]^{1/p_a} \qquad \text{in the P-norm;} \tag{A.17}$$

$$\hat{\Psi}^{PM}(\boldsymbol{z}, p_a) = \left[\frac{1}{N_c}\sum_{j=1}^{N_c} \hat{\sigma}_r\right]^{1/p_a} \qquad \text{in the P-mean;} \tag{A.18}$$

$$\hat{\Psi}^{KS}(\boldsymbol{z}, p_a) = \frac{1}{p_a} \ln\left(\sum_{j=1}^{N_c} \mathrm{e}^{p_a \hat{\sigma}_r}\right) \qquad \text{in the KS function;} \tag{A.19}$$

$$\hat{\Psi}^{LKS}(\boldsymbol{z}, p_a) = \frac{1}{p_a} \ln\left(\frac{1}{N_c}\sum_{j=1}^{N_c} \mathrm{e}^{p_a \hat{\sigma}_r}\right) \qquad \text{in the lower bound KS function;} \tag{A.20}$$

where $\hat{\sigma}_r = \hat{\sigma}_j^{vM}(\boldsymbol{z})/\sigma_{lim}$.

The approximation generated by the global functions can culminate in discrepancies about the real values of the local functions. In general, this phenomenon is associated with the loss of information about the stress distribution at points where the gradient suffers a sudden variation. As a consequence, the stresses can be far below or above the established limit in the optimized design. An attempt to overcome this difficulty is to partition the

design domain into small groups or blocks, which are, then, aggregated. This procedure is known as stress regionalization.

A.5 Stress Regionalization

Stresses regionalization suggests aggregating stresses related to a given group or block, Ω_k. Therefore, instead of treating only one global function, the optimization will now consider N_b global functions. The objective is to take advantage of the best of two scenarios: the most precise quantification of stresses while defining the constraints in their local form, and a decrease in computing cost when the constraints are condensed. In this context, Equations (A.17), (A.18), (A.19) and (A.20) remain valid; the only difference is that the stresses are now summed over the number of blocks, N_b.

The blocks may be formed by different strategies based on the: (i) geometry, (ii) element index, (iii) stress distribution, or (iv) stress level. The optimized design depends directly on the chosen strategy, but all have two common characteristics: (i) if $N_b = 1$, the elements are aggregated into a single global function, and (ii) if $N_b = N_e$, then the stresses remain as local quantities.

Consider the example of Figure A.5. The mesh is defined in Figure A.5(a), and the stresses, at an arbitrary i-th iteration, are drawn in Figure A.5(e). Next, we will use this example to clarify how each block formation method works.

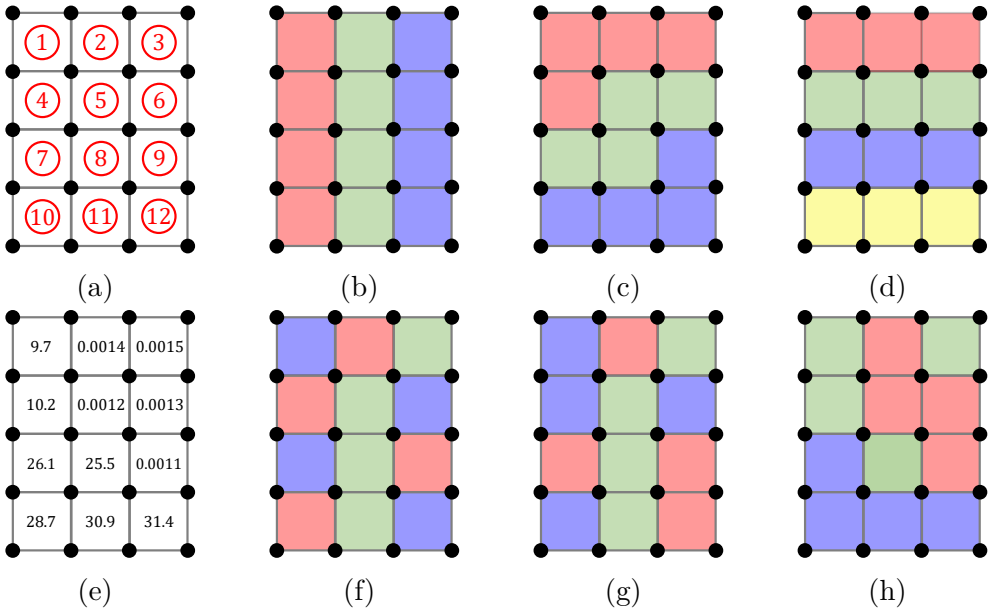

Figure A.5: Strategies for grouping the elements: (a) mesh numbering, (b) GBT, (c), EIT, (d) a possible case in which GBT results in the same block partition as EIT, (e) stress values, (f) SDT, (g) mSDT, and (h) SLT.

Geometry-Based Technique What we call the geometry-based technique (GBT) groups the stresses based on the geometry of the design domain.

Figure A.5(b) illustrates how the elements are regionalized using the GBT. In this example, the blocks are formed by the columns of the mesh, and this grouping technique is related to no aspects of the mesh. Observe that stress values are not taken into account. Then the blocks are:

$$\Omega_1 = \{e_1, e_4, e_7, e_{10}\};$$
$$\Omega_2 = \{e_2, e_5, e_8, e_{11}\};$$
$$\Omega_3 = \{e_3, e_6, e_9, e_{12}\}.$$

Element Index Technique The element index technique (EIT), of París *et al.* (2010), considers correlative indexes in the FE mesh to form the groups.

The EIT, displayed in Figure A.5(c), divides the blocks according to the element numbering – defined when the mesh is created. In the example of Figure A.5, the stresses are divided into three blocks containing successive elements:

$$\Omega_1 = \{e_1, e_2, e_3, e_4\};$$
$$\Omega_2 = \{e_5, e_6, e_7, e_8\};$$
$$\Omega_3 = \{e_9, e_{10}, e_{11}, e_{12}\}.$$

Depending on how the mesh is generated, the EIT may result in the same block partition as the GBT. This is the case when opting to form blocks using the lines as the reference in the GBT, Figure A.5(d). Then, we have four groups:

$$\Omega_1 = \{e_1, e_2, e_3\};$$
$$\Omega_2 = \{e_4, e_5, e_6\};$$
$$\Omega_3 = \{e_7, e_8, e_9\};$$
$$\Omega_4 = \{e_{10}, e_{11}, e_{12}\}.$$

Stress Distribution Technique As the GBT and EIT are purely heuristic, Le *et al.* (2010) propose a metric centered on the stress magnitude: the stress

distribution technique (SDT). Initially, the SDT requires sorting[15] the stresses,

$$\left\{\mathring{e}_1, \mathring{e}_2, \ldots, N_e : \sigma^{(i)}_{\mathring{e}_1} \leqslant \sigma^{(i)}_{\mathring{e}_2} \leqslant \cdots \leqslant \sigma^{(i)}_{N_e}\right\},$$

where $\mathring{e}_h$, for $h = 1, 2, \ldots, N_e$, represents h-th sorted element. Afterward, it sequentially groups the stresses in blocks defined as:

$$\Omega_k = \{\mathring{e}_k, \mathring{e}_{N_b+k}, \mathring{e}_{2N_b+k}, \ldots, \mathring{e}_{N_e}\}, \text{ for } k = 1, 2, \ldots, N_b. \tag{A.21}$$

Looking back at the example of Figure A.5, the SDT consists of the following blocks:

$$\begin{aligned}
\Omega_1 &= \{\mathring{e}_1, \mathring{e}_4, \mathring{e}_7, \mathring{e}_{10}\} \equiv \{e_2, e_4, e_9, e_{10}\};\\
\Omega_2 &= \{\mathring{e}_2, \mathring{e}_5, \mathring{e}_8, \mathring{e}_{11}\} \equiv \{e_3, e_5, e_8, e_{11}\};\\
\Omega_3 &= \{\mathring{e}_3, \mathring{e}_6, \mathring{e}_9, \mathring{e}_{12}\} \equiv \{e_1, e_6, e_7, e_{12}\}.
\end{aligned}$$

In the set of sorted elements, we notice that element $\mathring{e}_1$ belongs to the block Ω_1, $\mathring{e}_2$ to Ω_2, $\mathring{e}_3$ to Ω_3, and so on. After completing the N_b blocks with the first $\mathring{e}_{N_b}$ elements, the block counter is reset to 1, and the algorithm returns to Ω_1. This procedure continues until all the elements (N_e) are assigned to a group. See Figure A.5(f) for details.

Modified Stresses Distribution Technique Jeong *et al.* (2014) proposed a modification to the SDT (mSDT). The elements are still grouped by their stress magnitudes; the difference is that the higher and lower stress values belong to the same block. This technique tends to reduce peak stresses, as it uniformizes the aggregated stresses in each group. Thus, the elements are formed by the following criterion:

$$\begin{aligned}
\Omega_k = \{&\mathring{e}_k, \mathring{e}_{N_b+k}, \ldots, \mathring{e}_{N_e/2-(N_b-k)}, \mathring{e}_{N_e/2+(N_b-k)+1}, \cdots,\\
&\mathring{e}_{N_e-(N_b+k)+1}, \mathring{e}_{N_e-k+1}\}, \text{ for } k = 1, 2, \ldots, N_b.
\end{aligned} \tag{A.22}$$

In the example of Figure A.5, we observe the mSDT has the following element distribution:

$$\begin{aligned}
\Omega_1 &= \{\mathring{e}_1, \mathring{e}_4, \mathring{e}_9, \mathring{e}_{12}\} \equiv \{e_2, e_7, e_9, e_{12}\};\\
\Omega_2 &= \{\mathring{e}_2, \mathring{e}_5, \mathring{e}_8, \mathring{e}_{11}\} \equiv \{e_3, e_5, e_8, e_{11}\};\\
\Omega_3 &= \{\mathring{e}_3, \mathring{e}_6, \mathring{e}_7, \mathring{e}_{10}\} \equiv \{e_1, e_4, e_6, e_{10}\}.
\end{aligned}$$

[15]The sort type is, in general, irrelevant. So, one can opt for sorting in ascending or descending order.

From Figure A.5(g), the first block, Ω_1, contains elements $\mathring{e}_1$ and $\mathring{e}_{12}$, which correspond, respectively, to elements with the maximum and minimum stresses in the mesh. The remaining $N_b - 1$ blocks are formed by the $N_b - 1$ smallest and highest stresses: Ω_2 is composed of the element with the second lowest stress, $\mathring{e}_2$, and highest stress, $\mathring{e}_{11}$, and so on. Finally, after the k smallest and highest stresses have been arranged in the N_b blocks, the algorithm is reset to $k = 1$. That is, when $k = N_b = 3$, we return to Ω_1, which is filled with $\mathring{e}_4$ (the fourth smallest stress) and with $\mathring{e}_9$ (the fourth highest stress). This procedure is repeated until all elements have been allocated in a block.

Stresses Level Technique Holmberg *et al.* (2013) formulated the stress level technique (SLT). The idea is to divide the blocks so the stresses of similar magnitudes belong to the same block. Stresses are also sorted, and the associated elements are divided into groups constructed according to

$$\begin{aligned}\Omega_k = \{&\mathring{e}_{kN_e/N_b - N_b}, \mathring{e}_{kN_e/N_b-(N_b-1)}, \mathring{e}_{kN_e/N_b-(N_b-2)}, \dots, \\ &\mathring{e}_{kN_e/N_b-(N_b-3)}, \mathring{e}_{kN_e/N_b}\}, \text{ for } k = 1, 2, \dots, N_b.\end{aligned} \tag{A.23}$$

The SLT simply divides the element in the same order the stresses were sorted. For the example of Figure A.5, the blocks are

$$\begin{aligned}\Omega_1 &= \{\mathring{e}_1, \mathring{e}_2, \mathring{e}_3, \mathring{e}_4\} \equiv \{e_2, e_5, e_6, e_9\}; \\ \Omega_2 &= \{\mathring{e}_5, \mathring{e}_6, \mathring{e}_7, \mathring{e}_8\} \equiv \{e_1, e_3, e_4, e_8\}; \\ \Omega_3 &= \{\mathring{e}_9, \mathring{e}_{10}, \mathring{e}_{11}, \mathring{e}_{12}\} \equiv \{e_7, e_{10}, e_{11}, e_{12}\},\end{aligned}$$

as drawn in Figure A.5(h).

Perhaps the main criticism toward regionalization is that we do not know a priory the number of blocks needed to be used. Furthermore, we may wonder which of the aforementioned strategies best suits a certain problem, particularly as this decision depends on the problem itself.

If we compute the blocks at each iteration of the optimization procedure – as normally one does – the ordered stresses will also vary, and we will most likely solve a different optimization problem every iteration. Verbart (2015) pointed out that this approach hinders smooth convergence as the optimization process oscillates, and the convergence towards a feasible solution may be (very) slow.

The first option to lessen this oscillation is to simply not reassess the blocks at every iteration. Holmberg *et al.* (2013), however, claimed this strategy does not perform as desired in terms of simple designs that prevent stress

concentration.

A.5.1
Stress Adaptive Correction Factor

As discussed in Appendix A.4, the aggregated functions approximate the maximum value of local stresses, in which the quality of this approximation depends on the value of the aggregation parameter: the higher p_a is, the better the approximation; nevertheless, larger values of p_a may result in discontinues, and the optimizer may experience cumbersome convergence.

The stress adaptive correction factor, c_b, – first introduced by Le *et al.* (2010) as a heuristic parameter – is an attempt to correct such discrepancy as the optimization process is carried on. It is applicable regardless of the number of blocks or the aggregated stress measures, $\Psi_b^{(i)}$.

Hence, at the i-th iteration, we will have the corrected aggregated stress in the form of

$$c_b^{(i)} \Psi_b^{(i)},$$

with

$$c_b^{(i)} = \alpha^{(i)} \frac{\sigma_{max}^{(i)}}{\Psi_b^{(i)}} + \left(1 - \alpha^{(i)}\right) c_b^{(i-1)}. \tag{A.24}$$

$\sigma_{max}^{(i)}$ is the maximum von Mises stress at the current iteration, $\sigma_{max}^{(i)} = \max\{\sigma_e^{vM;(i)}\}$, and $\alpha^{(i)} \in (0, 1]$ is a damping parameter to be adjusted during the optimization process. When c_b does not oscillate, $\alpha^{(i)} = 1$ and no correction to global stresses is made; otherwise, one must choose any value in the range $0 \leqslant \alpha^{(i)} \leqslant 1$.

We detach this stress adaptive correction factor is applied for $1 \leqslant b \leqslant N_b$, in which b is the block counter. In other words, if one considers ten blocks, there will be ten values of c_b.

Le *et al.* (2010) detached one drawback: the damping parameter is non-differentiable. This means one is solving a (slightly) different optimization problem every time the scaling parameter is updated. Yet, as the optimization converges, the changes between successive design iterations diminish and c_b tends to converge.

Recently, Yang *et al.* (2018) proposed another approach combining the stability transformation method for chaos control of nonlinear dynamic systems and oscillation control of iterative computation (see references therein). They claimed this new scheme is "an exact correction of the global stress measure", and the global stresses are modified in the same manner as the previous method.

Thus, this new adaptive correction factor is defined as

$$c_b^{(i)} = \alpha^{(i)} \frac{\sigma_{max}^{(i)}}{\sigma_{lim} \Psi_b^{(i)}} + \left(1 - \alpha^{(i)}\right) c_b^{(i-1)}, \tag{A.25}$$

a very similar expression to the one in Equation (A.24). In this dissertation, we opt for the approach of Equation (A.25).

A.6 Comparison of Different Strategies

A study is performed to investigate the methodologies under the global (aggregation into one constraint), block (regional constraints), and local (ALM) strategies. In this section, all simulations[16] were conducted using Matlab R2022a on a desktop computer with Intel(R) Core(TM) i9-7920X CPU @ 2.90GHz processor and 64 GB of RAM with NVIDIA GeForce GT 710 and 1.00 GB of RAM.

For the global strategy we study:

- the variation of aggregation parameter, p_a, for the P-norm;
- the effect of the adaptive normalization factor, c_p;
- the influence of different aggregation functions: P-norm, P-mean, and upper and lower bounds KS functions.

Regarding the regionalization of constraints, we compare:

- the solution attained using some of the techniques discussed in Appendix A.5, namely EIT, SDT, and SLT;
- the influence in the number of blocks for a fixed technique, the SLT.

These methods were compared to the ALM-based solution assuming the *qp*-approach for relaxing the stress measure. In the local approach, we use the modified version of the unconstrained MMA implemented by Giraldo-Londoño & Paulino (2021), while for the above-mentioned strategies the 2007 MMA release (Svanberg, 2007) was considered.

To the best of the author's knowledge, two similar researchers have been described in the literature. París *et al.* (2010) contrasted global, block, and local strategies. Computationally, the results were costly, even with coarsened meshes (6,400 bi-quadratic quads). For instance, the local constraints were set by setting $N_b = N_c$, which resulted in higher times, and some simulations took 271.4 hours, or nearly 11 days and 8 hours. Naturally, this extended time was also related to the computer capacity and the strategy used. In this work,

[16]Since our simulations correspond to the same optimization procedure (e.g. filter kernel, material interpolation, stress relaxation), we had the luxury of not thresholding each of the optimized designs to 0–1 solution (Sigmund, 2022).

they opted to rewrite the optimization problem in a quasi-unconstrained form utilizing a modified inverse barrier function with proper rescaling, which was solved through the conjugate gradient method. The results indicated that: (i) aggregation can lower costs, and (ii) different techniques lead to different optimal topologies.

da Silva *et al.* (2021a) studied approaches for global and local strategies. A remarkable work was done as they compared the effect of different optimizers (MMA and steepest descent method) on two unconstrained optimization formulations (ALM and EPM) in the local approach. In turn, for the global strategies, they either assumed continuation in the aggregation parameter with or without c_p or considered a fixed value for p_a. This research was among the first to successfully address stress-related issues with high levels of p_a. In brief, the authors noted that: (i) both strategies generated nearly independent meshes and feasible solutions, (ii) the solutions were sensitive to the number of iterations allowed in certain optimization stages, especially for the global strategies, (iii) the aggregation-oriented approaches were more sensitive to the continuation procedure, and (iv) a fixed value of p_a required more iterations until convergence.

Thus, this section may be seen as complementary research addressing some of the issues left unexplored in these prior publications, like the usage and comparison of different block formation strategies. With that in mind, we will skip the sensitivity computation (necessary for gradient-based optimizers). Nonetheless, the study of Holmberg *et al.* (2013) gives the sensitivities for the global- and regional-aggregated approaches, whereas Giraldo-Londoño & Paulino (2021) provides the analytical solution for the derivatives in the ALM.

A.6.1 L-Bracket

The L-bracket benchmark example of Figure A.6 is analyzed. This structure is modeled for infinitesimal displacements under the assumption of a plane stress state and is discretized by 25,600 bilinear quads.

The L-bracket is supported on the top edge and submitted to a load F, distributed on the nodes within the distance d to avoid stress concentration. The material properties refer to a typical steel, where E_0 and ν_o are the Young's modulus and Poisson's ratio, respectively.

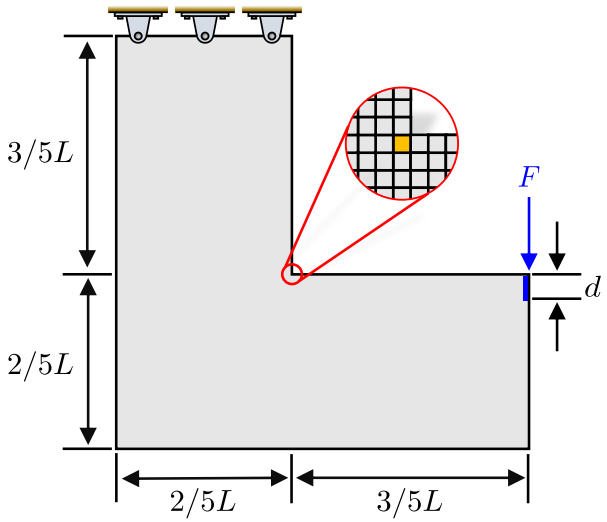

Load & Geometry:
$F = 400$ N
$L = 100$ mm
$t = 1$ mm
$d = 6$ mm

Material Properties:
$\sigma_{lim} = 241$ MPa
$E_0 = 197$ GPa
$\nu_0 = 0.29$

Figure A.6: L-bracket.

Our analyses are divided into two phases:

1. the adjusting phase, where SIMP is combined with tanh function of Equation (4.3). The projection parameter at the $(i+1)$-th iteration, $\beta^{(i+1)}$, follows a continuation procedure described by

$$\beta^{(i+1)} = \min\{f_\beta \beta^{(i)}, \beta_{max}\}, \tag{A.26}$$

with

$$f_\beta = \left(\frac{\beta_{max}}{\beta^{(0)}}\right)^{\left(\frac{1}{n_{Min}/\beta_f - 1}\right)}, \tag{A.27}$$

in which f_β follows the recommendations of da Silva *et al.* (2021a). This phase ends solely when $\beta^{(i+1)}$ meets the maximum value, $\beta_{max} = 20$, and

2. the stabilization phase, where $\beta^{(i+1)}$ is fixed, and the optimization procedure is allowed to converge under the following criteria:

$$||\boldsymbol{z}^{(i+1)} - \boldsymbol{z}^{(i)}||_\infty \leqslant \tau_\rho, \qquad \text{for design variables,} \tag{A.28}$$

$$\frac{\max\{\sigma^{vM,(i)}\}}{\sigma_{lim}} - 1 \leqslant \tau_\sigma, \qquad \text{for stress.} \tag{A.29}$$

To reduce oscillation, we introduce limitations on the minimum and maximum changes of the design variables. Then, the MMA routines modify to

$$\underline{\boldsymbol{z}} = \max\{0, \boldsymbol{z} - Osc\} \quad \text{and} \tag{A.30}$$

$$\overline{\boldsymbol{z}} = \min\{1, \boldsymbol{z} + Osc\}, \tag{A.31}$$

where $\underline{\boldsymbol{z}}$ and $\overline{\boldsymbol{z}}$ are, respectively, the modified lower and upper bounds of the design variable, and Osc is an oscillation parameter recommended by

Fernández *et al.* (2019). Table A.1 refers to the MMA parameters, while Table A.2 contains the information associated with the optimization.

Variable	Description	Value
a_0	Initial asymptotes	0.2
a_{inc}	Asymptotes increment	1.2
a_{dec}	Asymptotes decrement	0.7
$Move$	Allowable move step	0.05
Osc	Oscilation parameter	0.1

Table A.1: MMA parameters used in the L-bracket example.

Variable	Description	Value
$z_e^{(0)}$	Initial material distribution	1
R	Filter radius	4 mm
s	Filter exponent	3
p	SIMP exponent	3
q	*qp*-approach penalty	2.5
n_{Min}	Number of iterations in the adjusting phase	1,000
n_{Max}	Number of total iterations	1,500
τ_ρ	Design variable tolerance	0.01
τ_σ	Stress tolerance	0.001
$\beta^{(0)}$	Projection parameter initial value	0.1
β_f	Projection parameter update frequency iterations	40
β_{max}	Projection parameter maximum value	20
f_β	Projection parameter increment	Eq. (A.27)

Table A.2: Optimization parameters used in the L-bracket example.

A.6.2 Stress Aggregation Strategy

In the global approach, we answer

$$\begin{aligned} \min_{\boldsymbol{z}} \quad & m(\boldsymbol{z}) = \frac{1}{V_0}\sum_{e=1}^{N_e} \tilde{\rho}_e(\boldsymbol{z}) V_e \\ \text{s.t.:} \quad & \hat{g}(\boldsymbol{z}, p_a) = \hat{\Psi}(\boldsymbol{z}, p_a) - 1 \leqslant 0 \\ & 0 \leqslant z_e \leqslant 1, \quad \text{for } e = 1, 2, \ldots, N_e \\ \text{with} \quad & \boldsymbol{K}(\boldsymbol{z})\boldsymbol{u} = \boldsymbol{f}, \end{aligned} \tag{A.32}$$

where $\hat{\Psi}$ is one of the aggregation functions of Appendix A.4 for stresses relaxed in the form of *qp*-approach (*vid.* Appendix A.3.2). Keep in mind that, from

now on, we assume $N_e = N_d = N_c$, since we take all of them at the element's centroid.

Initially, we fix the aggregation function as the P-norm and study how variations in the aggregation parameter, p_a, affect the final design. To do so, we assume $p_a = \{12, 24, 36, 48, 60\}$.

Figure A.7 illustrates the material and (normalized) stress distributions. As the value of the aggregation parameter increases, the material distribution seems to converge to a certain pattern, and the stresses approach the so-called fully stressed design, i.e., a configuration where most of the stresses are near the limit value. This observation supports the concept underlying the use of aggregation functions that says the larger the value of p_a, the closer the global function approaches the peak stress.

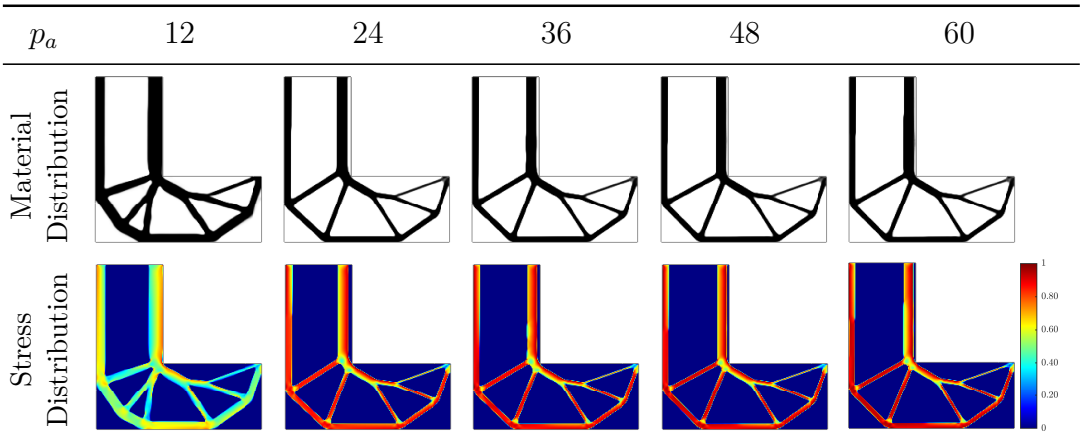

Figure A.7: L-bracket material and stress distributions for P-norm, with c_p, and varying p_a.

A question arises: why not increase the value of p_a even further? Theoretically, the best way to approximate the maximum stress would be for $p_a \to \infty$, which is not conceivable in practice. Since we were not able to achieve convergence for $p_a > 60$, another possible explanation is that the solutions degenerate, most likely owing to issues with gradient computing.

To verify this, we plot in Figure A.8 the P-norm stress versus the aggregation parameter for the reference element highlighted in Figure A.6. Here, the limit of p_a, in the x-axis, was set as the largest value before it attained a relative error of 10^{-3} in the stress approximation and without causing numerical issues in the derivative computation. This result indicates that larger values of p_a are unnecessary, as $p_a \geqslant 35$ provides reasonable estimates of peak stress. Although this finding depends on the material properties and boundary conditions, among others, the exponential-like behavior appears to indicate a trend regardless of the aggregation function used.

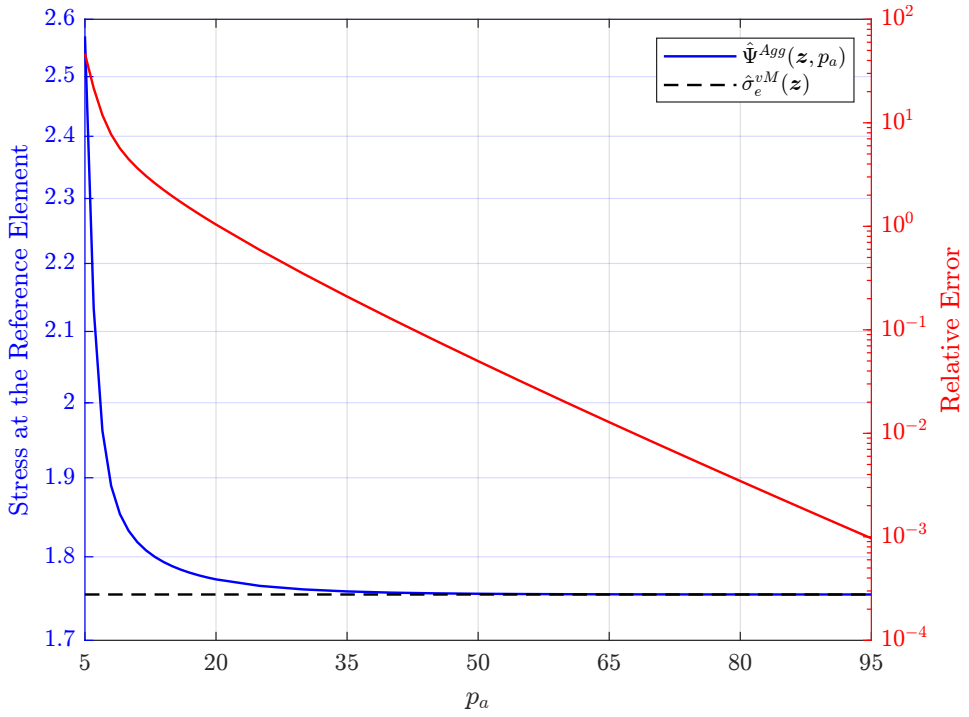

Figure A.8: P-norm as a function of aggregation parameter.

Table A.3 displays a few parameters obtained in the simulations of Figure A.7, where the gray levels are measured by

$$M_{nd} = \frac{\sum_{e=1}^{N_e} 4\tilde{\rho}_e(1-\tilde{\rho}_e)}{N_e} \times 100\%. \tag{A.33}$$

	Aggregation Parameter, p_a				
	12	24	36	48	60
M_{nd} (%)	5.35	3.48	3.59	3.84	4.05
Mass (%)	37.05	25.68	24.54	23.99	24.01
$\max\{\hat{\sigma}_e^{vM}(\boldsymbol{z})\}/\sigma_{lim}$ - 1	-0.0093	-0.0012	-0.0008	-0.0120	-0.0002
Active Elements (%)	0.01	0.84	3.82	6.18	6.68
Number of Iterations	1,000	1,000	1,000	1,000	1,000
Time (min)	12.7	12.9	13.3	13.6	13.9

Table A.3: Solution parameters based on P-norm, with c_p, and varying p_a.

We observed that: (i) all topologies resulted in feasible solutions, (ii) despite the concentration of grayish elements near the vertical right bar, the overall presence of intermediate densities (M_{nd}) was below 6%, (iii) as the value of the aggregation parameter was increased, the P-norm value approached the peak stress, contributing to the increase in the number of active elements[17],

[17]The number of active elements is defined over the solid elements ($\tilde{\rho}_e \geqslant 0.05$). So, those who were $\sigma_e \geqslant 0.95\sigma_{lim}$ were considered active.

(iv) the optimized design tended to stabilize for $p_a = \{48, 60\}$ since the mass did not exhibit substantial variations, (v) the processing time was similar in all cases, but increased slightly – about 18 seconds – with increasing p_a, and (vi) all simulations ended after 1,000 iterations. This occurred because our algorithm was forced to perform the minimum number of iterations designated for the adjusting phase. After this stage, the solver has already met the tolerances imposed in the stabilization phase, and the optimization process ends.

Next, we examine the impact of the stress adaptive correction factor, c_p. Figure A.9 highlights solutions without employing this factor for $p_a = \{12, 36, 60\}$, whereas Table A.4 returns the corresponding metrics. Apart from the degenerated solution for $p_a = 12$ – which did not converge, hence the longer operation time –, all other topologies had maximum stresses considerably lower than σ_{lim}, signaling that less material was removed compared to the Figure A.7 solutions. On the other hand, as expected, the mass ratio is higher than those indicated in Table A.3. Not surprisingly, no element is active; therefore, p_a is critical in estimating the P-norm value.

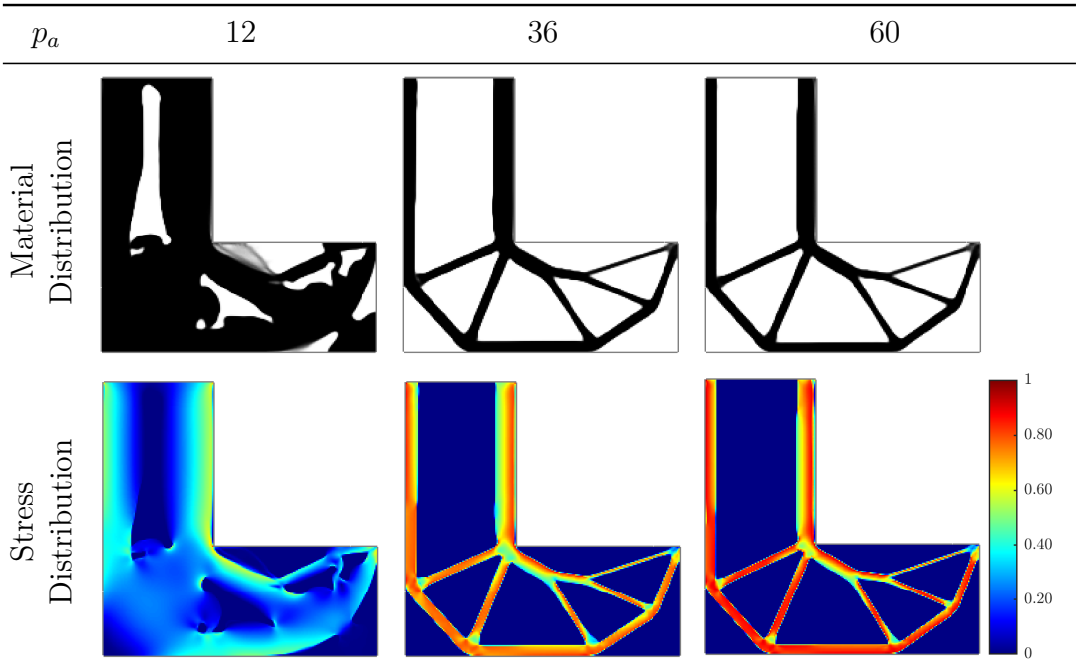

Figure A.9: L-bracket material and stress distributions for P-norm, without c_p, and varying p_a.

	Aggregation Parameter, p_a		
	12	36	60
M_{nd} (%)	4.32	3.33	3.76
Mass (%)	82.38	28.41	25.71
$\max\{\hat{\sigma}_e^{vM}(\boldsymbol{z})\}/\sigma_{lim}$ - 1	-0.2224	-0.1190	-0.0723
Active Elements (%)	0	0	0
Number of Iterations	1,000	1,000	1,000
Time (min)	22.4	13.7	13.6

Table A.4: Solution parameters based on P-norm, without c_p, and varying p_a.

Figure A.10 exhibits the layouts for the P-mean and upper and lower bound KS functions for $p_a = 12$ and considering c_p. Similar material distributions were acquired. We also noticed that increasing the value of p_a, made the designs even more similar to each other (*cf.* Figure A.7), so, for convenience, we chose not to include them here.

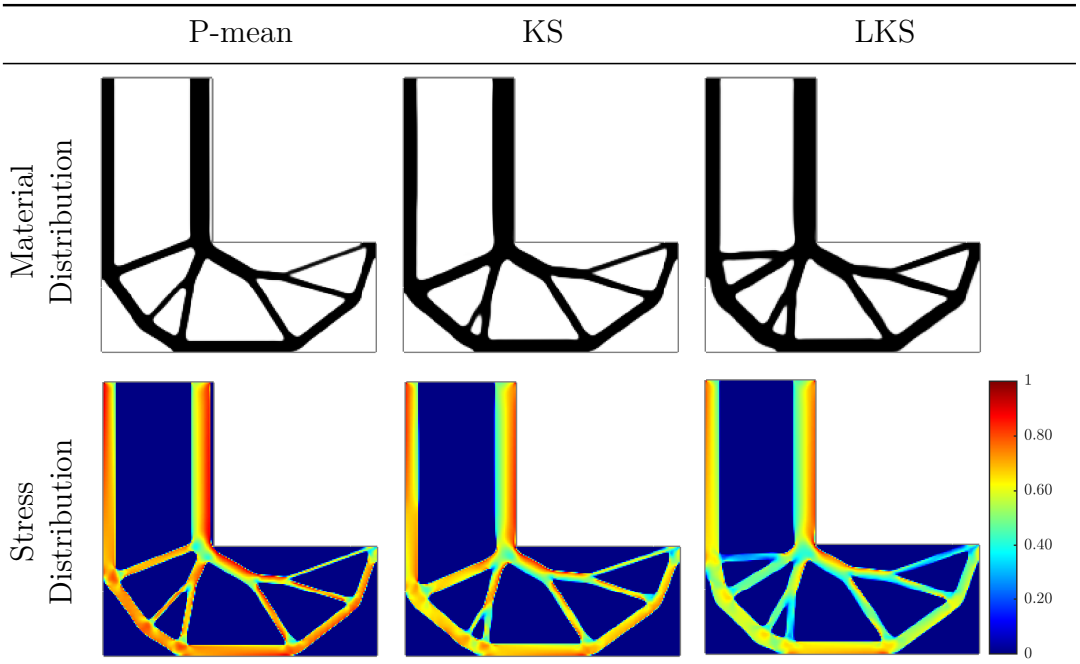

Figure A.10: L-bracket material and stress distributions for different aggregation functions and $p_a = 12$.

Table A.5 has additional information about these simulations. Due to the non-uniform stress distribution, the lower bound KS function has a final mass about 4-7% larger than the others, while the gray levels are around 1% larger (except for the P-norm – *vid.* Table A.3). Albeit the peak stress is closer to the allowable one in all the approximations, the percentage of active components is quite low, indicating the existence of a stress concentration point in the sharp

corner rather than a uniform distribution. Regarding the computing time, no remarkable distinction was seen in our simulations.

	Aggregation Function, $\hat{\Psi}$		
	P-mean	KS	LKS
M_{nd} (%)	3.85	3.91	4.90
Mass (%)	28.79	31.32	35.62
$\max\{\hat{\sigma}_e^{vM}(\boldsymbol{z})\}/\sigma_{lim}$ - 1	-0.0273	-0.0115	-0.0049
Active Elements (%)	0.07	0.01	0.01
Number of Iterations	1,000	1,000	1,003
Time (min)	13.2	13.2	13.2

Table A.5: Solution parameters for different aggregation functions and $p_a = 12$.

Finally, we research the mesh-dependence for $p_a = 48$[18] in Figure A.11 and Table A.6. One can observe the final topologies are somehow dependent on the FE discretization (see the discussion in Appendix B): (i) the solution with 57,600 elements had difficulty defining material near the right vertical bar, while the topologies with 160,000 and 230,400 elements showed the same adversity, but near the load application locality, (ii) as the mesh size increased, the vertical bar on the right was moved further away from the design boundary, and (iii) the continuation scheme proposed for the tanh function was not particularly effective as the some layouts persist with an oblique element of intermediate density connecting the vertical bars. Naturally, the calculating times increased as the mesh was refined.

	Mesh Size, N_e		
	57,600	160,000	230,400
M_{nd} (%)	3.97	5.71	7.50
Mass (%)	25.11	30.46	31.02
$\max\{\hat{\sigma}_e^{vM}(\boldsymbol{z})\}/\sigma_{lim}$ - 1	-0.0025	-0.0105	0.0009
Active Elements (%)	3.45	0.17	1.79
Number of Iterations	1,000	1,001	1,000
Time	29.2 min	1.54 h	2.28 h

Table A.6: Solution parameters for different mesh size and P-norm.

[18]This value was chosen because the relative error in Figure A.8 was below 0.1.

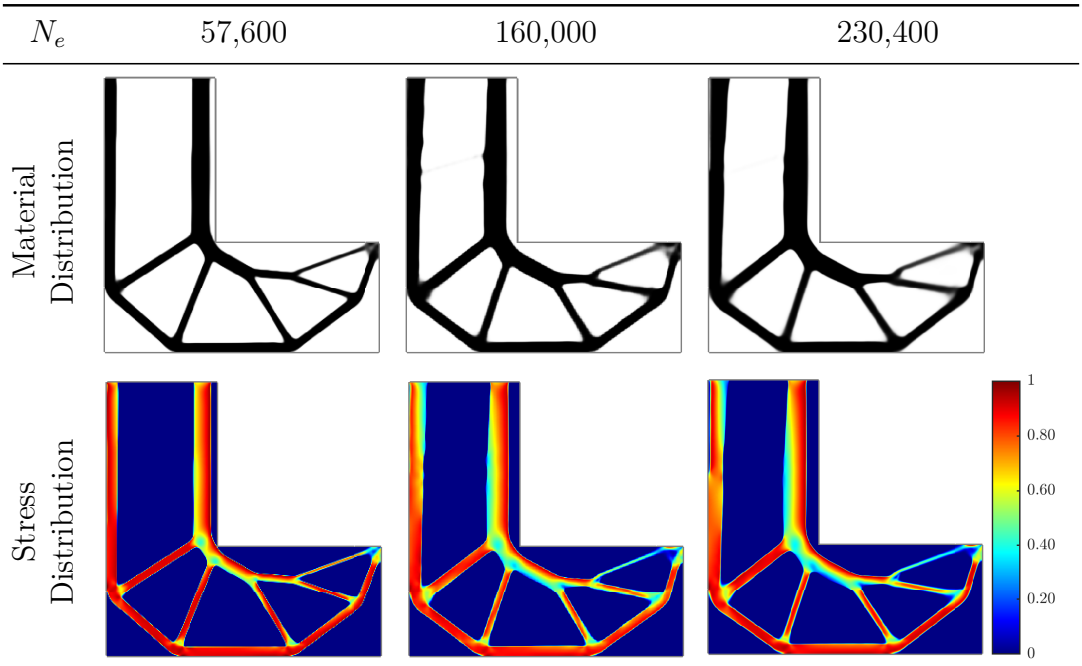

Figure A.11: L-bracket material and stress distributions for different meshes with $p_a = 48$ and P-norm.

A.6.3 Stress Regionalization Strategy

In this section, we deal with the optimization in the form of

$$\begin{aligned} \min_{\boldsymbol{z}} \quad & m(\boldsymbol{z}) = \frac{1}{V_0} \sum_{e=1}^{N_e} \tilde{\rho}_e(\boldsymbol{z}) V_e \\ \text{s.t.:} \quad & \hat{g}_b(\boldsymbol{z}, p_a) = \hat{\Psi}_b(\boldsymbol{z}, p_a) - 1 \leqslant 0, \quad \text{for } b = 1, 2, \ldots, N_b, \\ & 0 \leqslant z_e \leqslant 1, \quad \text{for } e = 1, 2, \ldots, N_e \\ \text{with} \quad & \boldsymbol{K}(\boldsymbol{z})\boldsymbol{u} = \boldsymbol{f}, \end{aligned} \tag{A.34}$$

where $\hat{\Psi}_b$ is an aggregation function defined by one of the block techniques discussed in Appendix A.5, and N_b is the number of blocks.

To investigate the influence of regional constraints in the optimal layout, we fix the aggregation function as the P-norm and alter the number of blocks, N_b, as well as their forming methods. Figure A.12 shows the material and stress distributions adopting the EIT, SDT, and SLT with number of blocks ($N_b = \{1, 2, 4, 5, 10, 20, 40, 50\}$) and $p_a = 12$.

N_b	EIT	SDT	SLT
1	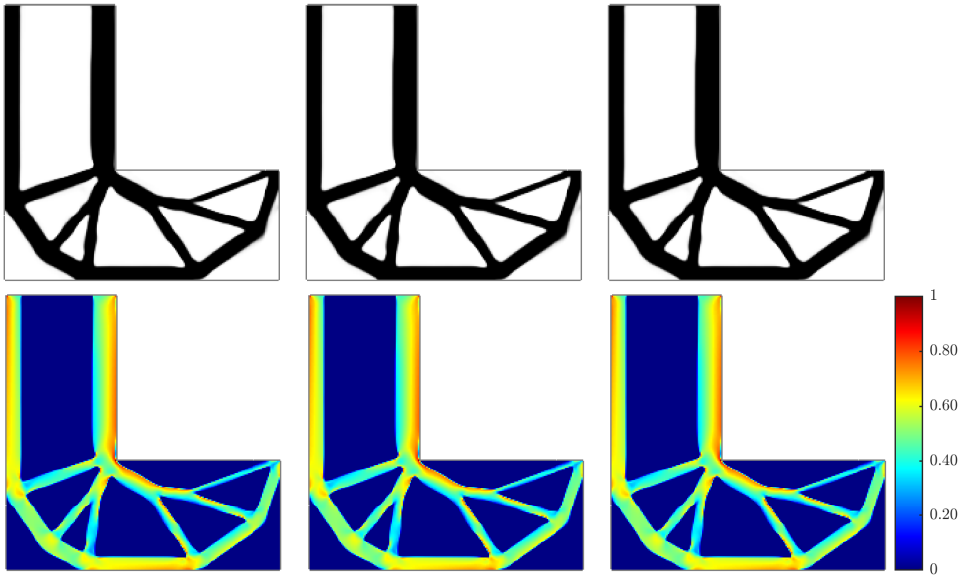		
2	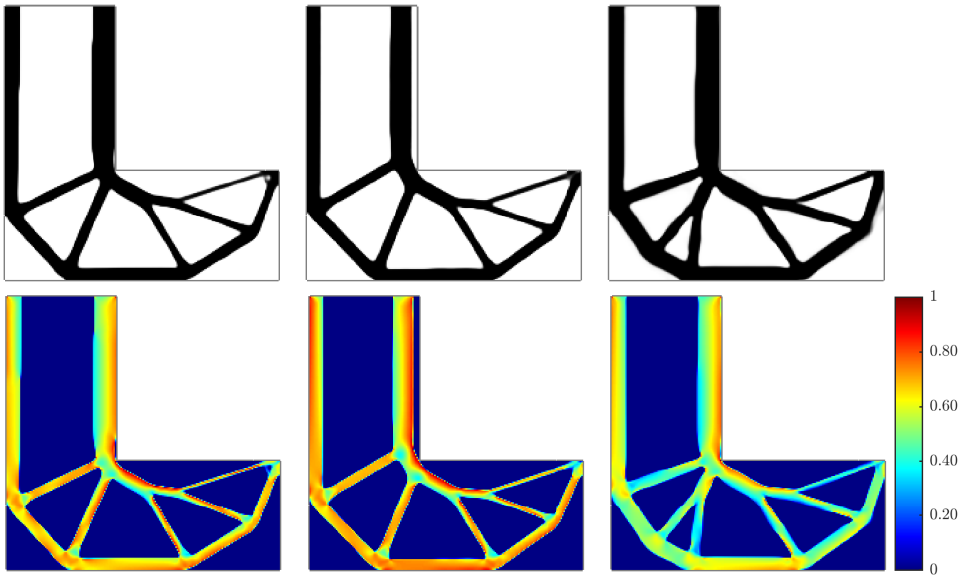		
4	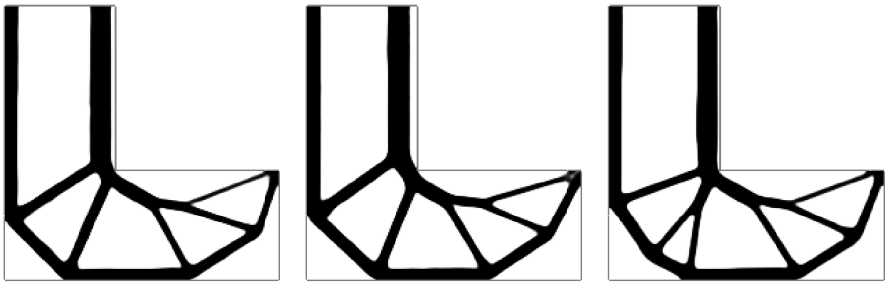		

Continued on next page

N_b	EIT	SDT	SLT
	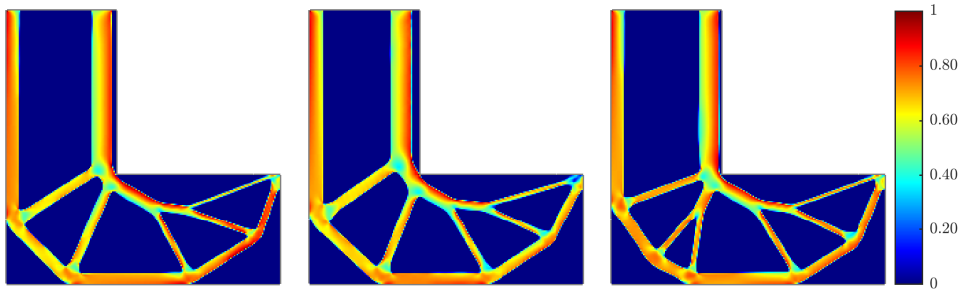		
5	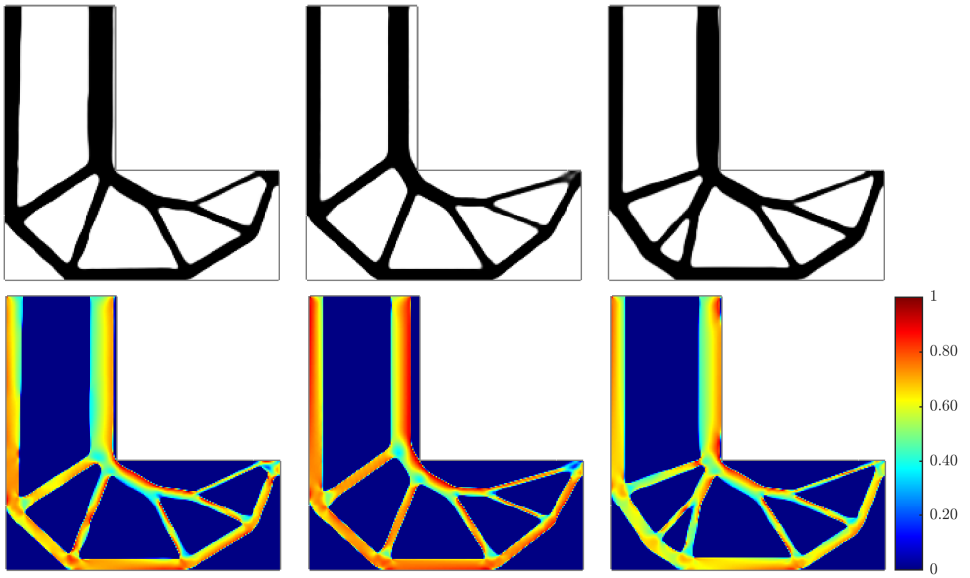		
10	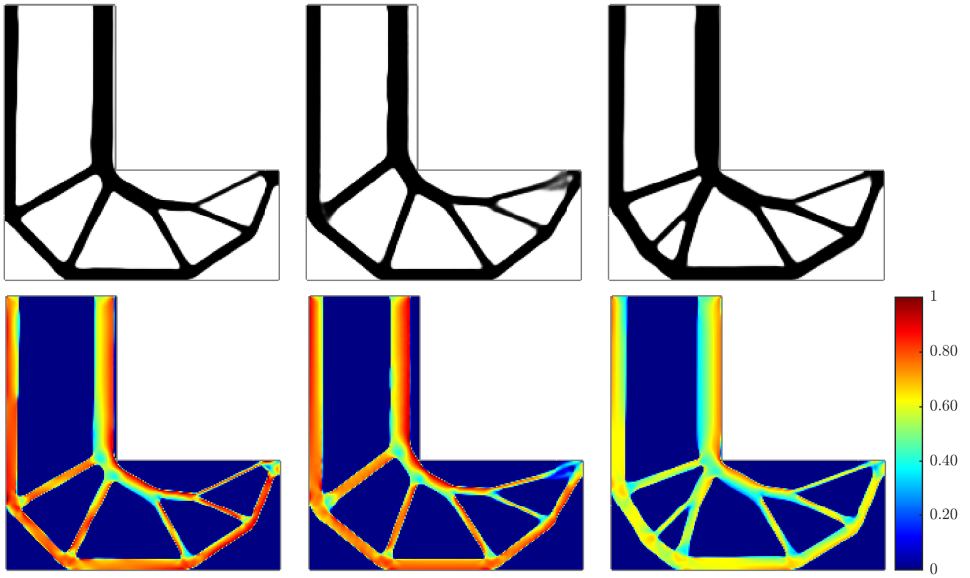		

Continued on next page

N_b	EIT	SDT	SLT
20	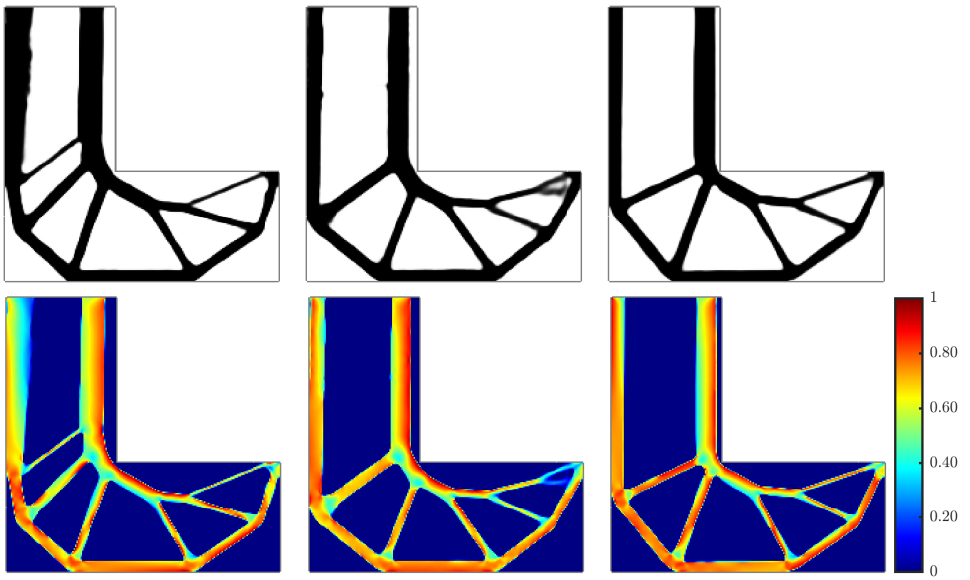		
40	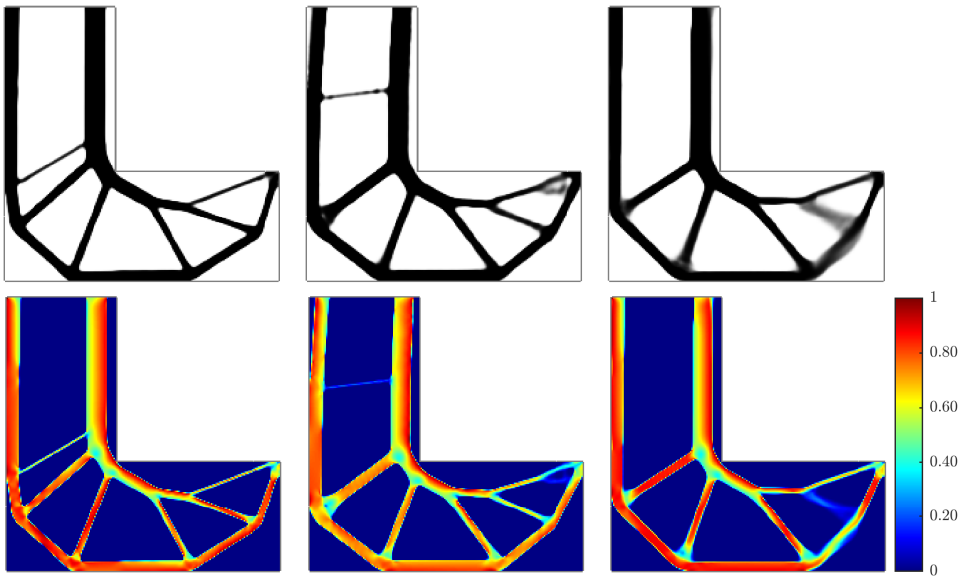		
50	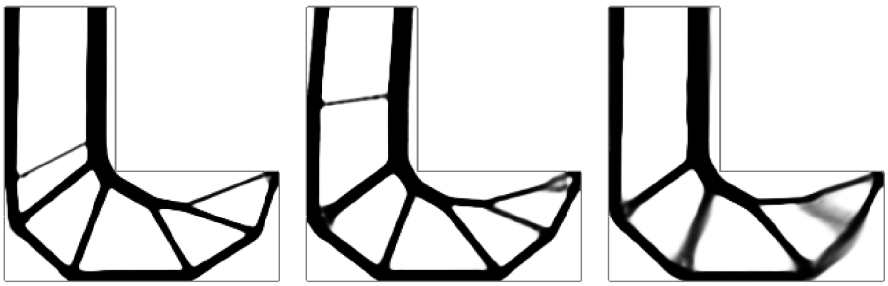		

Continued on next page

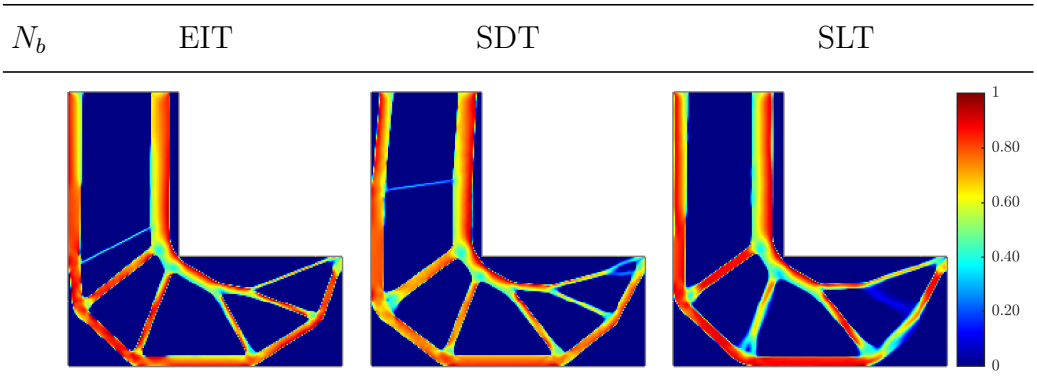

Figure A.12: L-bracket material and stress distributions with $p_a = 12$, P-norm and different block formation methods.

As expected (i) for $N_b = 1$, the solution was independent of the block formation technique, and (ii) for a given $N_b > 1$, the optimized topologies from different regionalization techniques were similar but not identical. Furthermore, as the number of blocks increases: (iii) the material distributions tend to follow a specific layout that differs between the regionalization techniques, and (iv) the optimization procedure becomes cumbersome in the sense of less clear material distributions and more grayish regions. In this context, the MMA struggles to remove material, since it is necessary to maintain the new level of estimated stresses.

Mass reduction requires increasing the stress level. This is evidenced, for example, at $N_b = 40$ for the EIT, where the L-bracket had the higher mass ratio and the lower peak stress (*cf.* Figures A.13(a) and A.13(b)). Unfortunately, we cannot guarantee any tendency, as both the mass and stress suddenly changed the slope sign as N_b increased – observe, for example, we had an inflection point at $N_b = 20$.

Figure A.13(c) shows a linear trend between the processing time (s) and the number of blocks, N_b. Similarly, the percentage of active elements seems to increase as the number of blocks increases. Consider the EIT in Figures A.13(c) and A.13(d): when a single block was altered for $N_b = 50$, the computing time increased from around 12.8 minutes to more than 2.5 hours. On the other hand, the percentage of active elements increased from around 0.01% at $N_b = 1$ to 1.53% when 50 blocks were employed. Hence, the effort spent generating blocks, and computing constraints and their derivatives seemed to justify using regionalization approaches.

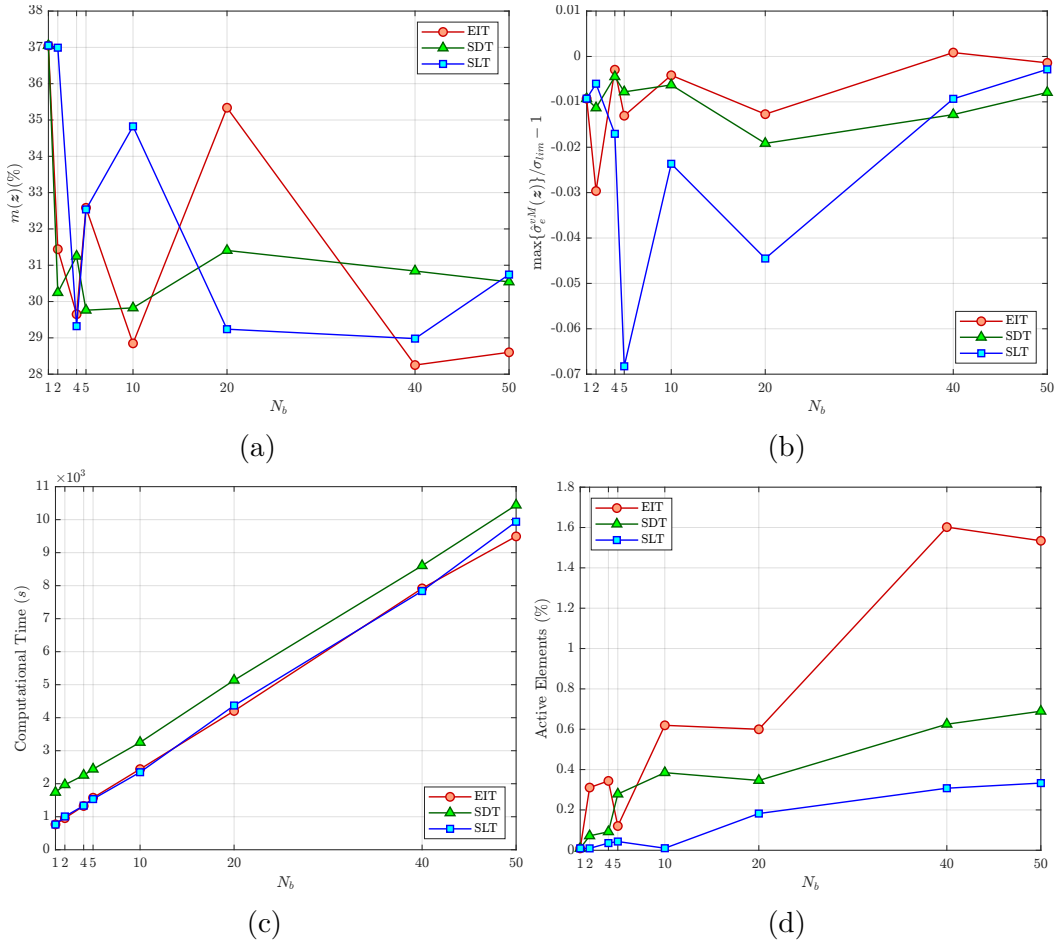

Figure A.13: History of (a) mass, (b) stress, (c) computing time and (d) active elements versus the number of blocks.

Figure A.14 shows the material and stress distributions for $N_b = \{1, 5, 50\}$ and $p_a = 48$, assuming the same block formation methods as before. Our simulations yielded homogenous designs for the majority of the tested blocks, except for $N_b = 50$. When the number of blocks increased, the position of the right vertical bar sild further from the edge and angled similarly to the left bar. This is notably true for the SDT and SLT, where the solver redistributed material along the structure's boundaries, especially at the right bottom edge of the domain. This argument explains the amount of intermediate design variables seen in $N_b = 50$. But a growth in grayish regions may suggest the solver's inability to handle numerous stress constraints – at least, for the considered material properties and imposed methods – prompting more investigation.

N_b	EIT	SDT	SLT
1	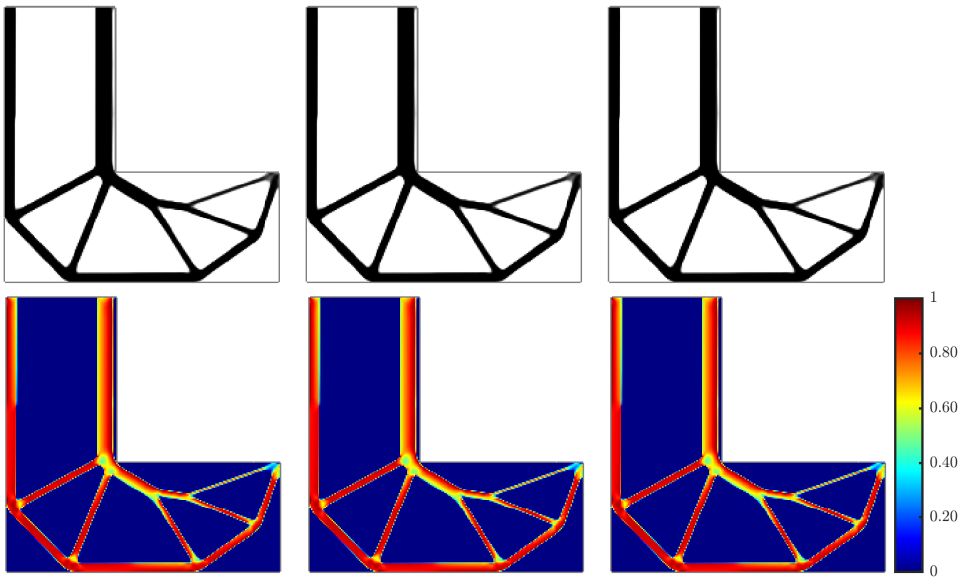		
5	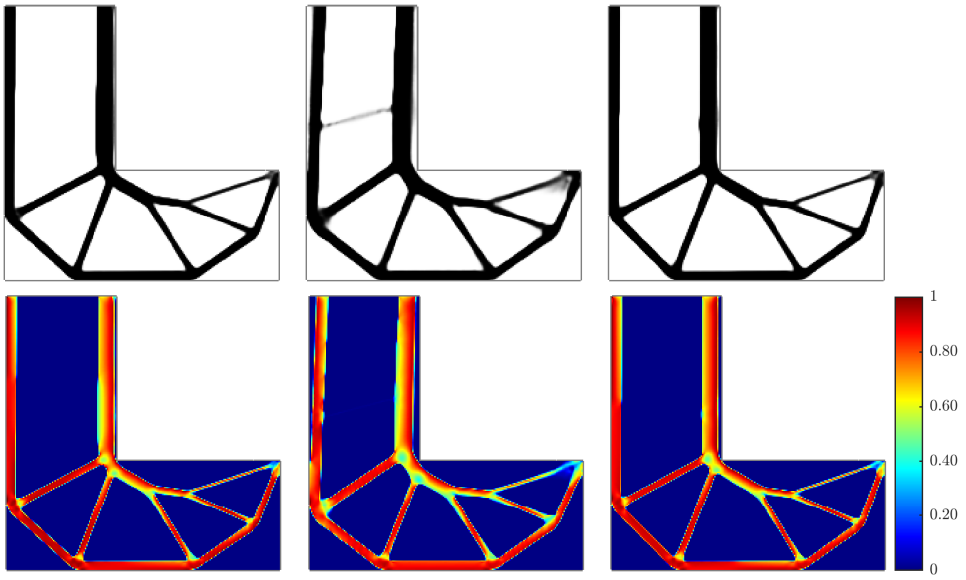		
50	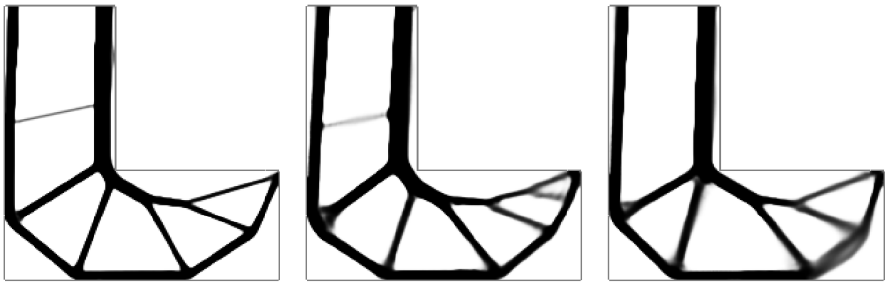		

Continued on next page

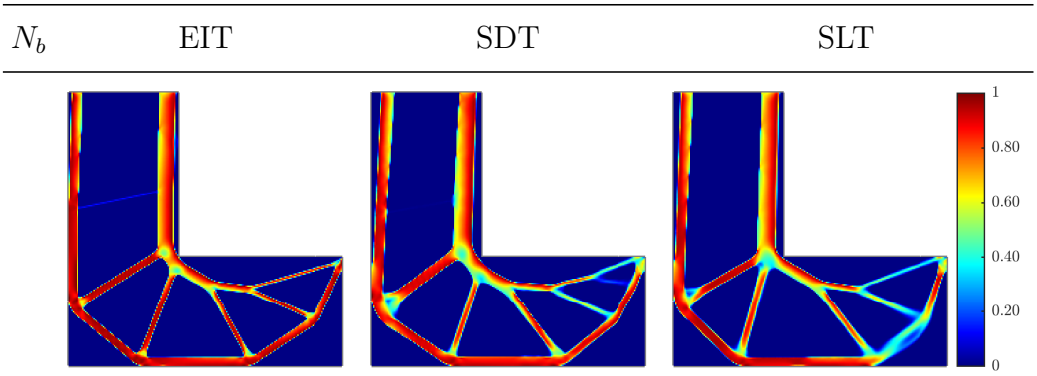

Figure A.14: L-bracket material and stress distributions with $p_a = 48$, P-norm and different block formation methods.

A.6.4 Local Stresses Strategy

For convenience, we repeat the AL formulation developed in Section 5.2:

$$\begin{aligned} \min_{\boldsymbol{z}} \quad & \mathcal{L}_A^{(i)}(\boldsymbol{z}, \boldsymbol{\mu}^{(i)}, \varphi^{(i)}) = m(\boldsymbol{z}) + \zeta \hat{\mathcal{A}}^{(i)}(\boldsymbol{z}, \boldsymbol{\mu}^{(i)}, \varphi^{(i)}), \\ \text{s.t.:} \quad & 0 \leqslant z_e \leqslant 1, \quad \text{for } e = 1, 2, \ldots, N_e \\ \text{with} \quad & \boldsymbol{K}(\boldsymbol{z})\boldsymbol{u} = \boldsymbol{f}, \end{aligned} \tag{A.35}$$

where the auxiliary term is

$$\hat{\mathcal{A}}^{(i)}(\boldsymbol{z}, \boldsymbol{\mu}^{(i)}, \varphi^{(i)}) = \sum_{e=1}^{N_e} \left[\mu_e^{(i)} \hat{g}_e^{+}(\boldsymbol{z}, \boldsymbol{u}) + \frac{\varphi^{(i)}}{2} \hat{g}_e^{+}(\boldsymbol{z}, \boldsymbol{u})^2 \right]. \tag{A.36}$$

Remember that the symbol $\hat{\bullet}$ assigns to relaxed quantities.

We tested several parameter combinations and found the best results were achieved with $\boldsymbol{\mu}^{(0)} = \mathbf{0}$, $\varphi^{(0)} = 20$, $\varphi_{max} = 10^4$, and $\phi = 1.02$. The ALM sub-problem was solved through the MMA unconstrained version with up to 5 iterations per step (Giraldo-Londoño & Paulino, 2021). The remaining parameters and strategies (filtering scheme, projection function, stress relaxation, and so forth) are the same applied in Appendices A.6.2 and A.6.3 – allowing for a fair comparison of the different techniques.

Figure A.15 presents material and stress distributions across different mesh sizes. We found topologies whose stress evaluation points met the imposed tolerance, regardless of mesh refinement. Furthermore, even though we also observed an increase in the gray near the load application point, this increase was far less significant, and the final designs rely less on mesh discretization than solutions obtained via aggregation (*cf.* Figure A.11).

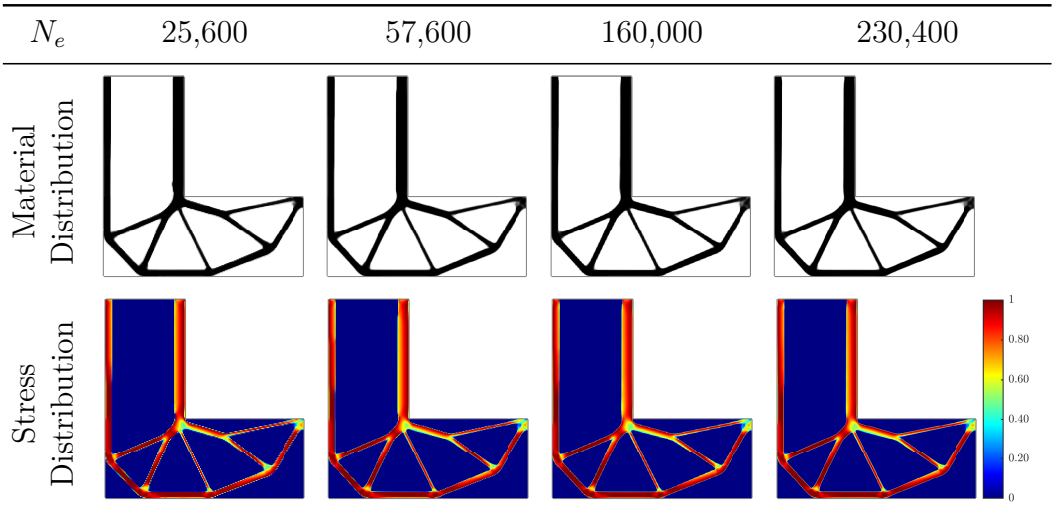

Figure A.15: L-bracket material and stress distributions for different mesh sizes and ALM.

Table A.6 contains information on the aforementioned simulations. Our outcomes indicated that: (i) the amount of grayish elements was practically constant, as it varied 0.16% from the smallest to the highest computed values, (ii) the overall mass could be considered constant due to the 0.18% of variation observed, (iii) the percentage of active elements was around 40% – a large increase compared to the designs generated by the aggregation techniques (*cf.* Tables A.3 and A.5), and (iv) the stresses were much closer to the admissible value, making better use of material than other techniques. Perhaps the main disadvantage was the processing time, which for ALM was greater than those presented in Appendix A.6.2.

	Mesh Size, N_e			
	25,600	57,600	160,000	230,400
M_{nd} (%)	4.11	4.09	4.25	4.23
Mass (%)	22.74	22.69	22.57	22.56
$\max\{\hat{\sigma}_e^{vM}(\boldsymbol{z})\}/\sigma_{lim}$ - 1	0.0001	0.0004	0.0002	0.0009
Active Elements (%)	44.56	44.51	47.14	47.31
Number of Iterations	1,000	1,000	1,000	1,000
Time	33.5 min	1.29 h	4.20 h	6.45 h

Table A.6: Solution parameters for different mesh sizes and ALM.

A.6.5
Remarks on the Different Strategies

The remarks outlined herein may not be definitive. The optimization process is parameter-dependent, i.e., it relies on the optimizer version and its initial and

update parameters, the boundary conditions, loads, material properties, and so on. Even so, the comments presented here provide useful insight into how the discussed strategies (local, global, and regional stress constraints) work on the stress-constrained topology optimization problem.

So, we highlight:

- in the global stress constraint approach, the larger the value of the aggregation parameter, p_a, the smaller the gap between the aggregated and the maximum stresses. In theory, this approach works better for larger values of p_a, as detached in Figure A.8. Nevertheless, the choice of p_a is problem-dependent and must be recalculated if the material or any of the optimization strategies change;
- the stress adaptive correction factor, c_p, better approximates the aggregated function value to the peak stress. It may also be essential in achieving consistent topologies, especially for smaller values of p_a, as seen in Figure A.9;
- the regional stress constraints approaches enhance global function layouts. Our research has shown that when the number of blocks, N_b, increases, the material distribution shifts toward a fixed, fully-stressed design. Anyway, the block creation procedure as well as the number of blocks that will result in an 'ideal' project remain unknown at first sight. One must take into account the possibility of finding 'not-so-well-defined' designs;
- the local stress constraint from the AL function ended in a larger mass reduction. This is probably due to the intrinsic behavior of the AL function, which better captured the local nature of stresses resulting in more active elements. The solutions were also clearer, especially near the left verticals bars and in the sharp corner spots of the L-bracket;
- concerning mesh discretization, our global and regional approaches resulted in some level of mesh dependency. The same, though, cannot be said of the ALM, where the optimized designs (in the range tested) were very similar to each other;
- larger computing times were observed in the ALM compared to aggregation techniques under the same mesh.

Regionalization will make the user hostage to both the block formation method and the number of blocks employed. Therefore, it does not appear to be an attractive option. In general, we might say the choice between global or local stress approaches is up to the reader. Yet, having at disposal a proper technique

with consistent responses (greater mass reduction and mesh-independence capabilities), such as the AL method, and not employing it appears to be, at the very least, foolish.

B
A Quick Discussion on Mesh-dependence

The following passage from Sigmund & Petersson (1998) helps exampling the concept of mesh-dependence:

> Mesh-refinement should result in a better modeling of the same optimal and a better description of boundaries – not in more detailed and qualitatively different structure.

We open space here for a simple but important conversation – at least in the context of this dissertation. According to traditional sources like Bendsøe & Sigmund (2003), an algorithm's ability to prevent the creation of finer members through mesh-refinement indicates that the solution to a topology optimization problem is mesh-independent. In this sense, the regularization techniques mentioned in Section 4.1.1 solve this issue. These methods, however, do not guarantee that the material will be arranged in similar locations when comparing solutions obtained in refined vs coarsed meshes, especially in stress-based topology optimization problems.

We highlight this debate because some of the findings in Appendix A are somehow mesh-dependent, even when the size of structural members remains unchanged. The idea of mesh-dependence adopt here was just to emphasize the possibility that some stress-based techniques may result in unforeseen changes to the material arrangement, especially at the boundaries and in the vicinity of loading localities.